Collective and Optical phenomena in equilibrium and nonequilibrium interacting quantum systems

PhD Thesis

Eduardo Mascarenhas

Supervisor: Marcelo Santos

Thesis presented to the Physics Graduate Program at *Universidade Federal de Minas Gerais.*

2014

Abstract

In this thesis we study collective, emergent and optical properties of interacting quantum systems both in equilibrium and nonequilibrium situations from a microscopic modelling. This orientation steams from both the fact there is a profound need to design, characterise and set up control strategies for realistic systems in which quantum technologies could be conceived and the interest to grasp and identify fundamental principles for the emergence of macroscopic behaviour. The thesis is divided into three parts: I Optical and Collective Phenomena; II Equilibrium many-body systems and III Nonequilibrium many-body systems. Part I includes four complementary contributions to the optics emerging from the collective behaviour of microscopic quantum systems. In part II (Equilibrium many-body systems) of the thesis I have addressed the physics of quantum phase transitions from the perspective of nonequilibrium thermodynamics. We have shown that such an approach captures the essential features of finite order transitions that have a strong connection to thermodynamical and energetic figures of merit, but does not capture infinite order transitions that are of a much more subtle nature. Motivated by these "exotic" infinite order transitions we have looked at quantum phases and phase transitions through an informational and operational perspective based on pure state conversions restricted by local operations. In the third and last part (Nonequilibrium many-body systems) of the thesis I have laid out a project on the closed evolution of quantum spin chains focussing on the emergent nonequilibrium laws that depart from equilibrium physics.

Acknowledgements

I have had the pleasure of collaborating with several scientists and friends who have contributed significantly to my research. Firstly I would like to thank Prof. Maria Carolina De Oliveira Aguiar, Dr. Simone Montenegro and, specially, Professor Marcelo Franca Santos for providing me with guidance in learning new physics and techniques throughout several years that have shaped this thesis.

Professor Dario Gerace for buying my ideas and providing daily assistance and indispensable feedback that have led to accomplished research.

Dr. Alexia Auffeves for including me in her research and point out weaknesses that needed to be strengthen.

(Soon to be) Dr. Helena Braganca for being the collaborator that worked most closely to me and for deeply impacting my recent research. She deserves substantial credit for the chapter on entanglement convertibility.

Dr. John Goold for being a constant inspiration and for always flooding my brain with modern and meaningful ideas.

Prof. Daniel Valente for the outstanding "one-dimensional" inspiration and for the perfect fusion of physics and alcohol.

Prof. Kavan Modi for the operationalising our lines of thought.

Dr. Filippo Fratini for believing in one idea, for thoroughly working on it and for helping me bring it to reality. He deserves substantial credit for the chapter on one-dimentional rectification.

There is a much longer list I would have to thank if I were politically correct. Since that is not the case I just thank CNPq for the financial support.

Introduction

Collective phenomena emerging out of the complexity and correlations of composite systems are most promising research topics for the future of modern science. There are many examples of collective phenomena that manifest themselves in different scales throughout science and our daily life and most importantly, they are commonly found in nonequilibrium conditions. The list is long as it is diverse, for instance: an orchestra is composed of single musicians each playing their own set of different notes and yet we interpret a symphony as a collective sound pattern; consciousness in living brains which is completely absent in single cells, the structure and existence of our planet and galaxy. Addressing emergent phenomena from a physical point of view is in general a difficult task both experimentally and theoretically. Despite of the obstacles, we have learned and deepened our understanding about nature by pursuing this topics. The major obstacle on the experimental side is controlling the systems on a microscopic scale, however, we have seen impressive advancements in the design and controlled tailoring of interacting quantum systems [1] in ultra-cold atoms and optical lattices [2], trapped ions [3] superconducting circuits [4, 5] and photonics [6].

On the theoretical side, the challenge is predicting macroscopic or collective behaviour whilst knowing only the microscopic laws. Fortunately, we have seen outstanding computational progress both in hardware and classical algorithms [7, 8] which allows us to describe complex quantum systems (at least in one dimensional geometries or other specific configurations) while modelling them on a microscopic scale. In this exciting new era of controlled collective quantum systems we have seen strong interdisciplinary activity between many-body physics, quantum information, quantum optics, atomic and molecular physics.

Profound debates on our understanding of nature are focussed on emergent behaviour, for instance, given that the microscopic laws of motion are confirmed to be quantum mechanical how do we observe classical laws of motion on macroscopic scales? The fact that "more is different" was highlighted by Anderson [9], meaning that, new laws emerge when we have significantly large amounts of interacting microscopic degrees of freedom. Describing the motion of interacting quantum systems has been a central goal for physicists ever since the microscopic laws of quantum motion were postulated. However, one of the main novelties in this research field is the discovery of strictly quantum correlations, such as entanglement [10] which were only carefully analysed by the end of last century. The complexity of quantum systems is in general higher than the classical counterparts mainly due to such entanglement in many-body states. On top of the intrinsic many-body complexity, different phenomena may be expected whether the composite system is in or out of equilibrium. When physical systems are found at thermodynamical equilibrium, be they quantum or classical, they are expected to obey a set of laws such that their collective statistical behaviour can be predicted (in principle) by thermodynamics or statistical mechanics regardless of their complexity. If however, the systems are out of equilibrium then there is no general set of

macroscopic rules to predict the emergent phenomena.

In this thesis we study collective, emergent and optical properties of interacting quantum systems both in equilibrium and nonequilibrium situations from a microscopic modelling. This orientation steams from both the fact there is a profound need to design, characterise and set up control strategies for realistic systems in which quantum technologies could be conceived and the interest to grasp and identify fundamental principles for the emergence of macroscopic behaviour.

The thesis is divided into three parts: I Optical and Collective Phenomena; II Equilibrium many-body systems and III Nonequilibrium many-body systems. Part I includes two complementary contributions to the optics emerging from the collective behaviour of microscopic quantum systems. I have addressed the physics of a single electromagnetic cavity mode interacting with a collection of non-interacting quantum emitters. We focused on the specific quantum states accessed by the emitters in the steady state regime and how they can influence the statistics of the light emitted by the cavity. Our approach departs from the usual way to tackle laser physics where each emitter is considered independently and one only worries about their overall statistical behaviour as a large gain medium. The ultimate goal is to understand the interplay between bosonic enhancement of the field due to entanglement between the emitters (superradiance) and that due to stimulated emission. This work is highly motivated by, now available, solid state micro-laser technologies in which the quantum nature of the emitters are carefully taken into account, thus departing from standard laser physics. We have shown how the statistics of the cavity output are imprinted with the quantum nature of the ensemble of emitters. In this work we have show how to quantify these effects and how they affect the laser physics. This work is an example of a nonequilibrium driven-dissipative quantum system that can be found in solid state platforms and the technics to measure and characterise the system are based on traditional quantum optical schemes.

The second contribution on the relation between statistical properties of emitted light and collective microscopic media took a different approach to study the nonequilibrium transport properties and control in photonic systems. In this case, the emitters were considered as an overall non-linear medium and the goal was to explore this non-linearity in order to design a quantum optical diode that is able to generate unidirectional (nonreciprocal) single or two photon pulses. Such devices are highly desirable in integrated photonic circuits, which are strong candidates for quantum information transfer and processing. Diodes are the building blocks of classical computers and they are likely to play an important role in quantum processing.

The third contribution also focusses on light transport and rectification. We present a theoretical analysis of a one-dimensional Fabry-Perot interferometer built with two highly saturable nonlinear mirrors embedded in a one-dimensional wave guide. In this architecture we use two level systems as mirrors which are highly nonlinear due to their quantum nature. Remarkably, we show that such an elementary device can operate as a microscopic integrated optical rectifier at high efficiency.

Also in quantum optical setups, but focussing on emergent equilibrium phases and the controlled simulation of condensed matter bulk systems, I have also studied the equilibrium and disordered behaviour of hybrid many-body systems composed of tunnel coupled electromagnetic cavities that interact with single two-level matter systems. This study is an example of the integration of condensed matter and quantum optics in which genuine quantum correlations are show to characterise the macroscopic quantum phases including the effects of disorder that induce localisation in the many-body state. Quantum simulations in coupled cavities has been a very hot topic due to the fast development of nano-fabrication techniques which have largely enhanced the quality factor of photonic crystal micro-cavities and waveguides and their coupling to artificial atoms such as quantum dots and NV-centers.

Our work on quantum-optics of many-body physics and specially the numerical and theoretical techniques learnt to develop it ended up presenting us with a whole new field to be explored in the thesis and that is why in the last portion of my PhD we have studied the physics of quantum spin chains. In part II (Equilibrium many-body systems) of the thesis I have addressed the physics of quantum phase transitions from the perspective of nonequilibrium thermodynamics. We have shown that such an approach captures the essential features of finite order transitions that have a strong connection to thermodynamical and energetic figures of merit, but does not capture infinite order transitions that are of a much more subtle nature. Motivated by these "exotic" infinite order transitions we have looked at quantum phases and phase transitions through an informational and operational perspective based on pure state conversions restricted by local operations. We have found that the notion of entanglement convertibility seems to be a detector of symmetries of the many-body state, rather then phase transitions. This work is an important contribution showing what kind of many-body properties can be captured by operational and informational points of view.

In the third and last part (Nonequilibrium many-body systems) of the thesis I have laid out a project on the closed evolution of quantum spin chains focussing on the emergent nonequilibrium laws that depart from equilibrium physics. In this project we present a few preliminary results on localisation properties and nonequilibrium effects emerging out of the interplay between disorder and interactions of quantum particles. Our preliminary results are quite promising since we have already uncovered interesting effects not reported previously in the literature.

For the sake of not being accused of self-plagiarism I should state that I have published most of the results in this thesis in peer reviewed journals and below I enumerate these references with a short abstract.

1. **Cooperativity of a few quantum emitters in a single-mode cavity**

   Phys. Rev. A, 88, 063825 (2013).

   Authors: Eduardo Mascarenhas, Dario Gerace, Marcelo Franca Santos, Alexia Auffeves

   We theoretically investigate the emission properties of a single-mode cavity coupled to a mesoscopic number of incoherently pumped quantum emitters. We propose an operational measure for the emitter medium cooperativity, valid both in the bad and in the good cavity regimes. We show that the opposite regimes of subradiance and superradiance correspond to negative and positive cooperativity, respectively. The lasing regime is shown to be characterized by nonnegative cooperativity. In the bad cavity regime we show that the cooperativity defines the transitions from subradiance to superradiance. In the good cavity regime it helps to define the lasing threshold, also providing distinguishable signatures indicating the lasing regime. Increasing the quality of the cavity mode induces a crossover from the solely superradiant to the lasing regime. Furthermore, we verify that lasing is manifested in a wide range of positive cooperative behaviour, showing that stimulated emission and superradiance can coexist. The robustness of the cooperativity is studied with respect to experimental imperfections, such as inhomogeneous broadening and pure dephasing.

2. **A quantum optical valve in a nonlinear-linear resonator junction**

   EPL 106, 54003 (2014)

Authors: Eduardo Mascarenhas, Daniel Valente, Simone Montangero, Alexia Auffeves, Dario Gerace, M. Franca Santos.

Electronic diodes, which enable the rectification of an electrical energy flux, have played a crucial role in the development of current microelectronics after the invention of semiconductor p-n junctions. Analogously, signal rectification at specific target wavelengths has recently become a key goal in optical communication and signal processing. Here we propose a genuinely quantum device with the essential rectifying features being demonstrated in a general model of a nonlinear-linear junction of coupled resonators. It is shown that such a surprisingly simple structure is a versatile valve and may be alternatively tuned to behave as: a photonic diode, a single or two-photon rectified source turning a classical input into a quantum output depending on the input frequency, or a quantum photonic splitter. Given the relevance of non-reciprocal operations in integrated circuits, the nonlinear-linear junction realises a crucial building component in prospective quantum photonic applications.

3. **A Fabry-Perot interferometer with quantum mirrors: nonlinear light transport and rectification**

Authors: F. Fratini, E. Mascarenhas, L. Safari, J-Ph. Poizat, D. Valente, A. Auffeves, D. Gerace, M. F. Santos.

Optical transport represents a natural route towards fast communications, and it is currently used in large scale data transfer. The progressive miniaturisation of devices for information processing calls for the microscopic tailoring of light transport and confinement at length scales appropriate for the upcoming technologies. With this goal in mind, we present a theoretical analysis of a one- dimensional Fabry-Perot interferometer built with two highly saturable nonlinear mirrors: a pair of two-level systems. Our approach captures non-linear and non-reciprocal effects of light transport that were not reported previously. Remarkably, we show that such an elementary device can operate as a microscopic integrated optical rectifier.

4. **Equilibrium and Disorder-induced behaviour in Quantum Light-Matter Systems**

Authors: Eduardo Mascarenhas, Libby Heaney, M. C. O. Aguiar, Marcelo Franca Santos.

We analyse equilibrium properties of coupled-doped cavities described by the Jaynes-Cummings-Hubbard Hamiltonian. In particular, we characterise the entanglement of the system in relation to the insulating-superfluid phase transition. We point out the existence of a crossover inside the superfluid phase when the excitations change from polaritonic to purely photonic. Using an ensemble statistical approach for small systems and stochastic-mean-field theory for large systems we analyse static disorder of the characteristic parameters and explore the ground state induced statistics. We report on a variety of glassy phases deriving from the hybrid statistics. On-site strong disorder induces insulating behaviour through two different mechanisms. For disorder in the light-matter detuning, low energy cavities dominate the statistics allowing the excitations to localize and bunch in such cavities. In the case of disorder in the light-matter coupling, sites with strong coupling between light and matter become very

significant, which enhances the Mott-like insulating behaviour. Inter-site (hopping) disorder induces fluidity and the dominant sites are strongly coupled to each other.

5. **The work of quantum phase transitions**

Phys. Rev. E 89, 062103 (2014)

Authors: E. Mascarenhas, H. Braganca, R. Dorner, M. Franca Santos, V. Vedral, K. Modi, J. Goold.

Classical phase transitions (CPTs) are driven by a multitude of mechanisms such as particle or heat exchange with a reservoir. A characteristic trait of first order CPTs, e.g. water turning into ice, is an exchange of heat between the system and reservoir at constant temperature called the *latent heat*; this is the energy needed to go from one state of matter to another. Quantum phase transitions (QPTs), on the other hand, occur at zero temperature and are driven by changes in the system Hamiltonian, i.e., by extracting or performing work on the system. Here, we recast QPTs in the framework of non-equilibrium thermodynamics and show that the average and irreversible work are discontinuous at the critical point of a first order QPT, however we show that there is no correspondence with classical latency. Thus there is no quantum latency in first order quantum phase transitions.

6. **Non-universality of entanglement convertibility**

Phys. Rev. B 89, 235132 (2014)

Authors: Helena Braganca, Eduardo Mascarenhas, G. I. Luiz, C. Duarte, R. G. Pereira, M. F. Santos, M. C. O. Aguiar

Low order quantum phase transitions are well defined from a thermodynamic point of view: the discontinuity in the energy derivative of the corresponding order forbids adiabatic dynamics when going through the critical point. However, this approach fails for infinite order transitions which do not present such finite order singularities and therefore allow adiabatic dynamical evolution through the critical point. The question of how to convert one quantum state to another may also be stated under settings other than the adiabatic, for instance, the quantum informational approach of entanglement convertibility under extended local operations that recasts the system into two parts which operate locally. We analyse several phase transitions under the framework of local convertibility, including transitions of infinite order that may be detached from pre-existing symmetries. We show that the operational transitions are associated to the symmetry features of the system. Our results systematically indicate that alterations of the local convertibility may correspond to points of highly symmetric hamiltonians, which need not coincide with quantum phase transitions. In fact, we show operational transitions that do not correspond to phase transitions and the converse, phase transitions that do not correspond to operational transitions. Therefore, we show that this operational approach is a good detector of symmetries rather then criticality.

7. **Dynamics and statistics of nonequilibrium spin chains (in progress)**

Some of the chapters are directly connected, however, each chapter is independent and I tried making them self contained at least on an informative level.

Bibliography

[1] I. M. Georgescu, S. Ashhab, and Franco Nori, Rev. Mod. Phys. 86, 153 (2014).

[2] Maciej. Lewenstein, Anna Sanpera and Veronica Ahufinger, *Ultracold atoms in Optical Lattices: Simulating Quantum Many-Body Systems*, (Oxford 2012).

[3] Joseph W. Britton, et al., Nature 484, 489 (2012).

[4] Andrew A. Houck, Hakan E. Tureci and Jens Koch, Nature Physics 8, 292 (2012).

[5] U. Las Heras, A. Mezzacapo, L. Lamata, S. Filipp, A. Wallraff, E. Solano, arXiv:1311.7626.

[6] Alan Aspuru-Guzik and Philip Walther, Nature Physics 8, 285 (2012).

[7] Anders W. Sandvik, *Computational Studies of Quantum Spin Systems*, AIP Conf.Proc.1297 (2010).

[8] G. De Chiara, M. Rizzi, D. Rossini, S. Montangero, J. Comput. Theor. Nanosci. 5, 1277(2008).

[9] P. W. Anderson, Science, New Series, Vol. 177 (1972).

[10] Ryszard Horodecki, et al., Rev. Mod. Phys. 81, 865 (2009).

Contents

Part I

Optical and Collective Phenomena

Chapter 1

Cooperativity of a few quantum emitters in a single-mode cavity

1.1 Introduction

Standard Laser theory describes the light amplification through stimulated emission by independent emitters in a single electromagnetic cavity. In a few words, as a result of the cumulative effect of stimulated emission a Laser turns the white noise that pumps the emitters into a quasi-monochromatic output light from the cavity. The emitters are pumped by some external classical source while interacting with a cavity mode. In the Laser regime a significant amount of light accumulates inside the cavity and such field stimulates the emitters to emit again in the same mode yielding a strong light output sharply centred at the cavity-mode frequency. However, such a theory assumes that each emitter is weakly coupled to the cavity and the Laser effect can only be seen for macroscopic amounts of emitters. For decades this assumption was able to account for every lasing system. As technology progresses we were able to achieve strong coupling between cavity and emitters which open up the possibility of Lasing with fewer emitters, in fact, we now know that the Laser effect can be achieved with a single emitter in a cavity, given that they are strongly interacting.

In a setting where different quantum emitters strongly interact with the same cavity mode correlations emerge between the emitters. Such correlations may be translated into destructive or constructive interferences between the light they emit. This is the topic of the present chapter and we term it the cooperativity of the emitters. Most importantly, we show the implications of the cooperativity for systems that may enter the lasing regime.

The optical properties of N emitters interacting with the same electromagnetic environment are drastically different from those of N independent emitters, each interacting with its own reservoir. Signatures of cooperative behaviour in the spontaneous emission of an atomic ensemble were first discussed in the context of the celebrated superradiance decay [1], where constructive interference of the atomic dipoles leads to enhanced relaxation of the atomic population, and to the emission of an intense and delayed pulse of light [2].

More recently, the steady state properties of the light field emitted by such a medium have been theoretically investigated, assuming continuous incoherent pumping, both for what concerns

its spectral [3, 4] and statistical characteristics [5, 6, 7]. Subradiant and superradiant regimes have been defined and identified, respectively corresponding to the emission of less/more light than in the independent emitters case. In these works, a common electromagnetic environment for the quantum emitters is provided by a leaky cavity, which acts as a collective decay channel. Naturally, increasing the quality factor of the resonator can eventually induce lasing, such that both phenomena could be observed in the same system at different pumping rates, in principle.

In the weak coupling regime, the concept of cooperativity has been implicitly used in the literature by adiabatically eliminating the cavity mode in the theoretical description, as described, e.g., in Ref. [6]. However, even in this particular case there was no precise definition to measure such a quantity. In this chapter, we propose an operational measure to quantify the cooperativity of a few quantum emitters coupled to the same single-mode resonator. We show that it works well irrespective of the operating regime of the system (weak or strong coupling, good or bad cavity, etc.). In that sense, it is also universal. We also address the spectral and the statistical properties of the emitted radiation supporting our analysis with the cooperativity measure.

Specifically, we analyse an ensemble of two-level emitters and study their cooperativity with respect to experimentally addressable parameters. We show that the cooperativity assumes negative values at subradiance and positive values at superradiance, which clearly indicates the change of regime. As the cavity quality factor is increased, we observe a crossover to a lasing regime, where the cooperativity shows distinctive signatures below and above threshold that allow to identify the nonlasing-lasing crossover. In the good cavity regime, our measure can reasonably be used to define the lasing threshold (usually not well defined for lasers of few emitters) as the pump rate increases, and the cooperativity changes from negative to non-negative values. Furthermore we show that lasing is manifested in a wide range of positive cooperativity, showing that lasing and superradiance are distinct phenomena that can coexist: when each emitter is strongly coupled to the resonator mode, a *cooperative lasing* regime manifests by a delayed quenching of the laser at strong incoherent pumping. Finally, we analyse the robustness of cooperativity to experimental imperfections, such as inhomogeneous broadening and dephasing. From an experimental point of view, systems that might realize the present model include small assemblies of artificial atoms, such as semiconductor quantum dots in microcavities [8, 9], superconducting qubits coupled to microstrip line resonators [10], or defects in solid state cavities [11].

The chapter is organized as follows. In Sec. 1.2 we define the hamiltonian and master equation we have used, and discuss the numerical techniques used to solve the problem. In Sec. 1.3 we introduce a novel definition of cooperative fraction, which is able to discriminate between the various regimes of the model. In Sec. 1.4 we investigate the signatures of the superradiance-lasing crossover as a function of the incoherent pumping rate, while its robustness to external parameters is discussed in Sec. 1.5, with an emphasis on the role of the cooperativity as a valuable measurable quantity.

1.2   System, model and methods

The system under study is a single-mode electromagnetic cavity coupled to N two level emitters, as schematically pictured in Fig. 1.1a. The emitters are incoherently pumped and may be dephased or detuned from the cavity frequency. The model describing this system is the well known Tavis-Cummings Hamiltonian [12] describing a coupling between the electric dipoles of two-level-emitters and a cavity electric field mode and assumes that the matter-light coupling is much smaller than
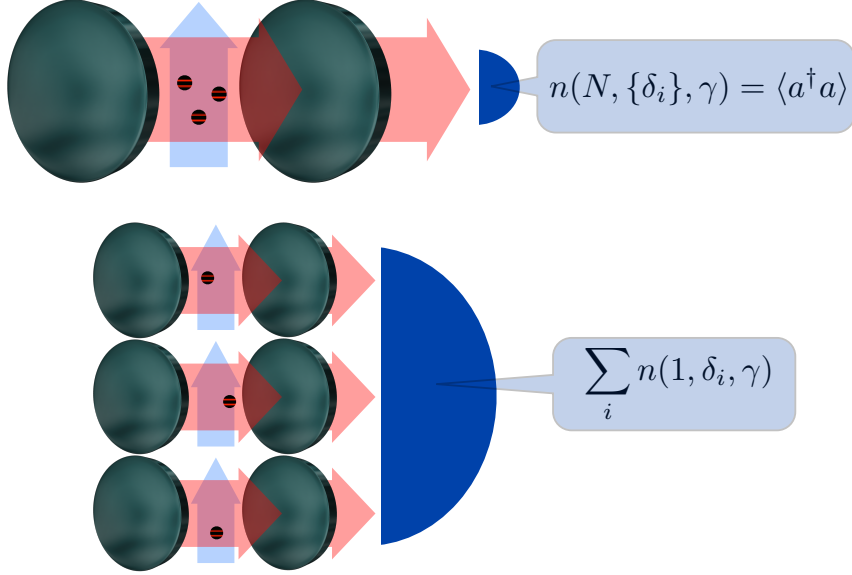
Figure 1.1: The system under investigation, and the operational definition of cooperativity. N emitters being incoherently pumped, two situations are compared. (a) A detector captures the output of a cavity containing the ensemble of emitters. (b) Each emitter is coupled to an individual cavity, and each output signal is assumed to be detected and summed.

the emitter's transition and mode frequency

$$H = \sum_{i}^{N} [\delta_i \sigma_i^\dagger \sigma_i + g(\sigma_i^\dagger a + \sigma_i a^\dagger)] \,, \tag{1.1}$$

with σ_i being the lowering operator for the ith emitter, a the annihilation operator for the cavity mode, δ_i the detuning of the ith atom from the cavity resonance, and g the light-matter coupling constant depending on the two-level system oscillator strength [14].

The incoherent processes, namely cavity losses, pumping of the emitters, and their pure dephasing are described with a Markovian approximation and Lindblad dynamics, with the Liouville-von Neumann equation of motion being written as (see, e.g., [16] for a rigorous derivation)

$$\dot{\rho} = \mathcal{L}(\rho) = -i[H, \rho] + k\mathcal{D}_a(\rho) + \sum_{i} [P\mathcal{D}_{\sigma_i^\dagger}(\rho) + \gamma\mathcal{D}_{z_i}(\rho)] \,, \tag{1.2}$$

with k being the rate of photon leakage from the cavity, P the incoherent pumping rate, γ the pure dephasing rate, and $z_i = \sigma_i^\dagger \sigma_i$. The Lindblad expression for an arbitrary operator, x, is given by

$$\mathcal{D}_x(\rho) = -\frac{1}{2}[x^\dagger x \rho + \rho x^\dagger x] + x\rho x^\dagger \,. \tag{1.3}$$

That is to say that such processes are approximated by white noise processes since they present extremely small correlation times. Such processes may also be though of as large quantum reservoirs that affect the system but are unaltered by the presence of the system.
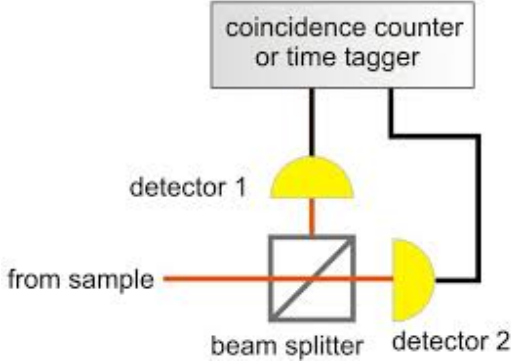
Figure 1.2: Schematic representation of a coincidence measurement and $g^{(2)}$.

In the following we focus on the stationary properties of the system and numerically compute the steady state values of the cavity population and atomic inversion, respectively. We also perform measurements of the cavity output field defined as [15]

$$b_{\text{out}}(t) = \sqrt{k}a(t) + b_{\text{in}}(t), \tag{1.4}$$

assuming that the vacum is the input field $\langle b_{\text{in}}(t)b_{\text{in}}^{\dagger}(t')\rangle = \delta(t - t')$ with all other correlations being zero. We evaluate the second-order coherence function at zero time delay of the cavity field, defined as [16]

$$g^2(0) = \frac{\left\langle b_{\text{out}}^{\dagger}b_{\text{out}}^{\dagger}b_{\text{out}}b_{\text{out}}\right\rangle}{\left\langle b_{\text{out}}^{\dagger}b_{\text{out}}\right\rangle^2} \propto \frac{\left\langle a^{\dagger}a^{\dagger}aa\right\rangle}{\left\langle a^{\dagger}a\right\rangle^2}, \tag{1.5}$$

which can be measured through a coincidence counting as illustrated in figure (1.2).

We also evaluate the cavity emission spectrum [15, 16]

$$S(\omega) = \int \lim_{\tau \to \infty} \left\langle b_{\text{out}}^{\dagger}(t + \tau)b_{\text{out}}(\tau)\right\rangle e^{i\omega t}dt, \tag{1.6}$$

which is the Fourier transform of the first-order correlation function. The latter can be calculated for the stationary state as $\left\langle b_{\text{out}}^{\dagger}(t)b_{\text{out}}(0)\right\rangle = k\left\langle a^{\dagger}(t)a(0)\right\rangle = k\text{tr}\left\{a^{\dagger}e^{\mathcal{L}t}a\rho_s\right\}$ (see equation 5.4.40 of [15]), with ρ_s being the steady state density matrix of the system.

The determination of the asymptotic state can be numerically done by standard sparse matrix diagonalization of the total Lindblad operator, such that $\mathcal{L}\rho_s = 0\rho_s$. In this work, we used a shift-and-invert Arnoldi method, which is coded in the ARPACK library that is built-in the MATLAB environment [17]. The time evolution needed to compute the correlation function is done with the Arnoldi method, which is the optimization of the matrix exponential in the Krylov subspace [18]. A brief description of the method is as follows. One needs to compute propagations of the form $\rho(t + \Delta t) = e^{\mathcal{L}\Delta t}\rho(t)$, with the major difficulty being the calculation of the matrix exponential.

This is done in the Krylov subspace, which is the subspace generated by the iterative application of the Lindblad matrix

$$\mathcal{K}_m[\mathcal{L}, \rho(t)] = \text{span}\left\{\rho(t), \mathcal{L}\rho(t), \mathcal{L}^2\rho(t), ..., \mathcal{L}^{m-1}\rho(t)\right\} . \tag{1.7}$$

This basis for the Krylov space can be ortho-normalized. In fact, the subspace can be constructed in orthonormal form by the modified Gram-Schmidt method. We call V the matrix whose columns are the orthonormal basis-vectors of the Krylov space. For the calculations shown in the present work, we have always kept 20 Krylov vectors. Thus, the huge numerical problem can be reduced to a small space by projecting the Lindblad into an upper Hessenberg form, $V^\dagger \mathcal{L} V = \mathcal{H}$. The eigenvalues of the Hessemberg matrix are called Ritz approximate eigenvalues of $\mathcal{L}$ which are good approximations for the extreme eigenvalues of $\mathcal{L}$, such that $\mathcal{H} = UDU^{-1}$. Finally, we have the solution (explicitly written in the most effective order of multiplication)

$$\rho(t + \Delta t) = V\left[Ue^{D\Delta t}U^{-1}\right]\left[V^\dagger\rho(t)\right] . \tag{1.8}$$

1.3 A measure of cooperativity

To quantify the cooperativity of the ensemble of emitters coupled to the same cavity mode, we compare the two situations that are schematically pictured in Fig. 1.1. We pump the N quantum emitters at the same rate, P. The emitters are either coupled to the same cavity mode $((a))$, or each of them is coupled to its own resonator (b). The output in the photonic channel, which is proportional to the emitted radiation in each case, is compared for the two situations above. The first situation gives rise to an output field (in units of k), that is $n(N, \{\delta_i\}, \gamma) = \langle a^\dagger a \rangle$. In the second case, we measure the sum of the outputs from each cavity, where each one contains a single emitter, which is written as $n(1, \delta_i, \gamma) = \langle a_i^\dagger a_i \rangle$. For a given set of initial conditions, such as pump/dissipation rates, atom-cavity couplings, etc., the system behaviour is said to be "cooperative" when the two measurements differ, the difference between them giving direct access to the field that is created or annihilated by cooperativity. Then, a cooperativity parameter, or cooperative fraction, can be defined as

$$C_f = \frac{n(N, \{\delta_i\}, \gamma) - \sum_i n(1, \delta_i, \gamma)}{n(N, \{\delta_i\}, \gamma)} . \tag{1.9}$$

By construction, this parameter is positive when cooperativity is constructive, while it necessarily assumes negative values for destructive cooperativity. It is worth stressing here that the absolute value of C_f as defined in the last equation is not bounded, i.e. it could be arbitrarily large if $\sum_i n(1, \delta_i, \gamma)$ is arbitrarily large. However, this will never be the case in situations one is usually concerned with, in particular the ones treated in the present work. The cooperative fraction tends to the limiting value of 1 for maximum constructive cooperativity, and it is ultimately bounded at negative values by the sum of the single emitters output for maximum destructive cooperativity.

It is wort mentioning straightforwardly that this parameter we are defining captures both cooperation in the quantum sense that the atomic states are mutually affected in case the emitters a made to interact with the same field but also cooperation in a semiclassical manner through stimulated emission. In a standard laser treatment [15] the emitters are assumed to be in quasi-dynamical-equilibrium with their individual inversion reservoirs. In this case there is no quantum

correlation between the emitters but their common presence in the same cavity generates an accumulation of photons in the cavity field. Our parameter does not distinguish between quantum cooperation and classical cooperation. In standard laser theory the phase space amplitude of the field (per emitter) can be approximately given by (see equation 9.3.78 of [15])

$$d\widetilde{\alpha} = -k\widetilde{\alpha} \left(1 - \frac{C}{1 + |\widetilde{\alpha}|^2/\widetilde{n}_0} \right) dt + dF, \tag{1.10}$$

with $\widetilde{\alpha} = \alpha/\sqrt{N}$. The factor C is the traditional cooperativity parameter given by $C = \frac{2Pg^2N}{P^2k}$ and $\widetilde{n}_0 = \frac{P^2}{8g^2N}$ is the so called saturation photon number. We may naively average over the stochastic Gaussian force $\langle dF \rangle = 0$ and look at the stationary solutions $\langle d\widetilde{\alpha} \rangle = 0$ of the amplitude recovering a semiclassical approximation (see equation 9.3.28 of [15])

$$\widetilde{\alpha} \left(1 - \frac{C}{1 + |\widetilde{\alpha}|^2/\widetilde{n}_0} \right) = 0, \tag{1.11}$$

which has two solutions: $\widetilde{\alpha} = 0$ if $C < 1$ and $\widetilde{\alpha} = \sqrt{\widetilde{n}_0(C-1)}$ if $C > 1$. In this approximation, that neglects quantum fluctuations, we have that the cavity photon number (per emitter) is the modulus squared of the amplitude $\widetilde{n} = |\widetilde{\alpha}|^2$. In the limit of validity of equation (1.10) $P \gg g$ and usually $k > g$, thus the standard C factor is very small unless theres is a macroscopic number of atoms $N \gg 1$ such that $\widetilde{n}(N) = \widetilde{n}_0(C-1)$ and $\widetilde{n}(1) \approx 0$. Hence, for the standard laser above threshold our definition of cooperativity reads

$$C_f = \lim_{\substack{N\to\infty \\ g\to 0}} \frac{\widetilde{n}(N) - N \times \widetilde{n}(1)}{\widetilde{n}(N)} = \lim_{\substack{N\to\infty \\ g\to 0}} \frac{\widetilde{n}_0(C-1) - N \times 0}{\widetilde{n}_0(C-1)} = 1. \tag{1.12}$$

This brief analysis confirms that even though the standard laser has no quantum cooperation it does have classical cooperation which is captured by our newly defined C_f. Furthermore, the cooperativity is null bellow threshold and 1 above threshold under this strong semiclassical approximation. But in reality the a smoother crossover.

We can also show that in the absence of stimulated emission C_f can also capture quantum interferences or cooperation. In the bad cavity regime ($k \to \infty$) the cavity may be eliminated (as the emitters were eliminated in the lasing regime) in this case we may explicitly write the output field in terms of the emitters operators. Assuming that the cavity is in quasi-equilibrium with its reservoir we may define the cavity field as the reservoir for the emitters in the Markovian approximation as $a = \frac{b_{\text{out}} - b_{\text{in}}}{\sqrt{k}}$ and thus $a_{\text{in}} = -\frac{b_{\text{in}}}{\sqrt{k}}$. In this limit the atom divides the cavity field into two regions, let us say left and right fields which we assume to be identical, thus a multiplication factor of two is included in the Hamiltonian. In the adiabatic elimination the hamiltonian describing the atomic dissipation is

$$H = 2g(Ja_{in}^\dagger + J^\dagger a_{in}) = -\frac{2g}{\sqrt{k}}(Jb_{in}^\dagger + J^\dagger b_{in}), \tag{1.13}$$

with $J = \sum_i^N \sigma_i$, $a_{\text{out}} = \frac{g^2}{k}J + a_{\text{in}}$ and the equation of motion being

$$\dot{\rho} = 4\frac{g^2}{k} \left[-\frac{1}{2}(J^\dagger J\rho + \rho J^\dagger J) + J\rho J^\dagger \right]. \tag{1.14}$$
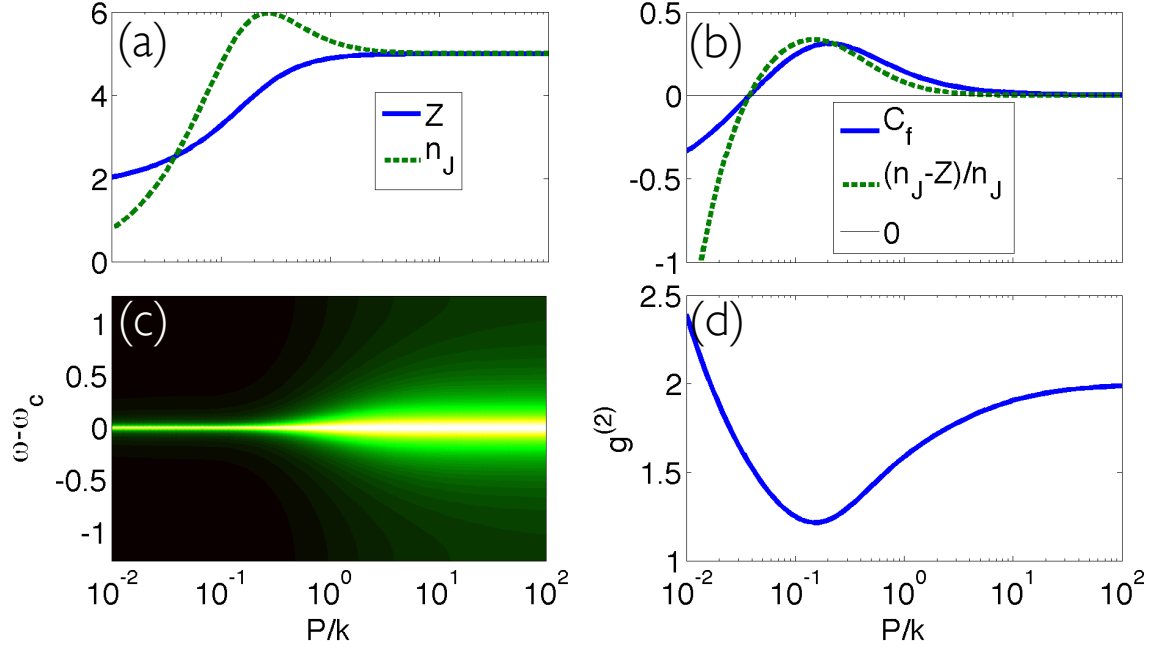
Figure 1.3: Subradiance and superradiance for 5 emitters in the bad cavity regime, $g = 0.1k$. (a) Total atomic inversion, Z, and average value of the total atomic dipole, $\langle J^\dagger J \rangle$; (b) Cooperative fraction compared to $(n_J - Z)/n_J$; (c) Cavity spectrum; (d) Second-order coherence function $g^2(0)$. All the data are plotted as a function of the pump rate.

Therefore in this limit the cavity works as a global collective decay channel for the emitters as expected. The output intensity is then given by $\langle n_{out} \rangle \propto \langle J^\dagger J \rangle$. Thus we have the cooperativity factor

$$C_f(k \to \infty) = \frac{\sum_{ij} \left[\langle \sigma_i^\dagger \sigma_j \rangle_{\text{collective}} - \langle \sigma_i^\dagger \sigma_i \rangle_{\text{individual}} \right]}{\sum_{ij} \langle \sigma_i^\dagger \sigma_j \rangle_{\text{collective}}} \tag{1.15}$$

$$= \frac{Z_{\text{collective}} - Z_{\text{individual}} + \sum_{i \neq j} \langle \sigma_i^\dagger \sigma_j \rangle_{\text{collective}}}{Z_{\text{collective}} + \sum_{i \neq j} \langle \sigma_i^\dagger \sigma_j \rangle_{\text{collective}}}, \tag{1.16}$$

with $Z_{\text{collective}} = \sum_i \langle \sigma_i^\dagger \sigma_i \rangle_{\text{collective}}$ and in this limit $Z_{\text{collective}} \approx Z_{\text{individual}}$ thus the factor C_f ends up measuring the direct impact of the atomic correlations on the output field.

As a first numerical test, we apply our definition of cooperativity to the bad cavity regime of the Tavis-Cummings model, where subradiant and superradiant regimes have already been theoretically characterized [6, 7]. We set the number of emitters to 5 and the coupling $g = 0.1k$, under which conditions the adiabatic elimination of the cavity mode is appropriate [19]: in this regime, a is proportional to the global atomic mode, defined by the collective dipole operator $J = \sum_i \sigma_i$. Cooperativity is usually evidenced by comparing the total atomic population inversion, $Z = \sum_i \langle \sigma_i^\dagger \sigma_i \rangle$, to the total atomic dipole $n_J = \langle J^\dagger J \rangle$ [19]: indeed, it directly compares the field emitted by

the atomic ensemble to the field that would be emitted by each two-level system in independent reservoirs. Figure 1.3a shows the evolution of these quantities as a function of pumping rate. As already discussed in Refs. [6, 7], a subradiant behaviour is manifested at low pumping $P < \Gamma$, where $\Gamma = 4g^2/k$ is the relaxation rate of a single emitter. It is due to the efficient optical pumping of the atomic ensemble into its dark states, and gives rise to the emission of highly bunched light [5, 7]. On the other hand, a superradiant regime is reached when $\Gamma < P < N\Gamma$, because of the preferential population of symmetrical Dicke states showing enhanced coupling to the electromagnetic field. Finally, when $P > N\Gamma$, the atomic population is totally inverted, such that each emitter behaves independently from the others [7]. Thus, superradiance (subradiance) is characterized by $n_J > Z$ ($n_J < Z$). In Fig. 1.3b we plot the cooperative fraction, which is negative in the subradiant regime, positive in the superradiant one and goes back to 0 at high pumping rates, as expected. In the same figure, we also plot the quantity $(n_J - Z)/n_J$, which provides an intuitive measure of cooperativity in the bad cavity regime, based on the analyses already performed in the literature and described above. As it can be seen, the parameter defined in the present work agrees qualitatively well with former studies, and can be used as a fair marker to describe the transition between subradiant to superradiant regimes, respectively.

As recently demonstrated, a huge ensemble of atoms coupled to a bad cavity can produce extremely coherent light, a phenomenon called "steady-state super-radiant laser" [13]. In this situation the coherence is to be attributed to the phase locking of the atomic dipoles, and not to the stimulated emission of one given mode of a high quality factor resonator. This result clearly shows the symmetry between steady-state superradiance and stimulated emission, both physical processes inducing an enhancement of the absorption properties of a medium because of bosonic amplification. Nevertheless, in the bad cavity regime, a lasing-like behaviour can only take place if the number of emitters is large enough, such that the matter field can be highly excited. This is not the case in the present few emitters situation. This appears in Figs. 1.3c and d where the spectrum and second-order coherence function of the cavity field have been plotted. As it can be seen, the second-order coherence does not lock to 1, and increasing the pump only broadens the spectrum. Hence in the case under study, the lasing character can only come from stimulated emission, which requires a high quality factor resonator. This is investigated in the following Section.

1.4   Superradiance-lasing crossover

In this Section we consider a regime of parameters in which lasing can take place, focussing our analysis on the respective contributions of stimulated emission and superradiance to positive cooperativity. We start from the case of $N = 2$, and we progressively increase the light-matter coupling, such that strong coupling regime is eventually reached for each individual atom-cavity system. We have plotted in Fig. 1.4a,c and d the cavity population, the second-order coherence function of the cavity field, and the total atomic inversion as a function of pumping rate, for g ranging from $k/100$ to $10k$. In addition to these quantities, which provide usual signatures of lasing, we have also plotted the newly defined cooperativity fraction (Fig. 1.4b). One can mainly distinguish three regimes for cooperativity, corresponding to the cooperative fraction being respectively negative, positive and null. Negative cooperativity still characterizes a subradiant regime, associated with the emission of a bunched light field.

In the case of positive cooperativity, the analysis performed in the bad cavity regime is valid as long as $g \leq k$. On the contrary, when $g > k$, two different behaviours emerge, as it clearly appears in the plots of Fig. 1.4. As a first step, the cooperative parameter C_f becomes positive
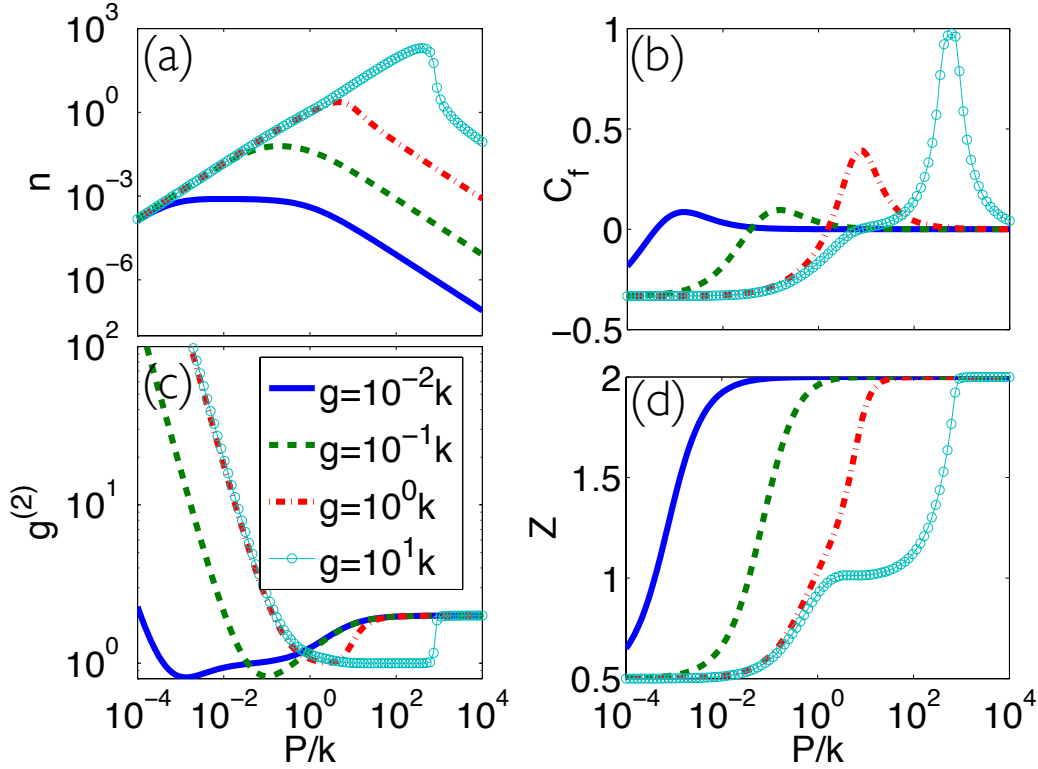
Figure 1.4: The superradiance-lasing crossover is shown for 2 emitters coupled to the same cavity mode: (a) cavity population, (b) cooperative fraction, (c) second-order coherence function, and (d) atomic inversion. The data are plotted as a function of pumping rate for different values of the emitter-cavity coupling constant.

and remains quite close to 0. The steady state cavity population increases drastically and the atomic inversion Z is clamped to 1. These are usual signatures of the lasing regime, confirming that stimulated emission takes place and that the non-linear regime is reached. Simultaneously, a plateau for $g^2(0) \simeq 1$ develops. Indeed, the emission of a Poissonian field induces the locking of the second-order coherence to 1 [20]. The crossover from non-lasing to lasing regime is captured by C_f. In particular, the switch from negative to positive provides a new way to define the lasing threshold in the few emitters case.

In a second step, as we further increase the pump, the cooperativity increases significantly while the system is deeply in the lasing regime. In particular, at the maximum value of cooperativity we have all the typical lasing signatures. In this situation indeed, the medium consisting of a few emitters is still lasing $n(N, \{\delta_i\}, \gamma) > 0$, while each single-emitter laser has quenched ($n(1, \delta_i, \gamma) \rightarrow 0$). Quenching takes place when the pumping power starts to overcome the effective light-matter coupling strength [25]. This strength scaling like the number of emitters (see next Section), the few emitters laser quenches for higher pumping power than the individual ones : this is a clear signature of cooperativity, which is captured by the parameter C_f defined in this study. This situation can
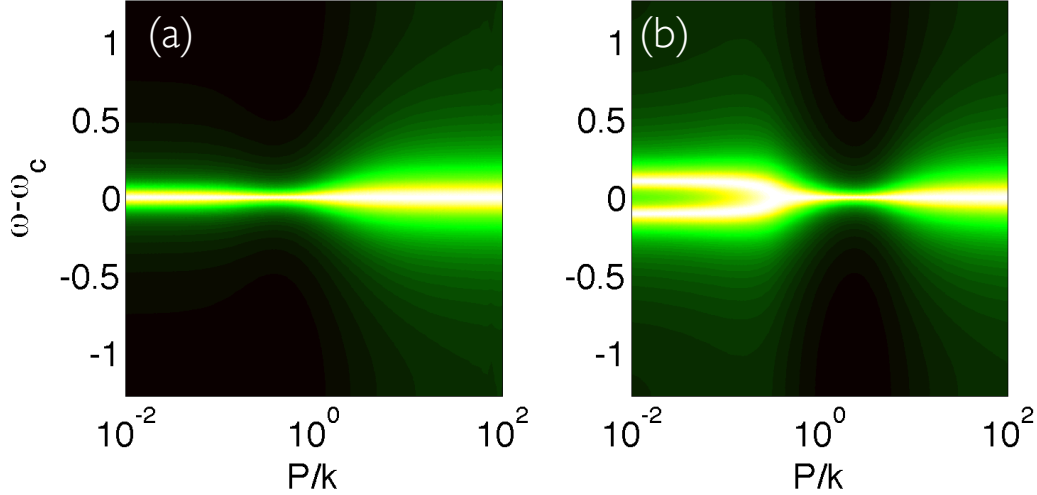
Figure 1.5: The spectral signature of superradiance-lasing crossover for 4 emitters coupled to the same cavity mode: spectrum of the emitted radiation vs. pumping rate for (a) $g = 0.2k$, and (b) $g = 0.5k$, respectively.

be described in terms of a strongly *cooperative laser*, pointing towards the coexistence of lasing and superradiant characteristics.

Finally the quenching regime appears at high pumping rates. In fact, for lager values of the pump the quenching of the laser begins, and the cooperativity starts decreasing back to zero. Under such conditions, power broadening spectrally decouples the lasing medium from the cavity mode, leading to a decrease of cavity mode population and the switching to a thermal statistics for the emitted field, i.e. $g^2(0) \to 2$. With respect to the cooperativity measure, quenching is clearly manifested by the simultaneous condition $C_f \to 0$.

The signatures of the crossover from plain superradiance to lasing should also appear in the spectral properties of the radiation emitted through the cavity mode. To confirm this behaviour, the results for the calculated spectra are shown in Fig. 1.5 for a larger number of emitters (4). The lasing crossover is clearly manifested by a visible narrowing of the emission spectrum in the lasing region. For $g = 0.5k$, at low pumping rates the spectrum is given by the Jaynes-Cummings doublet of each atom-cavity system, under which conditions the lasing narrowing is strikingly evident.

1.5   Influence of experimental parameters

In this section we focus on the evolution of the cooperativity fraction with respect to the parameters of the ensemble of emitters. In particular, we investigate the influence of the number of emitters, and the robustness of the cooperativity with respect to dephasing and inhomogeneous broadening.
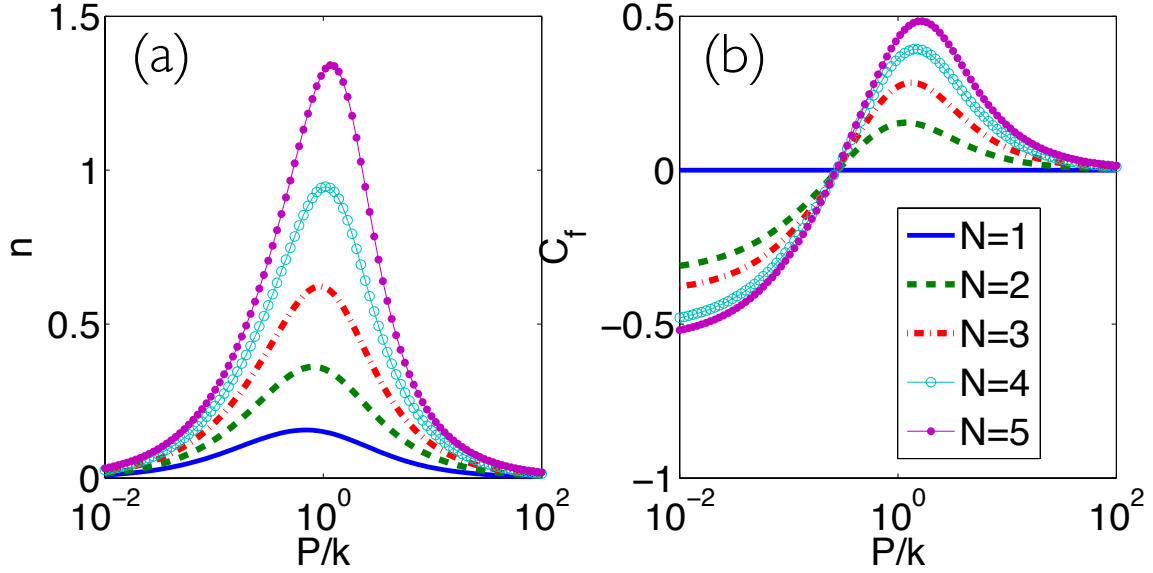
Figure 1.6: Influence of the number of emitters in the bad cavity regime, $g = 0.3k$: (a) cavity population, and (b) cooperativity fraction.

Cooperativity and number of emitters

The analysis of the emission properties of a mesoscopic number of emitters in a cavity by increasing the number one by one is a fruitful bottom-up approach, which was already taken in [7] to investigate the statistical properties of the emitted radiation, and paves the way to a novel description of the quantum-classical boundary. The results for the system parameters in the bad cavity regime are shown in Fig. 1.6. The maximum of the cavity population plotted in Fig. 1.6a increases drastically with the number of emitters, a behaviour already emphasized in [6], where such saturation value has been shown to evolve as N^2. In Fig. 1.6b, we can appreciate the corresponding evolution of the cooperativity fraction. In the subradiant regime, C_f decreases with the number of emitters: this can be interpreted by noting that the low excitation Dicke states are mainly populated on average, for which the decay rate typically scales as N. As a consequence, the larger N, the faster the relaxation, which leads to a lower excitation of the matter field at equal pumping rate and fully justifies the behaviour of C_f. As expected, C_f switches from negative to positive values for $P = \Gamma$, which does not depend on the number of emitters. On the contrary, and as it also appears in the Figure, the system returns to an independent-like behaviour when $P = N\Gamma$, which occurs at larger and larger pumping rates on increasing N.

In the same spirit as above, we revisit now these properties in the case where the resonator has a good quality factor, so that each emitter is individually strongly coupled to the cavity mode ($g = 5k$). We have investigated the signatures of lasing for a medium consisting of a few identical quantum emitters, ranging from 1 to 3. Usual quantities, namely cavity population n, second-order correlation at zero time delay, $g^2(0)$, and population inversion (normalized to the number of emitters, Z/N) are plotted on the left side of Fig. 1.7. As previously, the regimes of subradiance, superradiance/lasing and quenching can be clearly identified. Subradiance is manifested in the low

pumping regime, by a negative cooperativity fraction and oscillations of the second order coherence function between even and odd numbers of emitters. These oscillations have been thoroughly analysed and already discussed in Ref. [7], essentially related to differences in the Hilbert space geometry of Dicke states participating in the driven/dissipative quantum dynamics, and depend on the parity of N. In particular, these oscillations are the signature of the energy spreading of the Dicke eigenstates, which depends on the parity of the number of atoms [7]. Another signature is the excitation of the matter field even in the low pumping case, as already mentioned: such an effect reflects the optical pumping in the dark states [6] and clearly appears in the plot of the population inversion. It can also be seen that the extension of the lasing regime as a function of the pumping strength is larger the larger is N, as saturation and quenching take place at larger pumping rates. For completeness, we have also reported the results for the single-emitter case, which has been thoroughly investigated in the literature [21, 22, 23, 24, 25, 26]. Again, both effects can be accounted for by the increase of the effective light-matter coupling, which scales as $\sqrt{N}$. On the right hand side of Fig. 1.7, we plot the cooperative fraction, the cavity population per emitter, n/N, and the cavity population per excited emitter, which is defined as n/Z. The influence of N on C_f is quite straightforward to analyse: increasing N increases the magnitude of the cooperativity fraction. In the subradiant regime, C_f is more negative, as in the bad cavity case. In the superradiant regime, the maximum C_f occurs at larger pumping, and it reaches larger values: this corresponds to the saturation and quenching of N cooperative emitters occurring at larger pump power as compared to the single-atom laser. The maximum cooperativity is reached in this very region where the cooperative medium is still lasing, while the single emitter medium has quenched. Switching from negative to positive cooperativity does not depend on N, as in the low Q resonator case. The same evolution can be seen in the parameter n/N.

Finally, we have studied the quantity n/Z (see Fig. 1.7f), which is the typical absorption per emitter. Its meaning in the single atom case is clear: in the spontaneous emission regime, the atomic inversion and the cavity population scale like the pump power, hence the ratio n/Z is constant and locked at the spontaneous emission rate. When the non-linear regime is reached, the population clamps while the cavity population is still increasing. Hence the parameter n/Z increases linearly with the pump power because of stimulated emission, a feature that clearly appears in the plot. Such behaviour would also appear for a standard lasing medium made of distinguishable atoms. On the contrary, for the microlaser investigated here, the switching from linear to non-linear behaviour is blurred out as soon as the medium involves more than a single emitter. As it can be seen in the plot, the average absorption per emitter continuously increases with respect to the pump power. Indeed, here the increase in the absorption is the result of two contributions: before the lasing threshold, it is due to the displacement of the equilibrium in the Dicke states phase space toward higher excitation states characterized by higher coupling to the light field (steady state superradiance). When lasing takes place, the absorption increase comes from stimulated emission. This behaviour is a major difference between standard lasing media made of distinguishable atoms and the specific medium investigated here. At the highest powers the drop-off in n/Z is attributed to quenching, which describes the decrease in the absorption of the atomic medium when the pump power becomes too high. This effect is due to the broadening of the atomic emission line at high excitation power [25].

Cooperativy vs. dephasing/inhomogeneous broadening

So far we have assumed the quantum emitters to be identical, on resonance with the cavity mode, and non-dephased. Now we relax this latter constraint and analyse how detuning (i.e. inhomogeneous broadening) and dephasing affect the cooperativity. Both of these effects are relevant in solid state implementations of the model studied in this work, such as in a quantum dot laser [8]. We consider a system of two emitters equally detuned from the single-mode cavity frequency, and compute their cooperativity as a function of detuning for different regimes of the pumping rate. The results are plotted in Fig. 1.8a. As it appears in the plot, increasing the detuning may actually increase the cooperativity, even though the total atom-cavity coupling decreases. This increase is due to the fact that the cavity population in the single emitter is more sensitive to detuning. Thus, while the single emitters are being decoupled from their cavities the cooperative emitters sustain the cavity population. For low pumping regimes the system may be driven from subradiant to superradiant regime. We refer to this positive cooperative regime as superradiant instead of lasing, since it lacks other characteristic features of lasing, such as spectral narrowing (not shown here). For larger values of the pumping rate, the system behaves as a regular laser, as already established. In this regime the cooperativity also presents a maximum as a function of the detuning even though, once again, the effective atom-cavity coupling only decreases. Finally and as expected, for large detuning the cooperativity tends to zero.

Interestingly, a similar behaviour is found by adding pure dephasing to the emitters, as shown in Fig. 1.8b. However, it is clear that the cooperativity is much more sensitive to detuning rather than dephasing. We also point out that detuning the emitters asymmetrically (not shown here) with respect to the cavity frequency, or non equally detuning them, usually leads to less cooperativity as compared to the case in which the emitters are symmetrically detuned around the cavity mode frequency. This sensitivity is due to the fact that the resonator couples to the symmetric "brilliant" state of the two emitters, which remains identical if the two emitters are detuned symmetrically with respect to the mode.

1.6   Conclusion

In conclusion, we have introduced a new operational quantity to measure the degree of cooperativity in the emission characteristics of a system of few incoherently pumped emitters coupled to a single-mode cavity. It is defined by comparing the photon emission of an ensemble of emitters coupled to the same cavity mode with the overall emission of the same emitters each one individually coupled to its own resonator mode. We have shown how such a quantity is able to quantitatively describe the crossover between steady state subradiance, superradiance, and lasing. We have analysed the effects of inhomogeneous broadening and pure dephasing on cooperativity, which might be relevant in solid state implementations of this model. We have shown that in the good cavity regime, a few indistinguishable two-level systems provide a new type of lasing medium as compared to an ensemble of distinguishable emitters. These results are quite promising for emerging experiments in mesoscopic quantum optics, where a bottom up approach allows the possibility to sequentially add an increasing number of emitters coupled to the same cavity mode.
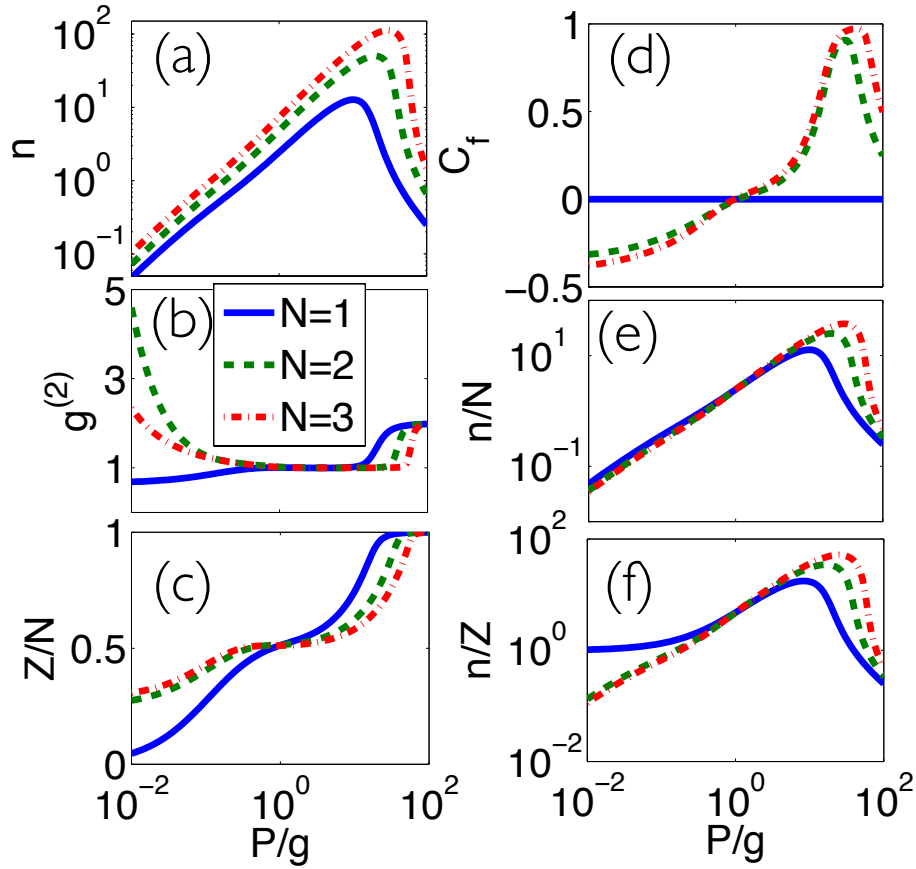
Figure 1.7: Subradiance and lasing in the strong coupling regime for increasing number of emitters, i.e. $g = 5k$: (a) cavity population, (b) second-order correlation function, (c) population inversion per emitter, (d) cooperative fraction, (e) cavity population per emitter, (f) cavity population per excited emitter. The data are shown for one emitter (blue continuous), two (green dashed) and three (red dashed-dotted) emitters, respectively. All the data are plotted as a function of the pumping rate.
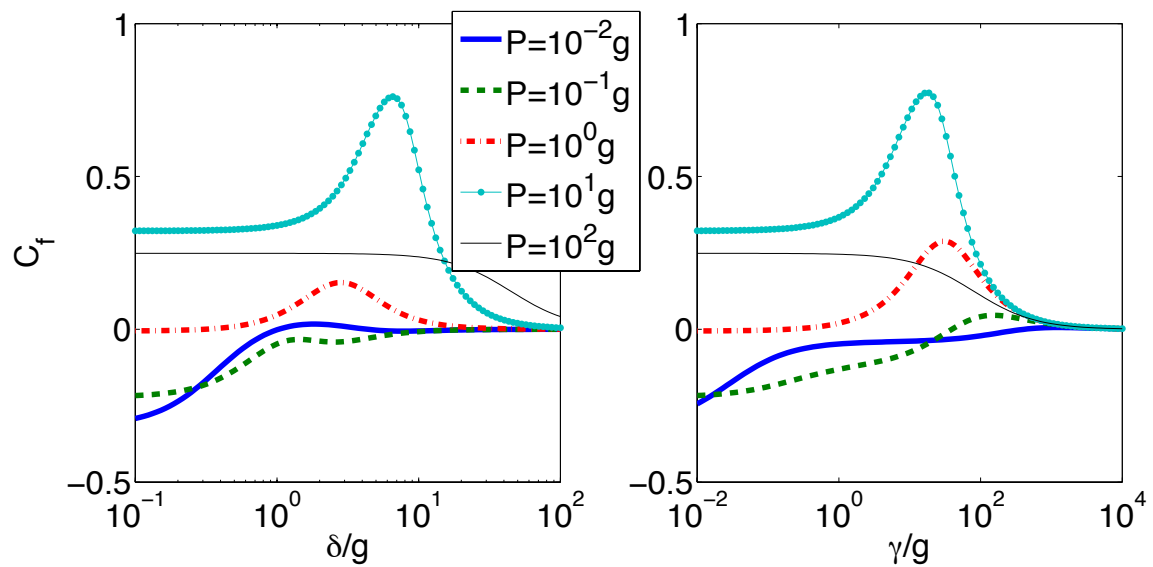
Figure 1.8: Cooperativity fraction in the two-emitter case: (a) as a function of (symmetric) detuning from the cavity resonance frequency, (b) as a function of pure dephasing rate (and zero detuning). We considered the strong coupling regime $g = 5k$.

Bibliography

[1] R. H. Dicke, Phys. Rev. **93**, 99 (1954).

[2] M. Gross and S. Haroche, Phys. Rep. **93**, 301 (1982).

[3] A. N. Poddubny, M. M. Glazov, and N. S. Averkiev, Phys. Rev. B **82**, 205330 (2010).

[4] F. P. Laussy, A. Laucht, E. del Valle, J. J. Finley, and J. M. Villas-Bôas, Phys. Rev. B **84**, 195313 (2011).

[5] V. V. Temnov and U. Woggon, Optics Express **17**, 5774 (2009).

[6] D. Meiser and M. J. Holland, Phys. Rev. A **81**, 033847 (2010); D. Meiser and M. J. Holland, Phys. Rev. A **81**, 063827 (2010).

[7] A. Auffeèves, D. Gerace, S. Portolan, A. Drezet, and M. F. Santos, New J. Phys. **13**, 093020 (2011).

[8] S. Strauf, K. Hennessy, M.T. Rakher, Y.-S. Choi, A. Badolato, L.C. Andreani, E.L. Hu, P.M. Petroff, and D. Bouwmeester, Phys. Rev. Lett. **96**, 127404 (2006).

[9] A. Surrente, M. Felici, P. Gallo, B. Dwir, A. Rudra, G. Biasiol, L. Sorba, and E Kapon, Nanotechnology **22**, 465203 (2011).

[10] L. DiCarlo, J.M. Chow, J.M. Gambetta, L.S. Bishop, B.R. Johnson, D.I. Schuster, J. Majer, A. Blais, L. Frunzio, S.M. Girvin, and R.J. Schoelkopf, Nature (London) **460**, 240 (2009).

[11] A. Faraon, P.E. Barclay, C. Santori, K.M.C. Fu, and R.G. Beausoleil, Nat. Photonics, **5**, 301 (2011).

[12] M. Tavis and F. W. Cummings, Phys. Rev. **170**, 379 (1968).

[13] J.G. Bohnet, Z. Chen, J.M. Weiner, D. Meiser, M.J. Holland, J.K. Thompson, Nature **10920**, 78 (2012).

[14] L. C. Andreani, G. Panzarini, and J.-M. Gérard, Phys. Rev. B **60**, 13276 (1999).

[15] C. Gardiner and P. Zoller, *Quantum noise* (Springer, 2004).

[16] H. J. Carmichael, *An open systems approach to quantum optics* (Springer-Verlag, Berlin, 1993).

[17] Y. Saad, *Numerical methods for large eigenvalue problems* (Manchester University Press, Manchester, UK, 1995).

[18] M. Knap, E. Arrigoni, and W. von der Linden, Phys Rev. A **83**, 023821 (2011).

[19] V. V. Temnov and U. Woggon, Phys. Rev. Lett. **95**, 243602 (2005).

[20] R. Loudon, *The Quantum Theory of Light* (Clarendon Press, Oxford, 1983).

[21] Y. Mu and C. M. Savage, Phys. Rev. A **46**, 5944 (1992).

[22] C. Ginzel, H. J. Briegel, U. Martini, B.-G. Englert, and A. Schenzle, Phys. Rev. A **48**, 732 (1993).

[23] M. Löffler, G. M. Meyer, and H. Walther, Phys. Rev. A **55**, 3923 (1997).

[24] E. del Valle, F.P. Laussy, and C. Tejedor, Phys. Rev. B **79**, 235326 (2009).

[25] A. Auffèves, D. Gerace, J.-M Gérard, M. F. Santos, L. C. Andreani, and J.-P. Poizat, Phys. Rev. B **81**, 245419 (2010).

[26] E. del Valle and F. P. Laussy, Phys. Rev. A **84**, 043816 (2011).

Chapter 2

A quantum optical diode in a nonlinear-linear resonators junction

2.1 Introduction

The electrical diode in a semiconductor p-n junction is the prototype of a rectifying device that allows non-reciprocal electronic transport, which is key to information processing in integrated circuits [1]; a number of applications currently require the realization of devices enabling unidirectional energy transport, from thermal [2, 3, 4] and acoustic [5, 6] rectifiers, to all-optical diodes [7, 8]. The latter have now been attained in different configurations on-chip [9, 10, 27], although always at the level of classical (i.e. many photons) signal transmission. A quantum optical rectifier may be generally defined as a two terminal, spatially nonreciprocal device that allows unidirectional propagation of single- or few energy quanta at a fixed signal frequency and amplitude. This conceptual extension of the classical diode operation can be foreseen to be important in the context of future applications in, e.g., integrated quantum photonics [12], where novel quantum devices as single-photon transistors [13] and interferometers [14] have already been proposed, and where tunable rectification of quantum states is likely to play a role analogous to electrical diodes in current microchips. However, proposals for quantum optical rectification have been quite limited in the literature, to date. A device relying on non reciprocity induced by an external magnetic field in a doubly polarized waveguide has been proposed as a single-photon diode [15], where only conditional non-reciprocity depending on the specific polarization of the input state was shown. Unconditional quantum optical diodes and transistors have also been introduced in the context of atomtronic circuits [16], where an analogy between one-dimensional optical lattices with cold atoms and electronic circuits was exploited to suggest equivalent atom-based circuits over many sites.

In this chapter we go beyond previous works, and describe a general scheme for a quantum optical device that works as an unconditional rectifier, elaborating on the simple analogy between the traditional p-n junction in semiconductor physics and a single nonlinear-linear (n-l) junction of two coupled resonators, as the building block of an elementary quantum optical valve. In particular, we show that this valve can be tuned to control energy transport at the quantum level with direct

applicability to current quantum technologies. Under a continuous monotonic pump the junction behaves as a rectified single or two photon source, depending on the input frequency, thus turning a classical input into a quantum output. At difference with previous investigations, we will use second-order photon correlation as a probe of the quantum behaviour of the device: a single-photon rectified source will be characterized by sub-Poissonian counting statistics in the transmitted signal, while a two-photon rectified source by its super-Poissonian one. We also show that the junction behaves as a diode for fully quantum two-photon Fock states, such that one photon activates the nonlinearity while the second photon is rectified. Finally, at high coupling between the resonators the junction splits the initial Fock state sending the two photons in opposite directions, thus acting as a quantum state splitter

2.2 The model

We start from the concept of generic wave diodes in a nonlinear chain of resonators [17]: a transmitted intensity at fixed incident amplitude and at the same frequency should be sensibly different in the two opposite propagation directions. To transfer these concepts to the quantum regime, we assume a chain of tunnel-coupled nonlinear sites, which can be generally described by the Bose-Hubbard model with single-particle interactions of the Kerr-type. We will specify our treatment to a minimal two-site Bose-Hubbard Hamiltonian ($\hbar = 1$)

$$H_{\text{n-l}} = \Delta_L a_L^\dagger a_L + \Delta_R a_R^\dagger a_R + \frac{U}{2} a_L^\dagger a_L^\dagger a_L a_L + J(a_L^\dagger a_R + a_L a_R^\dagger) \,, \tag{2.1}$$

such that the operator a_i is the annihilation operator for the quanta in the i-th site, U is the left site inter-particle interaction, and J is the coupling strength between the two sites (usually determined by evanescent tunnel-coupling), which describes a two-site (left L, and right R) n-l junction as schematically shown in Fig. (2.1). We expect such a model to present rectification since it can be made asymmetric and nonlinear which are the basic two ingredients for rectification [17]. We notice that the generality of such a model has been established by effectively describing a wide variety of physical systems, from cold atoms in optical lattices [18, 19], to strongly interacting photonic systems made with atoms coupled to optical resonators [20, 21] or optical fibres [22], spin chains [23], arrays of superconducting circuits [24]. or in open photonic devices, such as coupled arrays of nonlinear solid-state cavities [25]. In the latter case, the on-site inter-particle interaction can be given by strong radiation-matter coupling of a single qubit-cavity system [26], by enhanced Coulomb interaction of electron-hole pairs in semiconductor elementary excitations [27, 28], or by enhanced native nonlinearity of the bulk material thanks to the strong field confinement [29]. In the case of weak nonlinearities, quantum interference between coupled modes can be exploited to reduce the final modeling of the system to an effective Hubbard model in Eq. 2.1, as proposed in Refs. [30, 31]. In the latter case, applications would imply fully passive quantum photonic devices compatible with standard materials employed in optoelectronics [32].

Before proceeding we give a brief derivation (very similar to [33]) of the nonlinear term of Kerr term for a generic nonlinear medium. We make a few simplifications in order to present a clearer and lighter derivation. We assume we are dealing with a single electromagnetic field in one-dimension such that the nonlinear response to an applied electric field is

$$D(x)/\epsilon_0 = \sum_n \chi^{(n)} E^n(x). \tag{2.2}$$
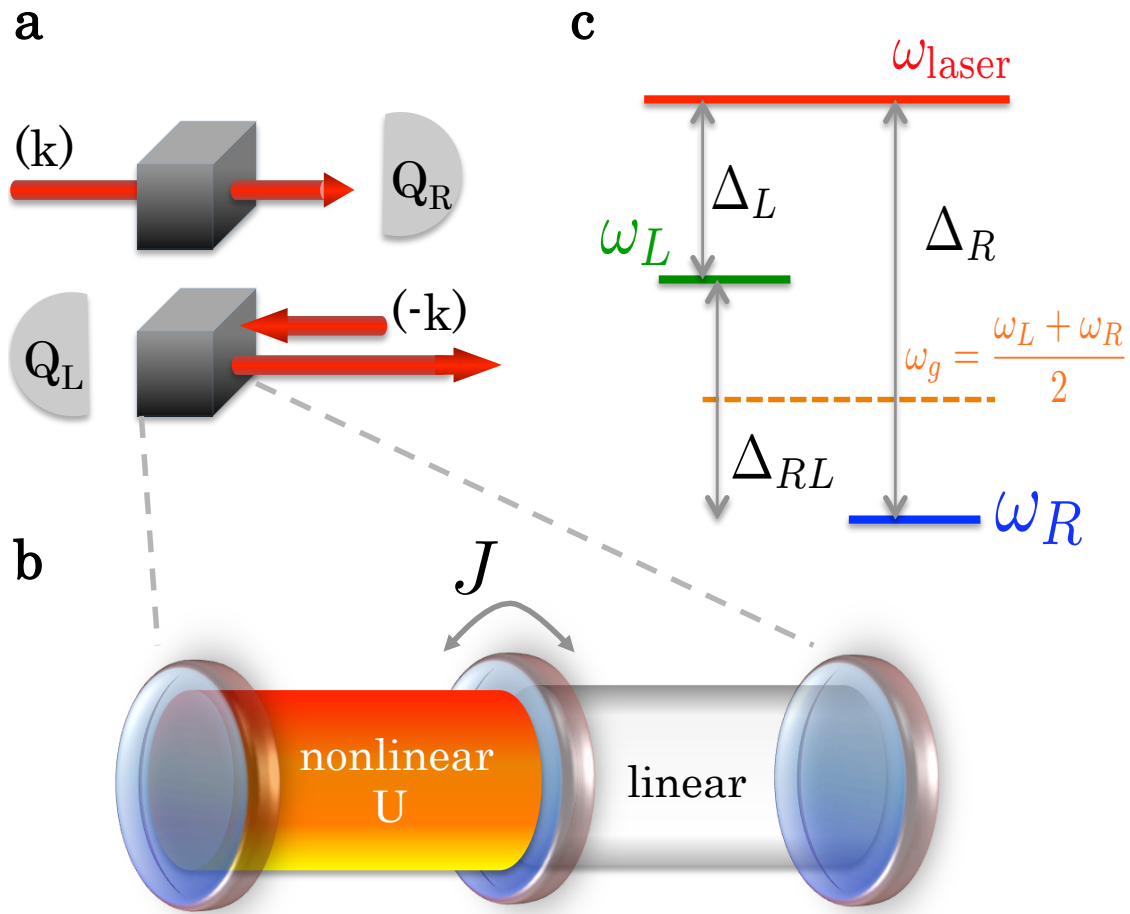
Figure 2.1: **Nonlinear-linear resonators junction** (a) Pictorial representation of a right-rectifying "black box" being pumped from left to right and then from right to left, with the transmission being significantly higher to the right. (b) Representation of light confining coupled resonators, one of which embedded in a nonlinear medium. (c) The representation of the frequencies and detunings of the driving laser and the resonators.

We also assume that that due to symmetry there is no second order nonlinearity and that the terms of 4th order or higher are much smaller than the third order term. The electromagnetic field is given by

$$E(x) = i \left(\frac{\hbar\omega}{2\epsilon_0} \right)^{1/2} \left[a \frac{\alpha(x)}{\epsilon(x)} e^{-i\omega t} - \text{h. c.} \right], \quad \int |\alpha(x)|^2 dx = 1 \tag{2.3}$$

whose energy is given by

$$H = \frac{1}{2} \int \left[ED + HB \right] dx = \frac{1}{2} \int \left[\epsilon_0 E^2 + \frac{B^2}{\mu_0} \right] dx + \frac{1}{2} \int \epsilon_0 \chi^{(3)} E^4(x) dx. \tag{2.4}$$

The first integral leads to the usual harmonic oscillator term $\omega a^\dagger a$. The second integral leads to the nonlinear term $\frac{U}{2} a^\dagger a^\dagger a a$ with

$$U = (2)6 \frac{(\hbar\omega)^2}{8\epsilon_0} \int \frac{\chi^{(3)}(x)}{\epsilon(x)} |\alpha(x)|^4 dx = (2)6 \frac{(\hbar\omega)^2 \overline{\chi^{(3)}}}{8\epsilon_0 \bar{\epsilon} V_{\text{eff}}}, \tag{2.5}$$

where we have derived the average approximate nonlinearity and permittivity and the effective volume $V_{\text{eff}}^{-1} = \int |\alpha(x)|^4 dx$. In such derivation we have made use of the rotating-wave-approximation, that is, in the fourth power of the field only the terms with the same power of destruction and creation operators survives. There are 6 such terms $a^\dagger a^\dagger a a$, $a^\dagger a a^\dagger a$ and so on. In these terms the complex time dependent exponentials are canceled while in all other terms there are rapidly rotating exponentials such as $aaaa e^{-i4\omega t}$, $a^\dagger aaa e^{-i3\omega t}$ and such exponentials generate a null average effect since they complete many cycles in a typical time it takes for the system to evolve.

Owing to its out-of-equilibrium nature, the system dynamics is necessarily described by a balance between driven-dissipative terms, as it is typical of quantum optical systems [16, 14, 26]. Either the left or right site of the junction can be coherently pumped, which is described by the Hamiltonian $H_p = F_i a_i^\dagger + F_i^* a_i$, with F_i being the driving strength, where $H_{\text{n-l}} + H_p$ is written in a reference frame rotating with the pumping frequency, ω_{laser}, with $\Delta_i = \omega_i - \omega_{\text{laser}}$ such that ω_i is the ith site characteristic frequency. The level configuration is schematically shown in Fig. (2.1-c).

We assume that the cavities (or sites) incoherently dissipate energy at a rate γ determined by the openness of each site into the output channels (e.g., one-dimensional waveguides), and we define the output currents as number of quanta emitted per unit time from each site, i.e. $q_i(t) = \gamma \langle a_i^\dagger a_i \rangle(t)$. Formally, the average number of quanta emitted from the ith cavity during a time interval $\Delta t = t_2 - t_1$, which is ideally the number of "clicks" registered as a photo-current in a single-photon detector, can be expressed as [34, 35]

$$Q_i(t_2, t_1) = \int_{t_1}^{t_2} q_i(t) dt, \tag{2.6}$$

and the time-dependent quantum state of the two-site system is determined by the Liouville-von Neumann equation in Lindblad form [34, 35, 36]

$$\dot{\rho} = \mathcal{L}(\rho) = -i[H_p + H_{\text{n-l}}, \rho] + \mathcal{L}_L(\rho) + \mathcal{L}_R(\rho), \tag{2.7}$$

with

$$\mathcal{L}_i(\rho) = -\frac{\gamma}{2} [a_i^\dagger a_i \rho + \rho a_i^\dagger a_i - 2a_i \rho a_i^\dagger], \tag{2.8}$$

describing the energy dissipation from each site. Note that Eq.(2.7) faithfully describes any physical implementation of this model in the standard Markovian open system formalism [34, 35]. If, for experimental or practical reasons, the output channels of the system are waveguides, the model properly describes the physical scenario in which these waveguides are independent and broadband.

With the dynamics and measurement processes specified, we define the rectifying factor as the normalized difference between the output currents when the chain is pumped through the left and right resonator (indicated by the wave vectors k and $-k$, respectively)

$$\mathcal{R} = \frac{Q_R[k] - Q_L[-k]}{Q_R[k] + Q_L[-k]},\tag{2.9}$$

such that the $\mathcal{R}$ factor measures the absolute rectification of the system: $\mathcal{R} = -1$ indicates maximal rectification with enhanced transport to the left (left rectification), $\mathcal{R} = 0$ indicates no rectification, while $\mathcal{R} = +1$ indicates maximal rectification with transport to the right (right rectification). We also define the transport efficiency which is the amount of light that is transported to the desired direction. The transport efficiency to the right is given by

$$T_R = \frac{Q_R[k]}{Q_R[k] + Q_L[k]}.\tag{2.10}$$

Left efficiency T_L is given analogously by interchanging R with L and k with $-k$. We notice that the photo-detection time interval, Δt, can be taken as arbitrarily small in continuous-wave pumping and steady state regime, but it should be taken large enough in case of pulsed excitation in order to fully integrate the emitted pulses.

As an effective probe of quantum nonlinear features of this device, we calculate the coincidence counting statistics of the emitted light. This is defined by the second order correlation function at zero time-delay, which is an experimentally relevant quantity and can be measured in a Hanbury Brown-Twiss (HBT) set-up with two single-photon detectors and a beam splitter [37], theoretically given by

$$g_i^{(2)}(\pm k) = \frac{\langle a_i^\dagger a_i^\dagger a_i a_i \rangle_{(\pm k)}}{\langle a_i^\dagger a_i \rangle_{(\pm k)}^2}.\tag{2.11}$$

This function gives values below unity for antibunched and above unity for bunched photons, respectively [36]. Antibunching corresponds to a reduced probability that two photons are detected in coincidence at a given time, while it is the opposite for bunching.

2.3 Results

Let us initially focus on Fig. (2.2), where we show the low U/γ regime of the system under continuous pump, for which we probe the n-l junction by scanning the laser frequency for a fixed Δ_{RL}. First, we turn our analysis to the full equilibrium quantum picture of the low lying eigenstates of the Hamiltonian 2.1, more specifically focussing on the nonlinear cavity. This is justified for two reasons: at this point we will address the regime of low tunnelling between cavities and low pump intensities. Therefore, only the low photon states can be probed and only if they are close to resonance with the laser, and due to the low tunnelling the nonlinear effects can be directly associated to the states of the nonlinear resonator. In Fig. (2.2-a) a maximum of left rectification corresponds to the condition $\omega_g - \omega_{\text{laser}} = -10\gamma$, which simultaneously shows anti-bunched emission
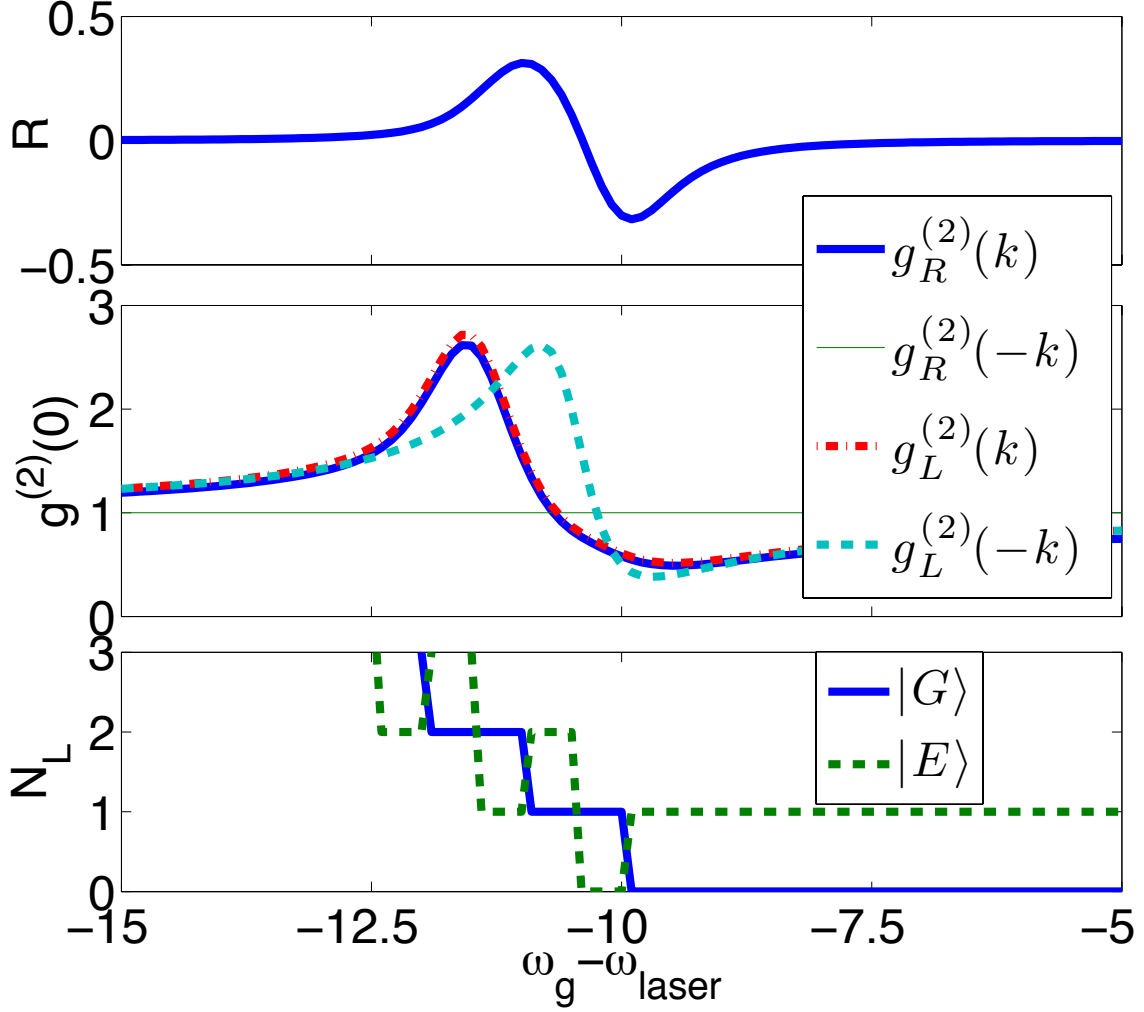
Figure 2.2: **Non-equilibrium rectification under continuous-wave pumping, and the corresponding equilibrium excitations of the low-lying eigenstates probed by tuning the laser frequency.** We show the rectification factor $\mathcal{R}$ (top panel), the second-order coherence function $g^{(2)}$ of the output light in both directions (middle), and the number of excitations in the left resonator, $N_L = \langle a_L^\dagger a_L \rangle$, for the ground and first excited states of the bare hamiltonian (1) (bottom). Parameters are: $U = \gamma$, $J = 0.1\gamma$, and $F = 0.5\gamma$. We assume $\Delta_{RL} = 20\gamma$ with $\Delta_L = \Delta_{RL}/2 + \omega_g$ and $\Delta_R = -\Delta_{RL}/2 + \omega_g$.
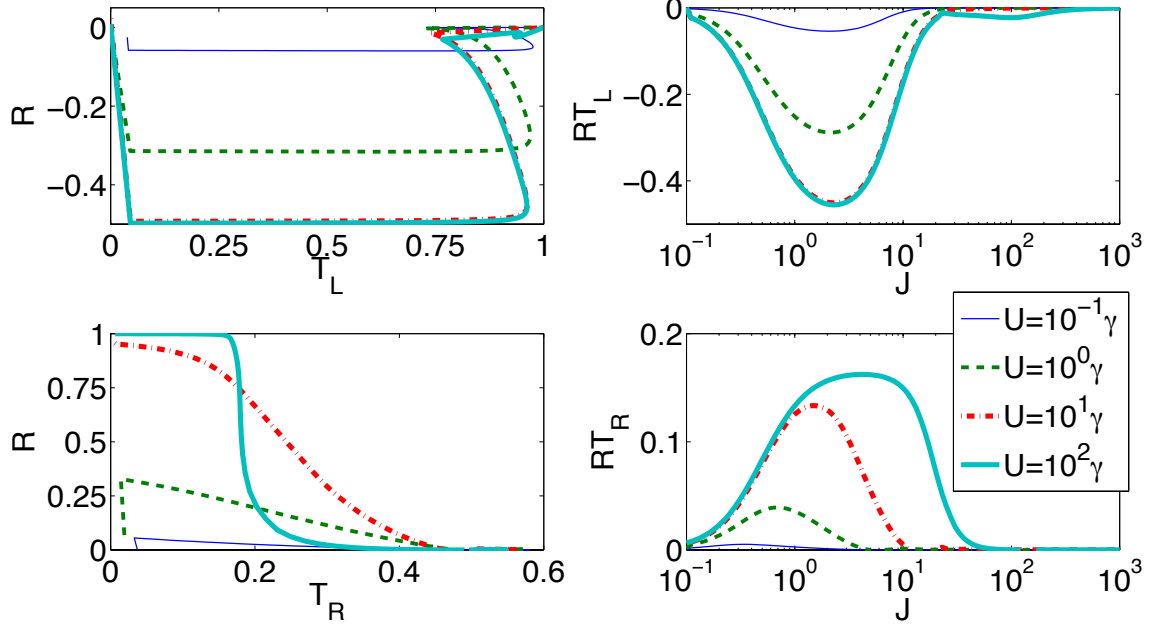
Figure 2.3: **Rectification and the corresponding transport efficiencies with frequency optimization.** (Top Left) Parametric plot of the optimized rectification and transport efficiency to the left and (Top right) their corresponding product as a function of the resonators coupling with $\Delta_{RL} = 20\gamma$. (Bottom Left) Parametric plot of the optimized rectification and transport efficiency to the left and (bottom right) the corresponding product as a function of the resonators coupling with $\Delta_{RL} = 0$.

of the left site occurring exactly at the left cavity bare resonance (higher nonlinearities lead to stronger anti-bunching) in (2.2-b). At the same time, in the equilibrium picture the population of the left resonator in the global ground state, $N_L = \langle a_L^\dagger a_L \rangle$, switches from zero to one [see Fig. (2.2-c)] while the population of first excited state switches from one to zero ($|0\rangle \leftrightarrow |1\rangle$), thus showing that this process is predominantly a single photon process (as further confirmed by the anti-bunching statistics). In this case the junction turns the classical input into a quantum output, working as a rectified single photon source. On the other hand, the right rectifying process (bunched light) is predominantly a two photon process (with resonance condition $\Delta_L + U \approx 0$, where the nonlinearity compensates for the detuning), as it can be observed in the low eigenstates excitations, where there is a switching from one-photon to two-photons state ($|1\rangle \leftrightarrow |2\rangle$). With this low lying states analysis we can fully connect the equilibrium properties of the system with its non-equilibrium response as a driven-dissipative quantum diode for one and two photons.

The analysis is further completed by addressing the transport efficiency and its relation to the rectification factor. In Fig. (2.3) we show the figures of merit given by the products $\mathcal{R}T_{L(R)}$, which characterize the total diode efficiency while optimizing over the input frequency. As expected, we can see that the rectification is small for small nonlinearity in the left site. For nonlinearities comparable to the dissipation rate, the system presents a left rectification factor of about 0.3,

and the corresponding transport efficiency increases with the tunnel coupling, J, until the system becomes generically a good conductor and the rectification factor tends to decrease. Therefore, there is a minimum of the product $\mathcal{R}T_L$, corresponding to the highest rectification at highest transport efficiency. Increasing the nonlinearity leads to products of about 0.5, which is ultimately limited by the rectification factor. As shown in Fig. (2.3), this device may achieve almost perfect transport together with a 0.5 rectification factor. As expected from the previous analysis, the best diode efficiency is reached when the input frequency is resonant with the nonlinear (left) resonator. Analogously, we show in Fig. (2.3) the optimization of the right diode efficiency, $\mathcal{R}T_R$. In this case the rectification approaches unity with increasing U/γ, however the corresponding transport is typically smaller than 0.2. This amounts to lower, however significant, diode efficiency of the order of 0.15. in this case the maximum efficiency is obtained when the laser frequency approximately matches the detuning induced by the nonlinearity $\Delta_L \approx U/2$. It is interesting that there is a trade-off between transport efficiency and rectification, and in a sense this is the price paid by the versatility of the junction.

Now we address the behaviour of the junction when it receives a quantum state as an input, instead of a coherent field. In practice, this can be achieved by designing an incoming pulse that prepares a pure Fock state in one of the resonators with high fidelity [45]. Since the Kerr nonlinearity is only activated by two quanta (or higher) Fock states, the n-l junction is reciprocal for a single photon Fock state as an input. Thus, we study the case of the $|n=2\rangle$ state, such that one photon activates the nonlinearity while the other can be rectified. In Fig. (2.4) we show the rectification and transport efficiency as functions of the resonators detuning, for different values of the resonators tunnel coupling. Similarly to the continuous wave pumping scenario, we find regimes of left and right rectification. Maximum left rectification is found when the resonators are very close to resonance, while maximum right rectification is found when the detuning is compensated by the nonlinearity $U - \Delta_{RL} \approx 0$. Once again we observe a trade-off between rectification and transport efficiency as we increase the resonators coupling, with a maximum diode efficiency in the interval $10^0 < J < 10^1$. This trade-off yields an interesting effect in regimes of strong coupling. In fact, at large J the junction may split the initial 2-photon Fock state into two distinct wave packets that travel in opposite directions, irrespective of the direction of the incoming pump pulse, which is indicated by the 0.5 transport efficiency in both directions. More precisely, if J is two large the photons can be found in either resonator with the same probability and since the resonators dissipate at the same rate there is a 50% chance the photons are emitted in both directions.

The main challenges to any feasible implementation of the present proposal rely on the system parameters that can be realistically achieved in order to observe quantum diode operation, and the detectability of the second-order correlation signals. For the first, we refer to the ratio U/γ as the relevant figure of merit, where γ is directly related to the resonators quality factors through the obvious relation $Q = \omega/\gamma$. We point out two different architectures that could be used for the implementation, where highly nonlinear and high quality resonators can be fabricated: Superconducting microwave circuits with microstrip (or coplanar) transmission line cavities coupled to superconducting qubits [38], also referred to as *circuit quantum electrodynamics*, and semiconducting optical circuits, such as photonic crystal circuits in thin semiconductor slabs [39].

Superconducting microwave circuits. Recently, tremendous progress has been made in the field of microwave photonic circuits employing superconducting almost-dissipationless elements, such as microstrip transmission line cavities and superconducting qubits [38], also referred to as *circuit quantum electrodynamics*. In the regime of strong light-matter coupling between a single qubit and a single mode of the superconducting resonator, the system nonlinearity is effectively
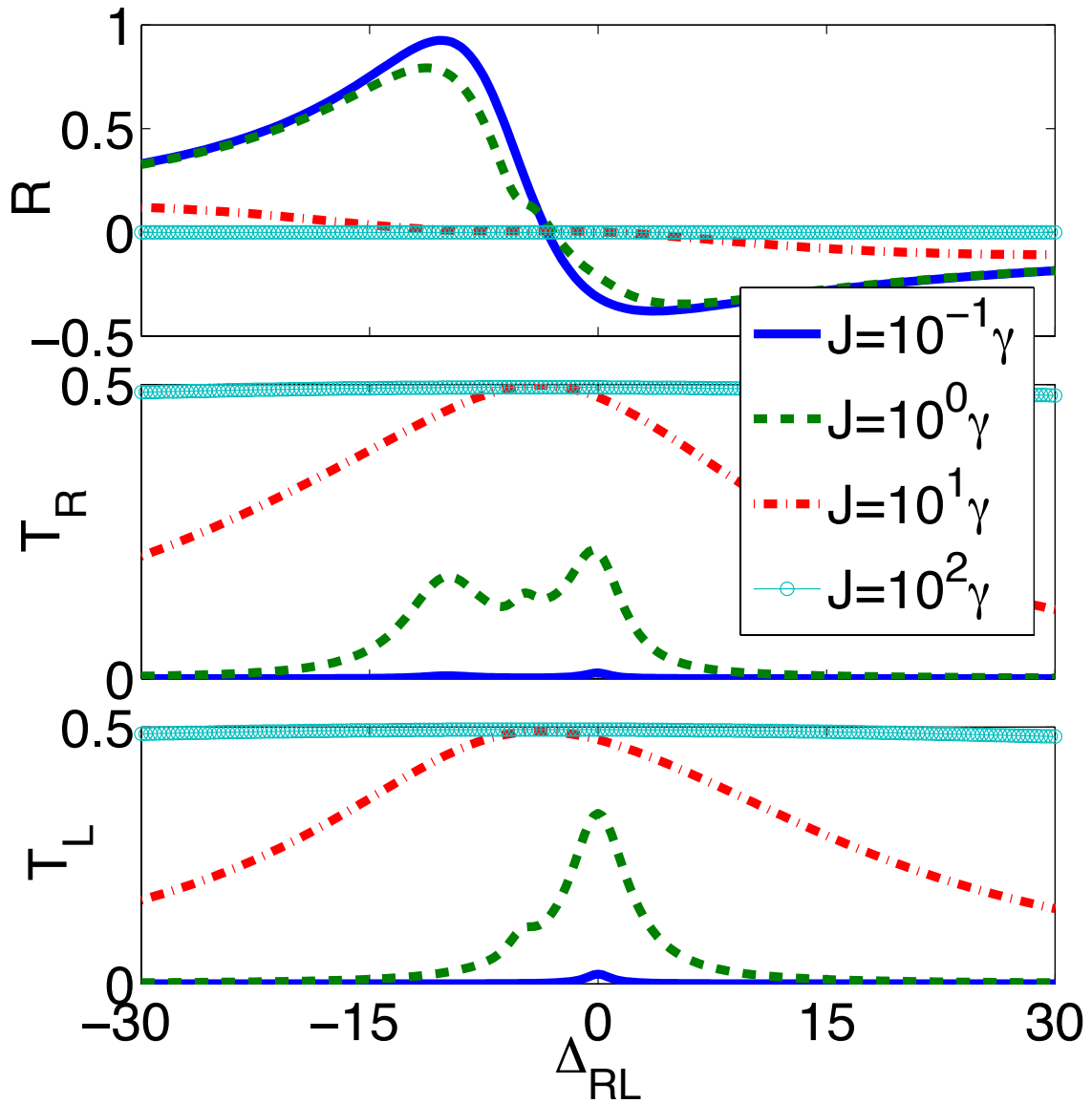
Figure 2.4: **Transport of Fock state** $|2\rangle$**.** A fast time-dependent pulse can be designed to prepare the Fock state, then the system is allowed to evolve and relax while the output currents are time-integrated, defining the rectification factor (top panel), the transport efficiency to the right (middle), and the transport efficiency to the left (bottom), with $U = 10\gamma$ and for different values of the tunnel coupling between resonators. As the coupling is increased the junction slowly switches from a rectifier to a splitter 50% chance splitter.

described by a single-mode Bose-Hubbard model with an effective nonlinearity $U \sim 1$ MHz [40]. With state-of-the art capabilities, the regime of quantum optical diode operation can be achieved in standard coplanar superconducting resonators with quality-factors on the order of $Q \simeq 10^5$, i.e. $\gamma \sim 100$ kHz at microwave frequencies (10 GHz) [40], which is enough to reach the condition $U/\gamma \sim 10$. Moreover, the superconducting microstrip platform naturally realizes the excitation scheme that we have been schematically considering: input/output channels can be defined as broad-band transmission lines of microwave photons directly pumping the n-l junction at left/right ends. Finally, detection of the second-order correlation signal at zero-time delay is now possible also in the microwave domain through quadrature detection schemes [41], which makes it possible for an experimental replication of our theoretical results.

Semiconducting optical circuits. On a parallel route, a quantum optical diode operation can be realized in integrated photonic circuits at optical or near-infrared wavelengths ($\lambda \sim 1$ μm). In this case, a preferred platform would be represented by photonic crystal circuits in thin semiconductor slabs [39]. Strong optical nonlinearities of the Kerr-type, which would be the route to effectively realizing the model, have been shown for polaritonic excitations in pillar micro cavities to be on the order of $U_{nl} \sim 9$ μeV$\cdot\mu$m^2 [42]. Diffraction-limited light confinement provided by photonic crystal cavities, i.e. an effective mode area of $(\lambda/n)^2$, would allow to achieve single-photon nonlinearities in the range $U \sim 10 - 100$ μeV. Considering optical/near-infrared operation, i.e. in the eV range, a quality factor on the order of $10^5 - 10^6$ would be sufficient to reach the quantum optical diode operation $U/\gamma \sim 10$. We notice that such values have been already demonstrated in typical semiconductor photonic crystal chips [43], although no conclusive signature of single-photon nonlinear behaviour has been reported to date for polaritons confined in photonic crystal cavities. On the other hand, such photonic crystal platforms naturally allow to engineer waveguide-coupled cavity schemes, which are straightforwardly described by the theoretical modeling analysed in the present work. It should also be noted that efficient measurement of second-order correlation signals at zero-time delay is achieved through fast single-photon counting at near-infrared wavelengths, where the main limiting factor might be related to the photon lifetime in the resonators, $\tau \sim 1/\gamma$. For $Q > 10^5$ such lifetime is certainly above the typical resolution timescale of photodetectors (in the pico-second range [44]), thereby allowing to identify the single- or two-photon rectification regimes in HBT measurements.

2.4 Summary

We have addressed non-reciprocal propagation of energy pumped into a generic system of tunnel-coupled nonlinear-linear resonators. The model considered has been shown to describe several physical systems. In particular, we have carefully verified that our results could be observed in state-of-the art experiments, and we pointed out two main architectures in which this goal could be pursued. From a theoretical point of view, we have addressed the quantum nonlinear regime of the proposed device, and we have shown it can work as a rectified quantum source. The ultimate goal in this research field would be to achieve complete control over quantum optical transport, which includes perfect quantum state transfer and rectification. Taking initial steps in this direction, we have also shown how quantum states at the input may be rectified through the junction, which opens up the possibility to work towards fully quantum state rectification, a goal that has never been achieved so far. Finally, we have shown that the junction also works as a photonic splitter, which shows the versatility of this elementary system as a valve for quantum optical transport. In this respect, a fascinating venue for future research would be the rectification of many-body

or mesoscopic quantum states, which would allow for the controlled transport of large amounts of quantum data encoded in complex quantum systems. In fact, we believe this novel quantum device might become a key element in prospective quantum photonic circuits, where unwanted feedback caused by reflections between different system components might have a deleterious effects on the quantum operations to be performed in complex optical networks.

Bibliography

[1] H. A. Haus, *Waves and Fields in Optoelectronics* (Prentice-Hall, Englewood Cliffs, NJ, 1984).

[2] M. Terraneo, M. Peyrard, and G. Casati, Phys. Rev. Lett. **88**, 094302 (2002).

[3] C.W. Chang, D. Okawa, A. Majumdar, and A. Zettl, Science **314**, 1121 (2006).

[4] R. Scheibner, M. König, D. Reuter, A. D. Wieck, C. Gould, H. Buhmann, and L. W. Molenkamp, New J. Phys. **10**, 083016 (2008).

[5] B. Liang, B. Yuan, and J. C. Cheng, Phys. Rev. Lett. 103, 104301 (2009).

[6] B. Liang, X.-S. Guo, J. Tu, D. Zhang, and J. C. Cheng, Nat. Materials **9**, 989 (2010).

[7] K. Gallo, G. Assanto, K. Parameswaran, and M. Fejer, Appl. Phys. Lett. **79**, 314 (2001).

[8] Z. Yu and S. Fan, Nat. Photonics **3**, 91 (2009).

[9] L. Bi, J. Hu, P. Jiang, D. H. Kim, G. F. Dionne, L. C. Kimerling, and C. A. Ross, Nat. Photonics **5**, 758 (2011).

[10] L. Fan, J. Wang, L.T. Varghese, H. Shen, B. Niu, Y. Xuan, A.M. Weiner, and M. Qi, Science **335**, 447 (2012).

[11] H. Lira, Z. Yu, S. Fan, and M. Lipson, Phys. Rev. Lett. **109**, 033901 (2012).

[12] J.L. O'Brien, A. Furusawa, and J. Vučković, Nat. Photonics **3**, 687 (2009).

[13] D.E. Chang, A.S. Sorensen, E.A. Demler, and M.D. Lukin, Nat. Physics **3**, 807 (2007).

[14] D. Gerace, H.E. Türeci, A. Imamoğlu, V. Giovannetti, and R. Fazio, Nat. Physics **5**, 281 (2009).

[15] Y. Shen, M. Bradford, and J.-T. Shen, Phys. Rev. Lett. **107**, 173902 (2011).

[16] R. A. Pepino, J. Cooper, D. Z. Anderson, and M. J. Holland, Phys. Rev. Lett. **103**, 140405 (2009).

[17] S. Lepri and G. Casati, Phys. Rev. Lett. **106**, 164101 (2011).

[18] D. Jaksch, C. Bruder, I. J. Cirac, C. W. Gardiner, and P. Zoller, Phys. Rev. Lett. **81**, 3108 (1998).

[19] M. Greiner, O. M. Mandel, T. Esslinger, T. Hansch, and I. Bloch, Nature **415**, 39 (2002).

[20] M.J. Werner and A. Imamoglu. Phys. Rev. A **61**, 011801(R) (1999).

[21] M. J. Hartmann, F. G. S. L. Brandão, and M. B. Plenio, Nat. Physics **2**, 849 (2006).

[22] D. E. Chang, V. Gritsev, G. Morigi, V. Vuletic, M. D. Lukin, and E. A. Demler, Nat. Physics **4**, 884 (2008).

[23] D. G. Angelakis, M. F. Santos, and S. Bose, Phys. Rev. A **76**, 031805(R) (2007).

[24] M. Leib and M. J. Hartmann, New J. Phys. **12**, 093031 (2010).

[25] I. Carusotto, D. Gerace, H. E. Tureci, S. De Liberato, C. Ciuti, and A. Imamoglu, Phys. Rev. Lett. **103**, 033601 (2009).

[26] F. Nissen, S. Schmidt, M. Biondi, G. Blatter, H. E. Tureci, and J. Keeling, Phys. Rev. Lett. **108**, 233603 (2012).

[27] A. Verger, C. Ciuti, and I. Carusotto, Phys. Rev. B **73**, 193306 (2006).

[28] I. Carusotto, T. Volz, and A. Imamoğlu. Europhys. Lett. **90**, 37001 (2010).

[29] S. Ferretti and D. Gerace, Phys. Rev. B **85**, 033303 (2012).

[30] T.C.H. Liew and V. Savona, Phys. Rev. Lett. **104**, 183601 (2010).

[31] M. Bamba, A. Imamoğlu, I. Carusotto, and C. Ciuti, Phys. Rev. A **83**, 021802(R) (2011).

[32] S. Ferretti, V. Savona, and D. Gerace, New J. Phys. **15**, 025012 (2013).

[33] Sara Ferretti, Dario Gerace, Physical Review B 85, 033303 (2012).

[34] H. Wiseman and G. Milburn, *Quantum Measurement and Control* (Cambridge, 2010).

[35] C. Gardner, *Quantum Noise* (Springer, 2010).

[36] H. Carmichael, *An open systems approach to quantum optics* (Springer-Verlag, Berlin, 1993).

[37] R. Hanbury Brown & R.Q. Twiss. *Nature* **177**, 27 (1956).

[38] A.A. Houck, H.E. Tureci, and J. Koch, Nat. Physics **8**, 292 (2012).

[39] J. D. Joannopoulos, S. G. Johnson, J. N. Winn, and R. D. Meade, *Photonic Crystals: molding the flow of light* (Princeton University Press, Princeton, 2008).

[40] A.J. Hoffman, S.J. Srinivasan, S. Schmidt, L. Spietz, J. Aumentado, H.E. Tureci, & A.A. Houck. *Phys. Rev. Lett.* **107**, 053602 (2011).

[41] C. Lang, D. Bozyigit, C. Eichler, L. Steffen, J.M. Fink, A.A. Abdumalikov, M. Baur, S. Filipp, M.P. da Silva, A. Blais, & A. Wallraff. *Phys. Rev. Lett.* **106**, 243601 (2011).

[42] L. Ferrier, E. Wertz, R. Johne, D. D. Solnyshkov, P. Senellart, I. Sagnes, A. Lamaitre, G. Malpuech, & J. Bloch. *Phys. Rev. Lett.* **106**, 126401 (2011).

[43] Combrié, S., De Rossi, A., Tran, Q. V. & Benisty, H. *Opt. Letters* **33**, 1908-1910 (2008).

[44] J. Wiersig, C. Gies, F. Jahnke, M. Assmann, T. Berstermann, M. Bayer, C. Kistner, S. Reitzenstein, C. Schneider, S.Hofling, A. Forchel, C. Kruse, J. Kalden, & D. Hommel. *Nature* **460**, 245 (2009).

[45] A. Tomadin, V. Giovannetti, R. Fazio, D. Gerace, I. Carusotto, H.E. Tureci, A. Imamoglu, Phys. Rev. A 81, 061801(R) (2010); J. Werschnik and E.K.U. Gross, J. Phys. B 40, R175 (2007).

Chapter 3

A Fabry-Perot interferometer with quantum mirrors: nonlinear light transport and rectification

3.1 Introduction

There is a growing interest in the realization of quantum optical systems in which single emitters are strongly coupled to one-dimensional (1D) radiation modes for efficient light transport [1, 2, 3] and quantum information processing [4]. The ultimate goal would be to progressively replace or hybridize current microelectronics with integrated optical devices in order to enhance data capacity, transmission velocity, and efficiency. One of the benchmarks for information processing is the ability to control the directionality of energy flux within a specific system architecture, a task that generically requires 1D propagation channels and nonlinear components. Furthermore, so-called rectifying devices provide the unidirectional isolation of strategical centres in electronic circuits. The combination of these properties has allowed for the technological revolution of microelectronic processors in the last century, and a similar development for the transport of light is necessary if one is to expect photon-based computing systems. In this letter, we show how two-level quantum systems may be employed as non-linear mirrors forming a Fabry-Perot interferometer. Optical rectification is a direct consequence of the nonlinear nature of such interferometer. If integrated within an optical circuit, this rectifying device would prevent unwanted signals (or noise) to travel back, thus preserving the processing capabilities at the source. This is of utmost importance in the quantum regime, e.g. to prevent decoherence at the sender of the signals.

Several experiments have already demonstrated the combination of strong nonlinear behavior and 1D light propagation in different system implementations, such as trapped ions coupled to focused light beams or optical fibers [5, 6], superconducting circuits coupled to microwave transmission lines [7, 8, 9], and semiconductor quantum dots or vacancy (e.g., N-V) centers coupled to photonic or plasmonic waveguides [12, 10, 11, 13]. Among these attempts, the use of solid state quantum emitters as artificial two-level systems (TLS) is specially promising due to their nanoscale dimensions, their extreme nonlinear properties, and their tunability, thanks to the use of external electrostatic gates [14], applied magnetic fields [15, 16], or mechanical strain [10]. These combined

advantages have led to a wide range of theoretical proposals and recent experiments, with the aim of building single photon emitters [17], single-photon light switches and transistors [2], quantum optical diodes [18, 19, 20] and interferometers [21]. Following these proposals, a pair of TLS coupled to a 1D waveguide can be expected as one of the simplest configurations where tunable non-linear and non-reciprocal optical phenomena at the quantum level could be practically realized, besides allowing for photonic mediated interactions between distant qubits [22, 23, 24].

In this work we employ a semi-classical analysis to theoretically treat the transport of light in a *Quantum Fabry-Perot* (QFP) interferometer built from two TLS embedded in a 1D photonic channel, drawing inspiration from the recently demonstrated analogy between a single TLS and an optical mirror [5]. After validating our theoretical approach through comparison with previous results based on a similar model for the case of two identical TLS [1, 9, 24], we thoroughly study the case of two different TLS. In this latter case, we show that the QFP interferometer manifests non-reciprocal effects, not captured in previous works, that enable to rectify light transport through the 1D channel. Remarkably, we find regions where both light rectification and transmission exceed 92%, depending on the system parameters. In our approach, the TLS are treated as quantum systems, and rectification emerges out of their highly nonlinear behavior, while the light field is treated as a classical input. Given the generality of this method in describing light transport within this QFP interferometer, our results can be adapted to a number of different physical implementations, as discussed at the end of the letter. Differently from previous proposals [19, 25, 26, 27], our QFP interferometer does not require the application of external fields to produce non-linear effects on light transport.

3.2 Fabry-Perot model:

We consider two TLS embedded in a 1D waveguide, as shown in Fig. 3.1. Light with angular frequency ω and power p_{inc} is injected into the waveguide. We shall use the terms "intensity" and "power" interchangeably throughout the manuscript. For these, we will use the symbol p, which is a dimensionless quantity representing the number of photons per lifetime. We denote with TLS1 (TLS2) the first (second) quantum emitter lying on the light path, if light is shined from left-to-right as in Fig. 3.1. The TLS1 (TLS2) has transition frequency $\omega_{1(2)}$, decay rate $\gamma_{1(2)}$, position $z = 0$ ($z = L$). The detuning of the incoming light with respect to the TLS1 (TLS2) transition frequency is $\delta\omega_1 = \omega - \omega_1$ ($\delta\omega_2 = \omega - \omega_2$). Within a semi-classical approach, we treat such a system in analogy to a Fabry-Perot interferometer (see Fig. 3.1), where the reflectances of the mirrors are given by the reflectances of the TLS, as obtained in a quantum mechanical framework. These latter can be readily derived from Ref. [28] (see [29]):

$$R_{1(2)} = \frac{\gamma_{1(2)}^2}{\gamma_{1(2)}^2 + 4\delta\omega_{1(2)}^2 + 4p_{1(2)}\gamma_{1(2)}^2} \ , \tag{3.1}$$

where $p_{1(2)}$ is the power impinging onto the TLS1 (TLS2), i.e. $\gamma_{1(2)}p_{1(2)}$ is the number of photons per second impinging onto TLS1 (TLS2). The quantity $R_{1(2)}$ represents the fraction of light power that TLS1 (TLS2) reflects back into the 1D channel. Furthermore, $\theta_{1(2)} = \arctan\left[2\delta\omega_{1(2)}/\gamma_{1(2)}\right]$ is the phase-shift given by the TLS1 (TLS2) to the light upon each reflection [24]. The phase-shift given by either TLS to the transmitted light is neglected, as usual for mirrors.
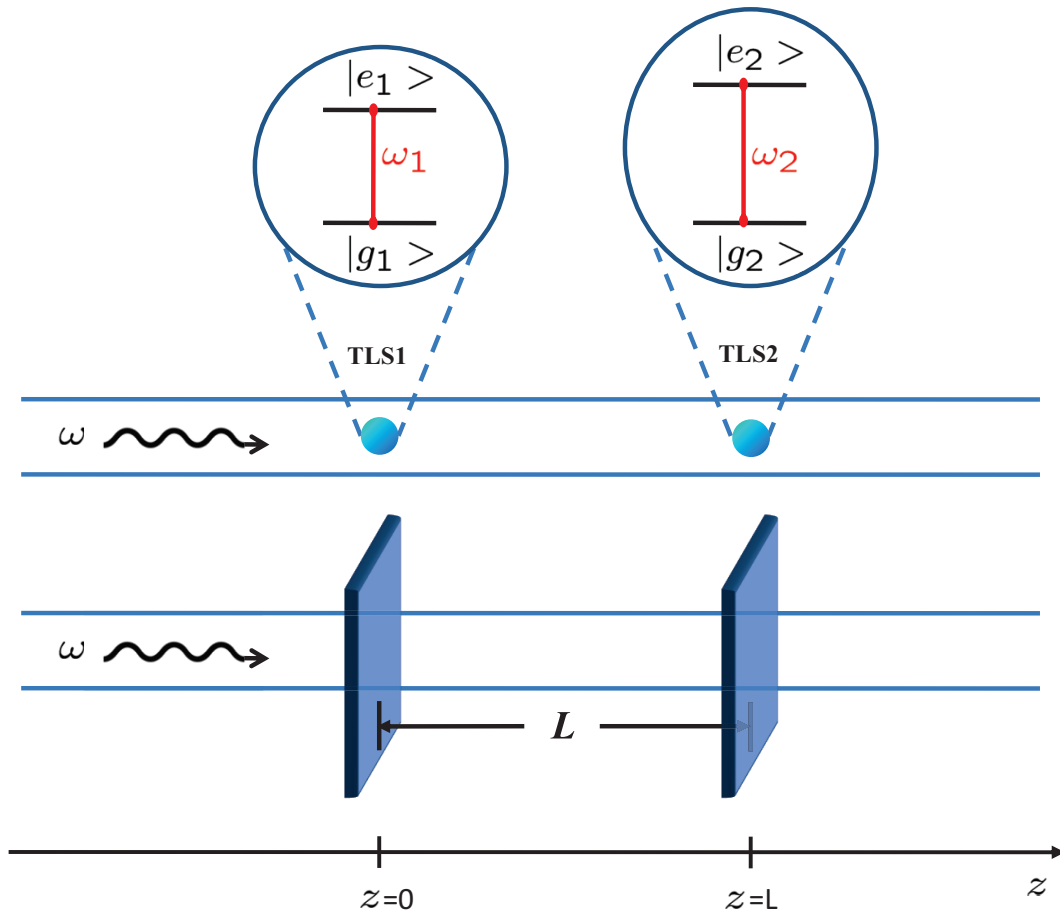
Figure 3.1: (Color online). A pair of two-level quantum systems in a one-dimensional waveguide as a quantum Fabry-Perot interferometer, and its classical counterpart.

The fraction of light power that the FP interferometer transmits, i.e. the FP transmittance, can be calculated as [29]

$$T = \frac{1}{F_1 + F_2 \sin^2(2\mu + \theta_+)} \ ,$$ (3.2)

where

$$F_1 = \frac{(1 - \sqrt{R_1 R_2})^2}{(1 - R_1)(1 - R_2)} \ , \ F_2 = \frac{4\sqrt{R_1 R_2}}{(1 - R_1)(1 - R_2)} \ ,$$ (3.3)

while $\mu = n\omega L/(2c)$, n is the effective refractive index of the waveguide, c is the speed of light in vacuum and $\theta_+ = (\theta_1 + \theta_2)/2$. In order to use Eq. (3.2), we need first to find what the values for R_1 and R_2 are. This reduces to the question of finding what the values for p_1 and p_2 are. These latter can be obtained by numerically solving a system of coupled equations. The details of such a calculation are given in the supplemental material [29]. Thus, by using Eqs. (3.2) and (3.1), together with the numerical values for $p_{1,2}$, the transmittance T can be numerically calculated for any set of the (externally adjustable) variables $\gamma_{1,2}$, $\delta\omega_{1,2}$, L, p_{inc}.

3.3 Non-linear light transport

The semiclassical approach employed in this work has been fully validated by comparing our results to solutions based on quantum mechanical models taken from the literature [24, 1, 9] (see [29]). In particular, we stress that the present approach allows to calculate the light transport for any incident light power, as well as for different atomic frequencies and decay rates, in contrast to [1, 24].

First, we explore the light intensity between the TLS (intracavity intensity) and at the TLS positions, respectively. For simplicity, in the following we will consider $\gamma_1 = \gamma_2 = 1 \equiv \gamma$ and L in units of the photon wavelength, $\lambda = 2\pi c/(n\omega)$. In a standard FP interferometer, large intracavity intensity is present when the mirror reflectances are close to 1. In line with our analogy, high intracavity intensity is expected in the present model when the TLS reflectances $R_{1,2}$ are nearly 1, which is the case when light is shined in resonance with the TLS and at low incident power. Let us denote by $p_{intr}(z)$ the intracavity intensity at the position z, where $0 < z < L$, and by $\langle p_{intr}(z) \rangle$ the average intracavity intensity: $\langle p_{intr}(z) \rangle = \int_0^L p_{intr}(z)\mathrm{d}z/L$. In Figs. 3.2(a) and (b), these two quantities are plotted as a function of p_{inc} and z, respectively. From panel (a) we notice that the relation between $\langle p_{intr}(z) \rangle$ and p_{inc} is *non-linear*. In fact, by supposing low incident power and $\delta\omega_1 = \delta\omega_2 = 0$, it can be analytically shown that the average intracavity intensity is well approximated by $\langle p_{intr}(z) \rangle \approx \sqrt{p_{inc}}$. In Fig. 3.2(a), such approximate expression and the exact numerical values for $\langle p_{intr}(z) \rangle$ are directly compared. The relation $\langle p_{intr}(z) \rangle \approx \sqrt{p_{inc}}$ indeed yields $\langle p_{intr}(z) \rangle \gg p_{inc}$, as we expected from the discussion above. Furthermore, this non-linear relation marks a stark difference with respect to the standard Fabry-Perot interferometer, where a linear relation between incident and intracavity intensities holds [31].

In our model, only for large p_{inc} the average intracavity intensity can be well approximated by a linear function of p_{inc} (see panel (a), inset). Specifically, for large p_{inc} the average intracavity intensity asymptotically satisfies the relation $\langle p_{intr}(z) \rangle \approx p_{inc}$, as expected.

Finally, for low incident power ($p_{inc} \lesssim 1$), light between the atoms forms a standing wave where nodes are present (see panel (b), where nodes are at positions $z = 1/4$ and $3/4$).

It is instructive to show the light intensities at the sites of the TLS as the distance L varies, while p_{inc} is kept constant. In Figs. 3.2(c) and (d), we plot p_1 and p_2 for incident power $p_{inc} = 0.1$
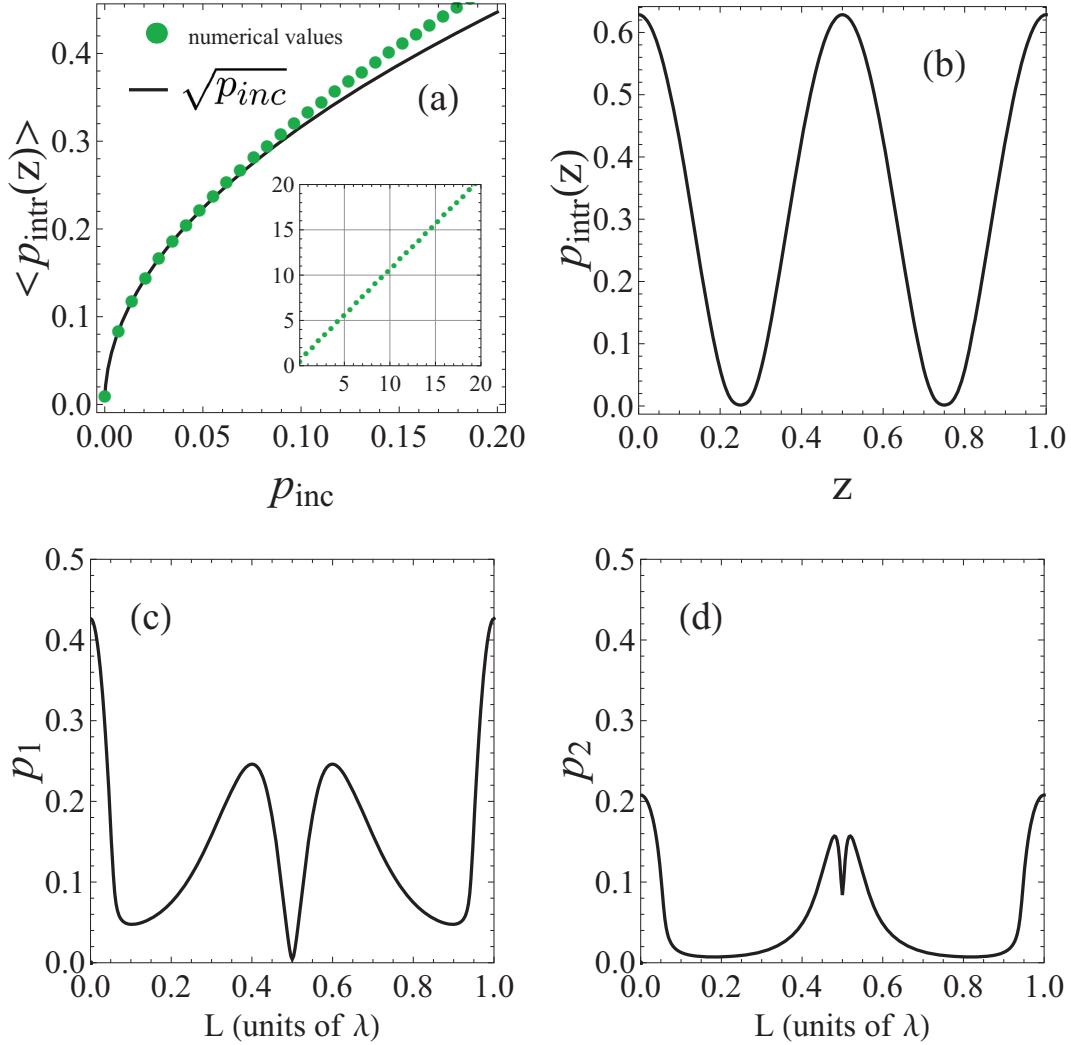
Figure 3.2: (color online). (a) Average intracavity intensity. The inset shows the same quantity for larger values of the abscissa; (b) Intracavity intensity; (c) Intensity impinging onto TLS1; (d) Intensity impinging onto TLS2. p_{inc} is the incident power, while L is the TLS distance in units of photon wavelength. $\delta\omega_1 = \delta\omega_2 = 0$ in all panels. $L = 1$ in (a) and (b). $p_{inc} = 0.1$ in (b), (c) and (d).

and $\delta\omega_1 = \delta\omega_2 = 0$. We notice that at $L = 0.5$ the light intensity at the TLS1 position is identically 0 and, consequently, the light intensity at the TLS2 position equals the incident intensity. This remains true up to about $p_{inc} \lesssim 1$, and it is caused by the fact that the back reflected light from the TLS2 turns out to be π shifted with respect to the incident light, at the site of the TLS1 (see [29] for more details).

3.4 Rectification

The joint implementation of TLS and 1D waveguides is believed to represent the future building-blocks of nanoscale optoelectronics [32, 33]. The realization of nanoscale devices that allow uni-directional light transmission is of utmost importance in this field, and is thus subject of current research [34, 35]. However, most of the attempts to realize or propose optical diodes able to work at the quantum regime lack real miniaturization possibilities and control at the nanoscale [19, 25, 26, 27, 20, 36, 37, 18]. Here we show that two TLS embedded in a 1D waveguide provide the requested features for building a microscopic and integrable optical diode. The realization of this quantum optical diode is feasible with the state-of-the-art technology, as discussed in the following section.

We define the rectifying factor for an optical diode as [20, 38]

$$\mathcal{R} = \frac{|T_{12} - T_{21}|}{T_{12} + T_{21}} \ , \tag{3.4}$$

where T_{12} is the transmittance for the case light is shined from left-to-right (as in Fig. 3.1), while T_{21} is the transmittance in the optical inverse situation where light is shined from right-to-left. We shall take $\mathcal{R}$ and $\mathcal{L} = T_{12}\mathcal{R}$ as figures of merit to quantify the non-reciprocal effects that our microscopic FP manifests. In Fig. 3.3, the quantities $\mathcal{R}$ and $\mathcal{L}$ are shown as functions of L and $\delta\omega_1$, while $\delta\omega_2 \approx 0$. In panels (a) and (b), we investigate the case $p_{inc} = 0.001$, which may be considered equivalent to the single-photon regime (see Fig. S2 of [29]). High levels of light rectification and transmission are evident. Specifically, some areas in the color scale plot are characterized by both $\mathcal{R}$ and $\mathcal{L}$ greater than 0.92. By increasing the incident power, these areas broaden, while $\mathcal{R}$ and $\mathcal{L}$ decrease (see panels (c) and (d) where the same quantities are plotted for $p_{inc} = 0.1$). In (c) and (d), the highest values for $\mathcal{R}$ and $\mathcal{L}$ are ≈ 0.53 and 0.52, respectively.

High values for $\mathcal{R}$ and $\mathcal{L}$ in Figs. 3.3(a) and (b), could be understood as follows. Light is in resonance with TLS2 and at low power, while it is in general not in resonance with TLS1, unless we are in the central region of the plots where $\delta\omega_1 = 0$. Under such conditions, we have $R_1 < 1$ and $R_2 \approx 1$. When light is incident from right-to-left, it encounters TLS2 first, which implies full reflection (being $R_2 \approx 1$). On the other hand, when light is incident from left-to-right, it encounters TLS1 first, hence a significant amount of that light is coherently transmitted to TLS2 (since $R_1 < 1$). Then, TLS2 totally reflects such radiation back into the 1D channel to TLS1. Such light acquires a phase-shift that depends on L, due to the path length. At this point, TLS1 must deal with both the phase-shifted light coming back from TLS2 and the incident light that is forwardly directed. Both are partially reflected and partially transmitted. However, since light is not in resonance with TLS1, the light reflected from TLS1 acquires a phase-shift θ_1 that depends on $\delta\omega_1$ (see after Eq. (3.1)). The two phase-shifts, the one depending on L and the one depending on $\delta\omega_1$, can give constructive or destructive interference. For some values of L and $\delta\omega_1$, we get destructive interference for light exiting the FP from the left, while constructive interference for
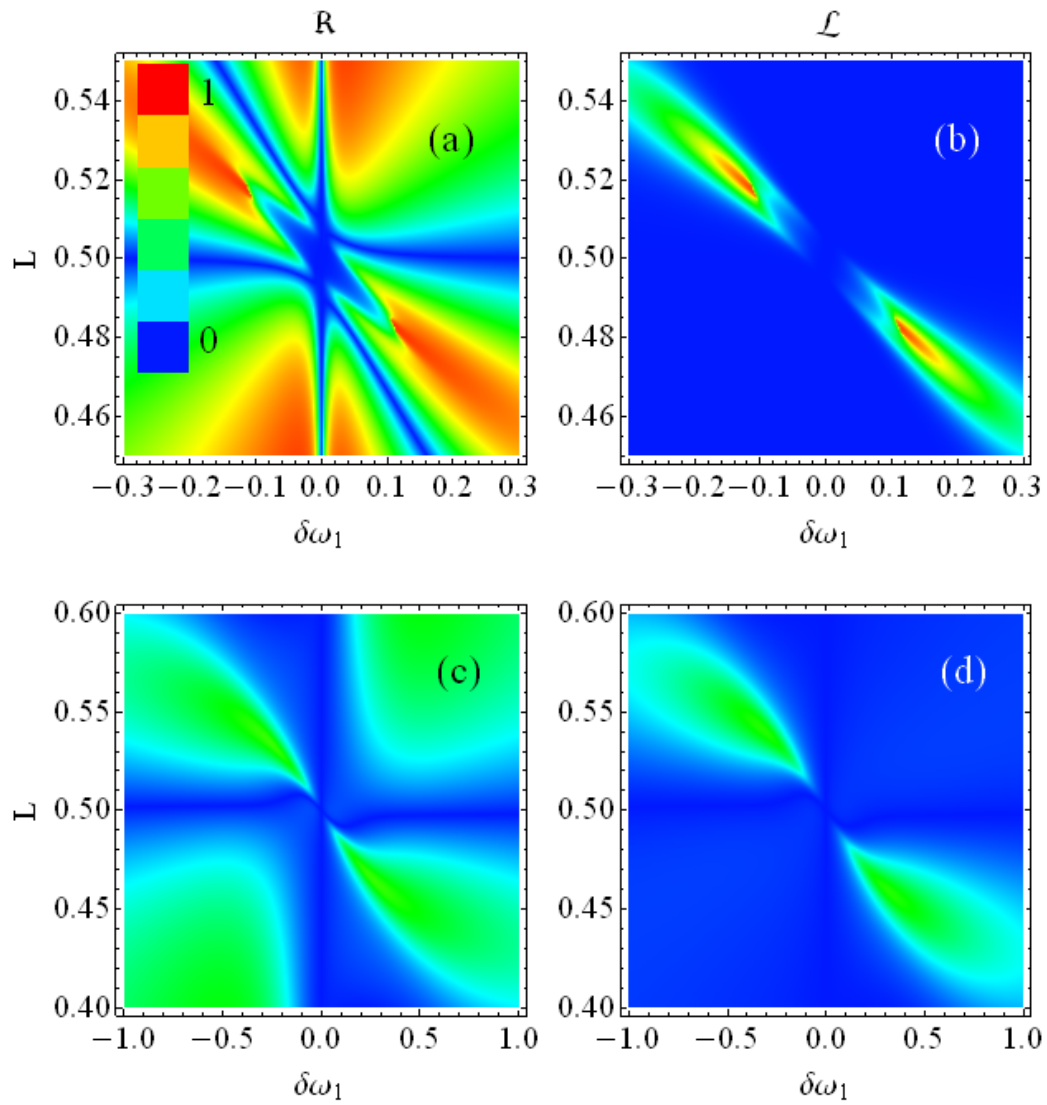
Figure 3.3: (color online). Light rectification. Parameters $\mathcal{R}$ and $\mathcal{L}$ are plotted. $\delta\omega_2 = 0$ in all panels. $p_{inc} = 0.001$ in (a) and (b). $p_{inc} = 0.1$ in (c) and (d).

light directed toward TLS2. Those values provide high level of rectification showed in Fig. 3.3(a). In Figs. 3.3(c) and (d), both R_1 and R_2 are considerably lower than 1, since here the incident light power is not very low. By re-applying the foregoing discussion, we expect and find lower degree of light rectification.

We finally point out that the results shown in Fig. 3.3 do not change significantly within the interval $-0.01 \lesssim \delta\omega_2 \lesssim 0.01$. For configurations where none of the two TLS is in resonance with the incident light beam, there is no region where both $\mathcal{R}$ and $\mathcal{L}$ simultaneously display large values.

3.5 Physical implementation:

The QFP interferometer introduced in this work can be implemented in a number of different technologies and material platforms. In particular, we outline three main architectures as promising candidates to observe such non-reciprocal behavior.

First, superconducting circuits have emerged in the last few years as an outstanding platform to realize quantum optical functionalities in the microwave range. In this respect, the QFP interferometer can be realized with the state-of-art technology. Considering recent experiments [8], we notice that the system parameters for attaining maximal light rectification and transmission are well within reach. Although it does not represent a miniaturized version of our proposed device, such microwave circuit implementation of the QFP interferometer is likely to be the most promising candidate for a first proof-of-principle demonstration of the rectifying features, also thanks to the high level of electrostatic control on state of the single superconducting qubits as TLS.

As a second alternative, we notice that remarkable progress has been lately achieved in coupling semiconductor quantum dots to 1D photonic wires [12, 17] or to semiconducting micro-pillars [40]. Such artificial atoms behave as almost ideal TLS, and growing stacks of two or more QDs along the same axis and at distances on the order of the optical emission wavelength ($\sim 1~\mu$m) is at the level of current technology [39]. Moreover, such a nanophotonic platform would naturally represent an fully integrated quantum optical version of our proposed device.

Finally, NV (Nitrogen vacancy) centers in diamond coupled to 1D surface plasmons [13] can be an interesting possibility to implement a QFP model. In this case, large values of the light-matter coupling rate could be achieved, owing to the strong confinement of plasmonic modes close to the metallic nanowire surface. This could allow to easily achieve the requested parameters range for light rectification along the 1D axis, i.e. large phase shifts produced by each TLS on incoming light.

The material and engineering efficiency in preparing the 1D system is standardly quantified by an efficiency parameter β ranging from 0 (minimal efficiency) to 1 (maximal efficiency). β quantifies the strength of the TLS-light coupling in the 1D material. Remarkably high values of β have been attained in recent experiments: in superconducting circuits $\beta \approx 0.99$ [8], while in semiconductor quantum dots coupled to photonic wires [41] or to photonic crystals [42] $\beta \approx 0.95, 0.89$, respectively.

3.6 Summary and conclusions

We modeled a pair of two-level quantum systems embedded in a one-dimensional waveguide as a Fabry-Perot quantum interferometer, where the two quantum systems play the role of highly saturable and nonlinear mirrors. Beside manifesting non-linear effects, this quantum interferometer can work as a very efficient integrated optical diode, with unprecedented figures of merit in terms of simultaneous light rectification and transmission, and thus with potential applications in integrated

optical photonics. Such a quantum optical diode can be implemented with several integrated one-dimensional designs employing different state-of-the-art technologies and materials, and dimensions ranging from nanometer to millimeter sizes. Unconditional quantum rectification (i.e., rectification of quantum states) is the ultimate goal of this research field, and has not yet been realized. We here suggest that the present system could be investigated in the fully quantum regime (considering quantum states for the input light field) as a strong candidate to photonic rectification.

Supplemental material:

Derivation of the reflectance of a TLS:

We take Eq. (1) of Ref. [28] and we adapt it to our case-study. To do this, we set dephasing (γ^*) and incoherent pump (ξ) equal to zero, while efficiency coefficient (β) equal to unity. We moreover relabel $\delta_L \to \delta\omega$, in order to match the notation used in the Letter. We solve in the steady-state regime, i.e. for $\mathrm{d}\langle\sigma_-\rangle/\mathrm{d}t = \mathrm{d}\langle\sigma_z\rangle/\mathrm{d}t = 0$. The solutions are

$$
\begin{aligned}
\Re\langle\sigma_-\rangle &= -\frac{\gamma\Omega}{\gamma^2+4\delta\omega^2+2\Omega^2} \quad , \quad \Im\langle\sigma_-\rangle = \frac{2\delta\omega}{\gamma}\Re\langle\sigma_-\rangle \ , \\
\langle\sigma_z\rangle &= -\frac{1}{2} + \frac{\Omega^2}{\gamma^2+4\delta\omega^2+2\Omega^2} \ ,
\end{aligned}
\tag{S.1}
$$

where $\Omega = \gamma\sqrt{2p}$, $\Re$ and $\Im$ are real and imaginary parts, respectively. By plugging this result in Eq. (4) of Ref. [28], we get $\mathcal{R} = \frac{\gamma^3 p}{\gamma^2+4\delta\omega^2+4\gamma^2 p}$. Finally, we normalize by the number of photons per second impinging onto the TLS, i.e. $p\gamma$. By doing so, we obtain the reflectance showed in Eq. (1) of the Letter: $R = \frac{\gamma^2}{\gamma^2+4\delta\omega^2+4p\gamma^2}$. A similar calculation is plainly carried out in Ref. [30], where the reflectance is derived and displayed in Eq. (1.51). Using elementary algebra, this latter can be shown to coincide with the reflectance here derived.

Equations for the Fabry-Perot model:

Here we provide explicit derivations of the equations of the Fabry-Perot (FP) model used in the Letter. Let us consider Fig. 1 of the Letter. Let us furthermore denote by $t_{k>0}^{out}(z)$ the fully transmitted amplitude for the whole FP interferometer at the point $z \geq L$. Such a quantity can be calculated by coherently summing the amplitudes of the events that lead to transmission (see [31]), as sketched in Fig. S.3.4. If we take the phase of the field to be 0 at the point $z = L$, we get

$$
\begin{aligned}
t_{k>0}^{out}(z) &= \sqrt{p_{inc}}e^{ik(z-L)}\Big(\sqrt{T_1}\sqrt{T_2} \\
&\quad + \sqrt{T_1}\sqrt{R_2}\sqrt{R_1}\sqrt{T_2}e^{2ikL}e^{i(\theta_1+\theta_2)} \\
&\quad + \sqrt{T_1}\big(\sqrt{R_2}\big)^2\big(\sqrt{R_1}\big)^2\sqrt{T_2}e^{4ikL}e^{2i(\theta_1+\theta_2)} + ...\Big) \\
&= \frac{\sqrt{p_{inc}}e^{ik(z-L)}\sqrt{T_1 T_2}}{1-\sqrt{R_1 R_2}e^{2ikL}e^{i(\theta_1+\theta_2)}} \ ,
\end{aligned}
\tag{S.2}
$$

where $T_{1(2)} = 1 - R_{1(2)}$ is the transmittance of the TLS1 (TLS2) and $k = n\omega/c$. On the other hand, the incident amplitude at the point $z \leq 0$, $t_{k>0}^{inc}(z)$, can be written as

$$
t_{k>0}^{inc}(z) = \sqrt{p_{inc}}\ e^{ik(z-L)} \ .
\tag{S.3}
$$

In Eqs. (S.2) and (S.3), the subscripts $k > 0$ and $k < 0$ indicate that light is directed forwardly and backward, respectively. The fraction of light power that the FP interferometer transmits, i.e.

Fig. S.3.4: (color online). Sum of the amplitudes of events that lead to transmission.

the FP transmittance, can be calculated as

$$T = \frac{|t_{k>0}^{out}(L)|^2}{|t_{k>0}^{inc}(0)|^2} = \frac{1}{F_1 + F_2 \sin^2(2\mu + \theta_+)} \ , \tag{S.4}$$

where

$$F_1 = \frac{(1 - \sqrt{R_1 R_2})^2}{(1 - R_1)(1 - R_2)} \ , \ F_2 = \frac{4\sqrt{R_1 R_2}}{(1 - R_1)(1 - R_2)}, \tag{3.5}$$

while μ and θ_+ are defined in the Letter.

In order to use Eq. (S.4), we need first to find what the values for R_1 and R_2 are. This reduces to the question of finding what the values for p_1 and p_2 are. Similarly to what we have done in Eq. (S.2), we can calculate the intracavity amplitude for forward ($t_{k>0}^{intr}$) and backward ($t_{k<0}^{intr}$) directions, at the point z ($0 \leq z \leq L$):

$$t_{k>0}^{intr}(z) = \sqrt{p_{inc}} e^{ik(z-L)} \left(\sqrt{T_1} + \sqrt{T_1 R_1 R_2} e^{2ikL} e^{2i\theta_+} \right.$$

$$\left. + \sqrt{T_1} \left(\sqrt{R_2 R_1} \right)^2 e^{4i(kL+\theta_+)} + ... \right)$$

$$= \frac{\sqrt{p_{inc}} \sqrt{T_1}}{1 - \sqrt{R_1 R_2} e^{2i(kL+\theta_+)}} e^{ik(z-L)} \ ,$$

$$t_{k<0}^{intr}(z) = \sqrt{p_{inc}}e^{-ik(z-L)}\Big(0 + \sqrt{T_1 R_2}e^{i(kL+\theta_2)}$$

$$+ R_2\sqrt{T_1 R_1}e^{i(3kL+2\theta_+ +\theta_2)} + ...\Big)$$

$$= \frac{\sqrt{p_{inc}}\sqrt{T_1 R_2}}{1 - \sqrt{R_1 R_2}e^{2i(kL+\theta_+)}}e^{i(kL+\theta_2)}e^{-ik(z-L)} \ . \tag{S.5}$$

Making use of Eqs. (S.2), (S.3) and (S.5), the light power at the sites of the TLSs, $p_{1,2}$, are obtained by numerically solving the coupled equations

$$\begin{cases} p_1 &= \left| t_{k>0}^{inc}(0) + t_{k<0}^{intr}(0) \right|^2 , \\[2ex] p_2 &= \left| t_{k>0}^{intr}(L) \right|^2 . \end{cases} \tag{S.6}$$

The light powers $p_{1,2}$ appear both at the right- and the left-hand sides of Eqs. (S.6) in a non-trivial manner. This endows the FP interferometer with an intrinsic non-linear behaviour. These non-linear phenomena are investigated in the Letter. Equations (S.6) depend on all variables that can be externally set in the FP interferometer, viz. $\gamma_{1,2}$, $\delta\omega_{1,2}$, L, p_{inc}. By using Eqs. (S.6), (S.4) and Eq. 3.1 of the Letter, the transmittance T can be numerically calculated for any set of those variables.

π-*shifted intracavity field at the site of TLS1:*
Here we give details on the fact that the intracavity field turns out to be π-shifted with respect to the incident field, at the site of the TLS1, for the settings chosen in Fig. 2 of the Letter. To this regard, we recall that for $L = 0.5$ we have $kL = \pi$. Then, from (S.3), the phase of the incident field at $z = 0$ is $-ikL = -i\pi$. On the other hand, from Eq. (S.5) the phase of any addend at $z = 0$ is $i(2\pi)n$, where $n = 0, 1, 2....$ Thus, the light back reflected from the TLS2 is π shifted with respect to the incident light, at the site of the TLS1. This causes zero light intensity at the site of the TLS1, for low light power, as shown in Fig. 3 of the Letter. We may also observe that, when the incident power increases above ~ 1, the π-shifted back reflected light from the TLS2 will not be enough to cancel out the incident light. Therefore the intensity p_1 starts growing when p_{inc} approaches 1.

Validation of the semiclassical solution:
We start by analyzing the portion of transmitted light in the case of low incident power and equal TLSs, to directly compare with Refs. [1, 24, 9], where this case is considered within quantum mechanical models. We denote $\delta\omega \equiv \delta\omega_1 = \delta\omega_2$. In [1, 24], the time-independent Schrödinger equation for the single photon state is solved. For the case of two equal TLSs, [1, 24] obtain the transmittance showed in Fig. S.3.5(a). On the other hand, results provided by our semi-classical FP model, for the same system, are shown in Fig. S.3.5(b). In this latter, we have chosen very low incident power ($p_{inc} = 0.001$), in order to best reproduce the single-photon regime in [24, 1] by using classical incoming light. We readily see that our semi-classical FP approach in low input regime perfectly reproduces the light transport found in the literature in the single photon regime.
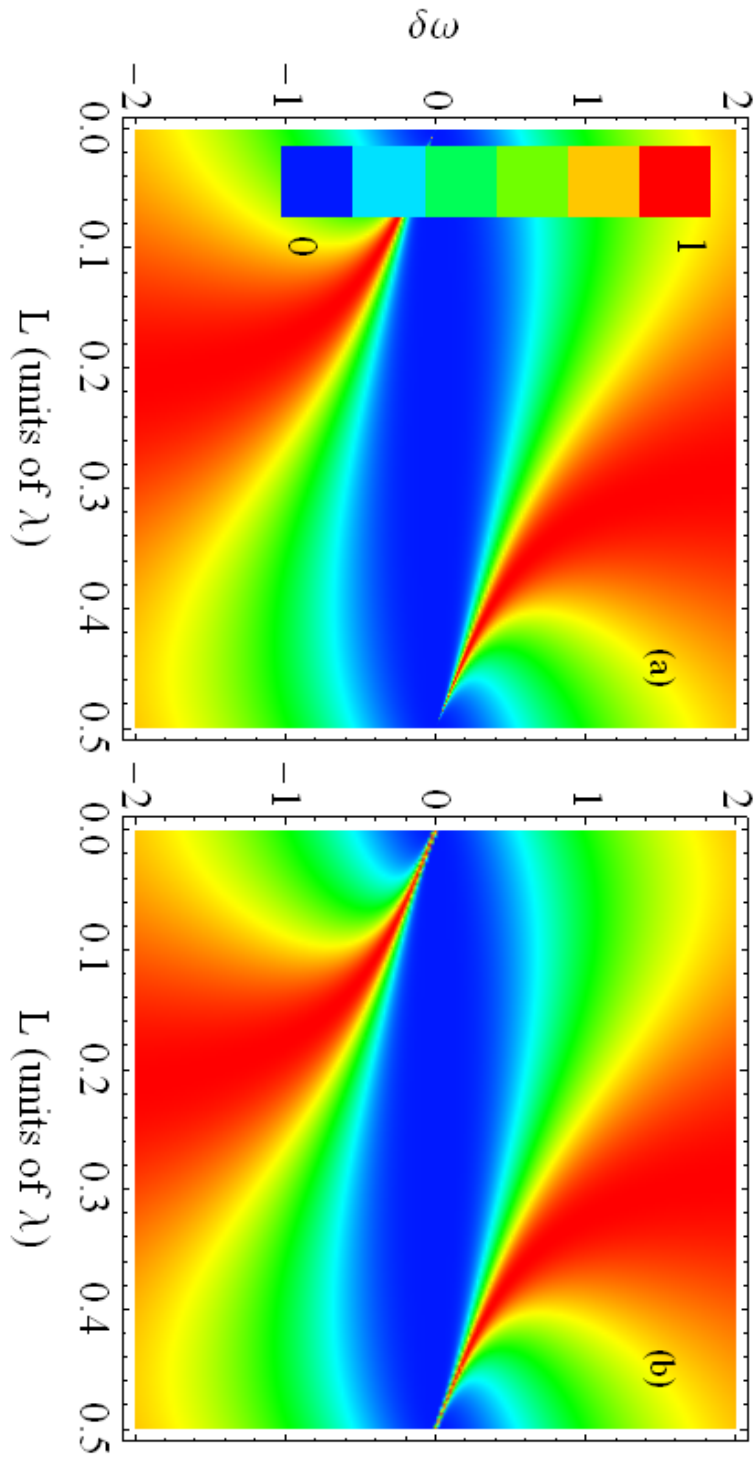
Fig. S.3.5: (color online). Transmittance for two equal TLSs. a) Quantum mechanical calculation with a single-photon state, as in [24] and [1]; b) Calculation from our semi-classical Fabry-Perot model with $p_{inc} = 0.001$. The two calculations give consistent results.

Bibliography

[1] J. T. Shen and S. Fan, Opt. Letters **30**, 2001 (2005); Phys. Rev. Lett. **98**, 153003 (2007).

[2] D. E. Chang, A. S. Sorensen, E. A. Demler, and M. D. Lukin, Nat. Physics **3**, 807 (2007).

[3] J. T. Shen and S. Fan, Phys. Rev. Lett. **98**, 153003 (2007).

[4] D. Valente, Y. Li, J. P. Poizat, J. M. Gérard, L. C. Kwek, M. F. Santos, and A. Auffèves, Phys. Rev. A **86**, 022333 (2013).

[5] G. Hétet, L. Slodička, M. Hennrich, and R. Blatt, Phys. Rev. Lett. **107**, 133002 (2011).

[6] C. Monroe and J. Kim, Science **339**, 1164 (2013).

[7] A. A. Abdumalikov, Jr., O. Astafiev, A. M. Zagoskin, Yu. A. Pashkin, Y. Nakamura and J. S. Tsai, Phys. Rev. Lett. **104**, 193601 (2010).

[8] A. F. van Loo, A. Fedorov, K. Lalumière, B. C. Sanders, A. Blais, A. Wallraff, Science **342**, 1494 (2013).

[9] K. Lalumiére, B. Sanders, A. F. van Loo, A. Fedorov, A. Wallraff, and A. Blais, Phys. Rev. A **88**, 043806 (2013).

[10] I. Yeo, P-L de Assis, A. Gloppe, E. Dupont-Ferrier, P. Verlot, N. S. Malik, E. Dupuy, J. Claudon, J-M. Gérard, A. Auffèves, G. Nogues, S. Seidelin, J-Ph. Poizat, O. Arcizet, and M. Richard, Nature Nanotech. **9**, 106 (2014).

[11] A. V. Akimov, A. Mukherjee, C. L. Yu, D. E. Chang, A. S. Zibrov, P. R. Hemmer, H. Park, and M. D. Lukin, Nature (London) **450**, 402 (2007).

[12] T. Lund-Hansen, S. Stobbe, B. Julsgaard, H. Thyrrestrup, T. Sünner, M. Kamp, A. Forchel, and P. Lodahl, Phys. Rev. Lett. **101**, 113903 (2008).

[13] A. Huck, S. Kumar, A. Shakoor, and U. L. Andersen, Phys. Rev. Lett. **106**, 096801 (2011).

[14] R. C. Ashoori, Nature **379**, 413 (1996).

[15] D. R. Stewart, D. Sprinzak, C. M. Marcus, C. I. Duruöz, J. S. Harris Jr., Science **278**, 1784 (1997).

[16] P. M. McEuen, Science **278**, 1729 (1997).

[17] J. Claudon, J. Bleuse, N. S. Malik, M. Bazin, P. Jaffrennou, N. Gregersen, C. Sauvan, P. Lalanne, and J.-M. Gérard, Nature Photon. **4**, 174 (2010).

[18] D. Roy, Phys. Rev. B **81**, 155117 (2010).

[19] Y. Shen, M. Bradford, and J. T. Shen, Phys. Rev. Lett. **107**, 173902 (2011).

[20] E. Mascarenhas, D. Gerace, D. Valente, S. Montangero, A. Auffèves, and M. F. Santos, Euro-Phys. Lett. **106**, 54003 (2014).

[21] D. Gerace, H. E. Türeci, A. Imamoğlu, V. Giovannetti, and R. Fazio, Nat. Physics **5**, 281 (2009).

[22] F. L. Kien, S. Dutta Gupta, K. P. Nayak, and K. Hakuta, Phys. Rev. A **72**, 063815 (2005).

[23] C. A. Büsser and F. Heidrich-Meisner, Phys. Rev. Lett. **111**, 246807 (2013).

[24] H. Zheng and H. U. Baranger, Phys. Rev. Lett. **110**, 113601 (2013).

[25] Z. Yu *et al.*. Phys. Rev. Lett. **100**, 023902 (2008).

[26] C. Mu-Tian, Commun. Theor. Phys. **58**, 151 (2012).

[27] H. Lira, Z. Yu, S. Fan, and M. Lipson, Phys. Rev. Lett. **209**, 033901 (2012).

[28] D. Valente, S. Portolan, G. Nogues, J. P. Poizat, M. Richard, J. M. Gérard, M. F. Santos, and A. Auffèves, Phys. Rev. A **85**, 023811 (2012).

[29] Supplemental Material, see last section of this Letter after Acknowledgements.

[30] D. Valente, *Quantum Optics with Semiconducting Artificial Atoms*, PhD thesis, University of Grenoble, Néel Institute CNRS, 2012. Available on-line at: tel.archives-ouvertes.fr/docs/00/85/97/10/PDF/32830_VALENTE_2012_archivage.pdf

[31] A. Yariv and P. Yeh, *Photonics, Optical Electronics in Modern Communications*, sixth edition, ch. 4 (Oxford University Press, 2007).

[32] X. Duan, Nature **409**, 66 (2001).

[33] S. Coe-Sullivan, Nature Photon. **3**, 315 (2009).

[34] L. Bi, *et al.*, Nature Photon. **5**, 758 (2011).

[35] L. Fan, *et al.*, Science **335**, 447 (2012).

[36] M.-T. Cheng, X.-S. Ma, M.-T. Ding, Y.-Q. Luo, and G.-X. Zhao, Phys. Rev. A **85**, 053840 (2012).

[37] D-W. Wang *et al.*, Phys. Rev. Lett. **110**, 093901 (2013).

[38] S. Lepri and G. Casati, Phys. Rev. Lett. **106**, 164101 (2011).

[39] A. Badolato, K. Hennessy, M. Atatüre, J. Dreiser, E. Hu, P. M. Petroff, and A. Imamoğlu, Science **308**, 1158 (2005).

[40] V. Loo, C. Arnold, O. Gazzano, A. Lematre, I. Sagnes, O. Krebs, P. Voisin, P. Senellart, and L. Lanco, Phys. Rev. Lett. **109**, 166806 (2012).

[41] Mathieu Munsch, Nitin S. Malik, Emmanuel Dupuy, Adrien Delga, Joël Bleuse, Jean-Michel Gérard, Julien Claudon, Niels Gregersen and Jesper Mørk, Phys. Rev. Lett. **110**, 177402 (2013). Erratum: Phys. Rev. Lett. **111**, 239902 (2013).

[42] T. Lund-Hansen, S. Stobbe, B. Julsgaard, H. Thyrrestrup, T. Sünner, M. Kamp, A. Forchel, and P. Lodahl, Phys. Rev. Lett. **101**, 113903 (2008).

Chapter 4

Equilibrium and Disorder-induced behaviour in Quantum Light-Matter Systems

4.1 Introduction

Quantum phase transitions are a remarkable zero temperature phenomenon driven by quantum fluctuations [1]. Such transitions have been studied in many-body quantum systems where each quantum phase can be unambiguously defined. However, recent results show evidence that interesting aspects and important traces of the physics of novel quantum phase transitions may already be observed in the limit of very few interacting sites [2, 3, 4, 5, 6]. This is particularly clear in hybrid light-matter systems, such as coupled electromagnetic cavities doped with two level impurities, where a Mott insulating to superfluid crossover has been predicted for as few as six or seven sites [2]. These systems feature a composite fermion-boson excitation in each site, hence the term *hybrid*, and quantities like the variance in energy for each site have been used as markers for the transition between different phases [7]. However, entanglement, an unique quantum correlation with no classical analog which has been related to fundamental features of quantum phase transitions [8], may be regarded as a more adequate order parameter [9, 4]. In this work, we study the system entanglement to show how such quantum correlations relate to the behaviours the system may present.

One possible Hamiltonian describing doped and coupled cavities is the Jaynes-Cummings-Hubbard (JCH) model [2, 10] which, in some limiting approximations, mimics the more typical and simpler Bose-Hubbard one. The similarities between both models have prompted the use of the latter as a basis for the analysis of quantum phase transitions in the former both for a large [11] and a very small number of sites [12]. However, the analogy to this simpler model ignores the internal structure of each site what prevents one from exploring the increased complexity of the JCH system. The implementation of such systems has been proposed in different quantum optical setups such as planar lattices of one mode cavities each containing one quantum dot [13], photonic crystal microcavities [14], circuit quantum electrodynamics with a finite system approach [15], and in trapped ions [16]. One of the greatest advantages of all these setups is the combination of highly

controllable experimental conditions and the large effective size of each site that allows for the design of mesoscopic simulators of condensed matter systems.

In many cases the JCH system is naturally disturbed by noise that usually takes the system out of equilibrium. However, even in equilibrium, disordered imperfections in the system preparation may induce transitions that drastically change quantum phases and their correlations. Disorder may manifest itself in very different and even opposite effects. The lattice imperfections, that differ from site to site, may suppress quantum coherence inducing the spatial localization of quantum states destroying the system fluidity, which leads to compressible, despite non-fluid, glassy phases [17]. However, disorder may induce fluidity under certain circumstances [6, 18, 19]. The hybrid nature of the system also leads to interesting effects under the action of disorder, as we show in the following sections.

In this chapter, we show that the entanglement between different constituents of the JCH system can be used not only to characterize the already known phase transitions, also present in the Bose-Hubbard model, but also, and more importantly, to identify new behaviour involving the nature, either hybrid or bosonic, induced by the more complex JCH interaction. We address small and large quantum systems, extremes that present similarities and differences that are of great interest: while few sites are experimentally feasible in a controllable way, phase transitions are better defined in large samples. We also analyse the entanglement and the disorder-induced effects of the JCH hamiltonian. For the analysis of the small system we enter deeply in the statistics of the ensembles induced by disorder, since in principle a physical observer could perform spectroscopic measurements of the system structure and obtain the disordered pure states (or at least quasi-pure) pertaining to the induced ensembles. For the analysis of the large system we resort to stochastic-mean-field-theory (SMFT), which was recently developed in [20, 19] and allows us to study on site statistics. We show how the statistics of the system change under the various ways in which disorder may set in and also show the disorder-induced phase transitions.

The analysis of the clean system is developed in section II with one subsection for the small limit and another for the large limit. The disordered small system is addressed in section III and the disordered large system is addressed in section V after a recollection of SMFT in section IV. Section VI concludes the chapter.

4.2 The Hybrid System: Jaynes-Cummings-Hubbard Hamiltonian

The system studied here features a chain of sites each of which containing composite excitations, also known as polaritons, created by the interaction of a boson and a fermion. A typical experimental proposal for these systems is devised in resonant cavities, the bosons being the photons that occupy the cavity mode and the fermions being two-level electronic transitions of the onsite dopants, as depicted in figure (4.1) and described in [2, 21]. The Hamiltonian of these coupled doped cavities (with two level impurities) is the so called Jaynes-Cummings-Hubbard model and it is given by

$$\mathcal{H} = \sum_{\langle i,j \rangle}^{n} [\mathcal{S}_i + \mathcal{T}_{(i,j)}], \tag{4.1}$$
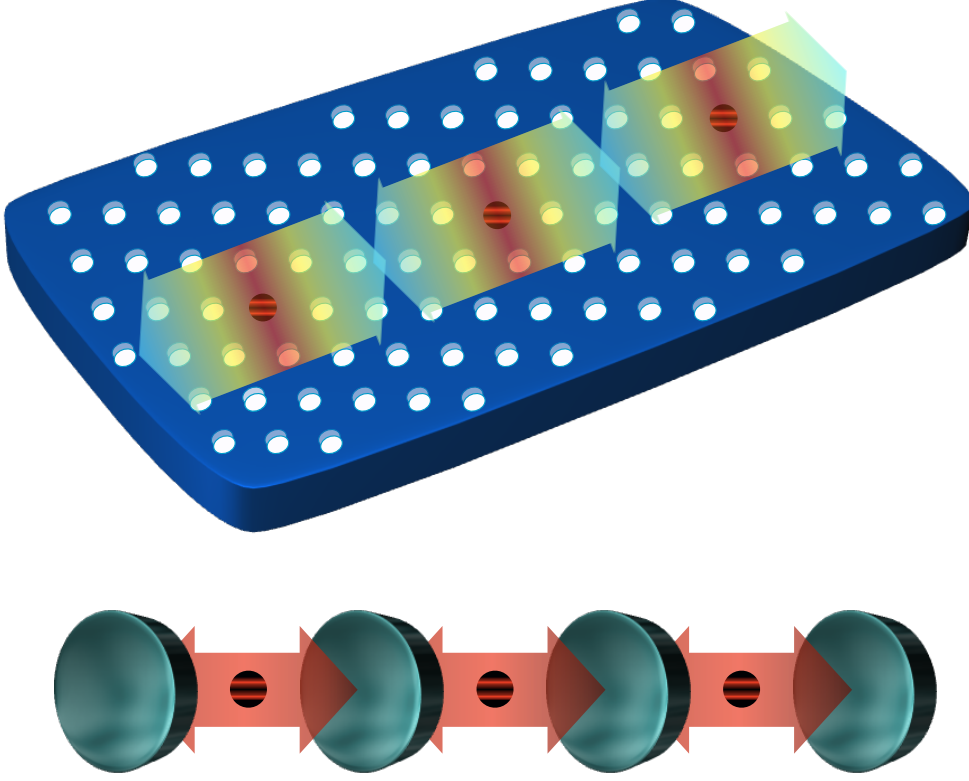
Fig. S.4.1: Coupled cavities doped with two-level systems. The figure shows one possible realization of this system, in this case in photonic crystals, where cavities are defects in the periodic structure of the crystal. The two-level systems can be excitons in quantum dots or electronic levels of dopant atoms, for example.

with n being the number of sites, and $\mathcal{S}_i$ being the intra site Jaynes-Cummings interaction between the dopant and the resonator

$$\mathcal{S}_i = \omega_i a_i^\dagger a_i + \nu_i \sigma_i^\dagger \sigma_i + g_i (\sigma_i^\dagger a_i + \sigma_i a_i^\dagger). \tag{4.2}$$

The ith site annihilation operators are a_i and σ_i for the bosonic and fermionic species, respectively. In Eq. (4.1), $\mathcal{T}_{(i,j)}$ describes the photon hoping, or tunneling, between nearest neighboring sites

$$\mathcal{T}_{(i,j)} = -A_{(i,j)}[a_i^\dagger a_j + a_i a_j^\dagger]. \tag{4.3}$$

The coupling strength between the two level system and the cavity in the ith site is given by g_i, and the photon tunneling strength between nearest cavities is $A_{(i,i+1)}$. The photon frequency at the ith site is ω_i and ν_i is the transition frequency of the dopant of the respective site, thus we define the ith site detuning $\Delta_i = \nu_i - \omega_i$.

The polaritons are eigenstates of the intra-site (Jaynes-Cummings) hamiltonian and are given by $|n+\rangle = \sin(\theta_n)|g\rangle|n\rangle + \cos(\theta_n)|e\rangle|n-1\rangle$ and $|n-\rangle = \cos(\theta_n)|g\rangle|n\rangle - \sin(\theta_n)|e\rangle|n-1\rangle$, with $\tan(2\theta_n) = -g\sqrt{n}/\Delta$. The states $|n\rangle$ are photon number states and $|g\rangle$ and $|e\rangle$ are the ground and excited states of the dopant inside the cavity. Finally, the number of particles operator in the ith site is given by $N_i = a_i^\dagger a_i + \sigma_i^\dagger \sigma_i$.

4.2.1 behaviour of Small Sample Systems

Recent works show that the system described in the last session undergoes a Mott-superfluid phase transition when going from small hoping to large hoping or from negative detuning to positive detuning [2, 10]. In the first case the transition is induced because the hoping strength circumvents the photon blockage regime (non-linearity due to the dopant-cavity interaction) and in the second case the excitations are directly driven from mainly electronic (electrons are not able to hop) to mainly photonic, hence the fluidity. This phase transition can be witnessed by single site properties. For example, when the system is isolated and the average occupation number per site $\langle N_i \rangle$ is one (same number of excitations and sites), the variance of N_i for any given site is a good order parameter [2, 3]: in the Mott phase each site has a single particle and there is no number fluctuation whereas in the superfluid phase the onsite number variance is maximum. This analysis begins to fail when one takes into account interactions with the environment and spatial fluctuations that may not preserve the total number of particles in the system. For instance, dissipation introduces variances of the occupation number in each site and $\text{var}(N_i)$ may overestimate fluidity. Furthermore, although the measure of $\text{var}(N_i)$ hints at the type of excitation that dominates each phase it cannot reveal this fundamental property in detail because it does not fully distinguish between photons, electrons and polaritons.

We proceed to show that the entanglement between different constituents not only reproduces previous results but actually allows for the identification of a new crossover that the previous analysis did not reveal.

In order to quantify the entanglement between the various components of the system we choose the negativity measure [22], which is very convenient to calculate. It should be reminded that null negativity does not necessarily imply null entanglement, in fact, null negativity means null or bound entanglement. However, any non zero value of negativity guarantees some form of distillable entanglement in the system what will prove to be enough for distinguishing the different quantum phases of the system as a whole. Given the quantum state of any two constituents A and B of the system, their negativity can be found by partially transposing their reduced density matrix $R = \rho_{AB}^{T_A}$ and then summing up the moduli of the negative eigenvalues of R.

We begin with the case of small systems, where the diagonalization of the Hamiltonian is computable, by looking at properties of the lowest energy state $|G\rangle$ with the constraint of having equal number of excitations and sites $\mathcal{H}|G\rangle = E_n|G\rangle$. In other words, $|G\rangle$ is the lowest energy eigenstate of the Hamiltonian having $n = \langle \sum_i^n N_i \rangle$, with N_i the number operator at the ith site. Consider, now, a cluster of two sites, that is the smallest possible such system. Even for this very basic *unit cell*, the entanglement between the sites clearly presents the signatures of Mott and superfluid phases that were found for much larger systems in previous works. In the Mott phase (with one polariton per site) there is no entanglement between sites with the Mott insulating state being $|G(\text{MI})\rangle = |1-\rangle|1-\rangle$ (for two sites). In the superfluid phase and when the excitations become mainly photonic the sites become entangled, with the superfluid state for two sites (described in [3]) given by $|G(\text{SF})\rangle = |g\rangle|g\rangle \left[\frac{1}{\sqrt{2}}|11\rangle - \frac{1}{2}(|20\rangle + |02\rangle) \right]$. It should be kept in mind that for the finite
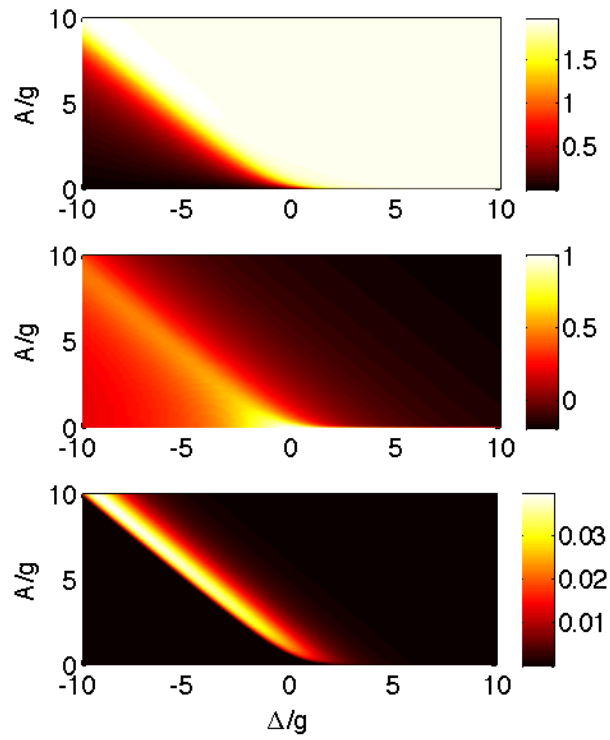
Fig. S.4.2: Results for a two site system. (Top-a) Entanglement between the sites. (Middle-b) In-site Entanglement. (Bottom-c) Atom-atom entanglement.

system analysis there is no phase transition, only a smoother crossover, even though the phase transition terminology is commonly adopted. The behaviour of the system (phase-like diagram), quantified by the entanglement between different constituents, is depicted in figure (4.2), where we show the entanglement between sites, the in-site entanglement and the entanglement between atoms.

The site-site entanglement shows the phase crossover as partially presented in [4]. When the site-site entanglement is negligible the system resembles a Mott-insulator and when the site-site entanglement is non-negligible the system presents superfluid-like behaviour. Thus the site-site entanglement indicates the regimes in which the system is insulating and superfluid with small and large values of entanglement, respectively [figure (4.2,a)]. In order to quantify the polaritonic behaviour we can look at the in-site entanglement that measures how correlated are the photonic field and the electronic transition in a given cavity (or a site)[figure (4.2,b)]. In the Mott-like regime (small site-site entanglement) the in-site entanglement is significant, indicating that the system presents polaritonic behaviour. Deep in the superfluid-like regime (large site-site entanglement) the in-site entanglement is small, indicating predominant photonic behaviour. However, during the crossover (as a function of either A or Δ) entanglement presents a non-monotonic behaviour, with a region where it is maximum. Such non-monotonic increase, which is even more pronounced in the atom-atom entanglement [figure (4.2,c)], suggests that as the system size increases and reaches the thermodynamic limit a phase transition should be verifiable, i.e. since at the point of the phase transition there are fluctuations over all length scales, more degrees of freedom interact with each other such that entanglement can exist between more degrees of freedom. Furthermore, the regime in which in-site and site-site entanglement coexist corresponds to a polaritonic-superfluid, rather then just a photonic-superfluid.

4.2.2 Large Sample Systems and the polariton-photon crossover

We can also obtain a wider view of the system phase diagram varying the number of polaritons in the system. In order to do that we can couple the system to a chemical reservoir of polaritonic particles with chemical potential μ (at zero temperature), such that the system is in equilibrium with this reservoir. The chemical potential can be explicitly included in the system Hamiltonian $\mathcal{H} \to \mathcal{H} - \mu \sum_i N_i$.

For large (infinite) systems we adopt the mean-field approach, in which we treat a small cluster of sites interacting with a mean field, that is, a classical approximation of the rest of the chain (to which we refer to as an environment). This approach gives a factorable approximation of the non-factorable tunneling (or hoping) term by approximating the operators for their mean values plus a small fluctuation (in this case a quantum fluctuation) $a = \langle a \rangle + \delta a$. The mean field hamiltonian for the cluster becomes

$$\mathcal{H}_{\text{MF}} = \sum_{\langle i,j \rangle (\text{cluster})} [\mathcal{S}_i + \mathcal{T}_{(i,j)}]$$
$$+ \sum_{\langle i(\text{cluster}),j(\text{environment}) \rangle} -A_{(i,j)}[\alpha_j^* a_i + \alpha_j a_i^\dagger - |\alpha_j|^2], \quad (4.4)$$

with $\langle a \rangle = \alpha$ being the mean-field order parameter that has to be self-consistently determined by minimizing the ground state energy. The phase diagram as a function of the chemical potential and the hoping frequency is shown in figure (4.3) for large systems.
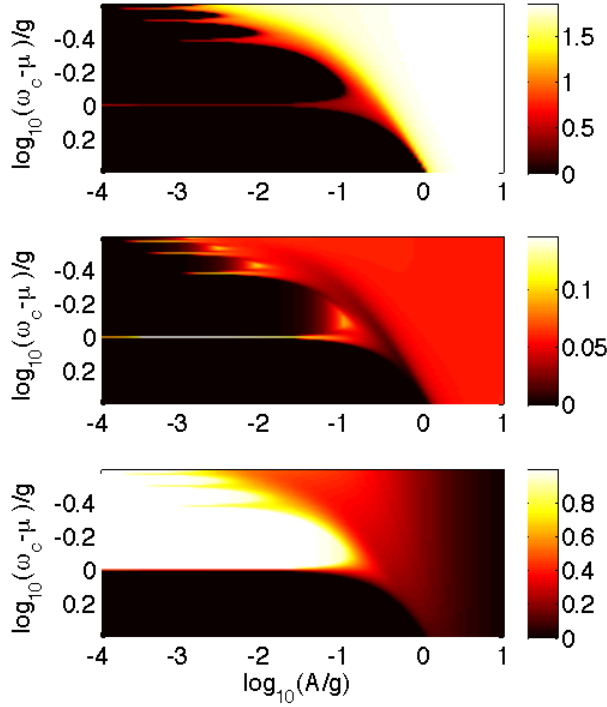
Fig. S. 4.3: (Top) The Mean-field parameter. (Middle) Entanglement between the sites in the cluster. (Bottom)The in-site entanglement, that is, the entanglement between the dopant and the oscillator mode in mean field theory. All data with a four-sites cluster with the dimension of each oscillator truncated to 6 photons and zero detuning ($\Delta = 0$).

Varying the chemical reservoir we can see the Mott lobes (each lobe corresponding to plateaus of different integer numbers of polaritons) in the infinite system [figure (4.3)]. The mean field parameter is null in the Mott phase and is positive in the superfluid phase. Only in this case we compute a site purity (one minus the purity more precisely) as the estimate of the entanglement between such site and the rest of the chain (in this case, the cluster). Although this entanglement is not strictly zero in all of the Mott phase it still gives a fair account of the phase diagram and the lobe structure. We have considered a four-sites cluster, which is a rather small cluster, even though it already requires a considerable computational effort. Larger clusters would increase the precision of the site-cluster entanglement. The site-cluster entanglement is maximum in the lobe borders (middle panel of fig. (4.3)), which, again, indicates strong polaritonic fluidity in the vicinity of the phase transition.

Now, looking at the in-site entanglement (bottom of fig. (4.3)), which can be regarded as the very essence of the polaritons, we can see the whole picture with the overlay of the Mott-Superfluid and Hybrid-Boson crossover. The highest in-site entanglement is in the Mott-lobes and the lobe structure can also be defined by this quantity. Outside the lobes fluidity sets in, however the in-site

entanglement is still very high indicating that the system has not yet undergone the Hybrid-Boson crossover despite having changed from insulating to superfluid. Farther away from the lobes and deeper into the fluid phase we finally observe the in-site entanglement vanishing indicating that the system finally turns bosonic.

4.3 Disordered Small Quantum systems

Every physical system presents imperfections (disorder), that is, the system parameters may vary from site to site. There are many possible origins of disorder, for instance, imprecisions in the system manufacturing process, thermal fluctuations, and fluctuations induced by other uncontrollable electromagnetic sources in the system environment. One way to study the effect of disorder is to describe the parameters of each site as a stochastic variable ξ_i and the Hamiltonian becomes dependent on the stochastic parameters $\mathcal{H}\{\xi_i\}$. Naturally, the system ground state becomes dependent on the values assumed by the system parameters $|G\rangle \rightarrow |G(\{\xi_i\})\rangle$ and there emerges a new state, an average state

$$\rho = \int dp(\{\xi_i\})|G(\{\xi_i\})\rangle\langle G(\{\xi_i\})|, \tag{4.5}$$

that contains the statistics of the effects induced by the static disorder, with $dp(\{\xi_i\})$ being the distribution measure of the disorder, such that it gives all moments of the site parameters $\overline{\xi_i^k} = \int dp(\{\xi_i\})\xi_i^k$. We choose to analyse only uncorrelated disorder such that the global measure is a product of local measures $dp(\{\xi_i\}) = \prod_i P(\xi_i)d\xi_i$, with gaussian distributions $P(\xi_i) = \frac{1}{\sqrt{2\pi}\delta}\exp\{-\frac{(\xi_i - \overline{\xi_i})^2}{2\delta^2}\}$. The magnitude of disorder is then given by the distribution width or the mean square deviation δ.
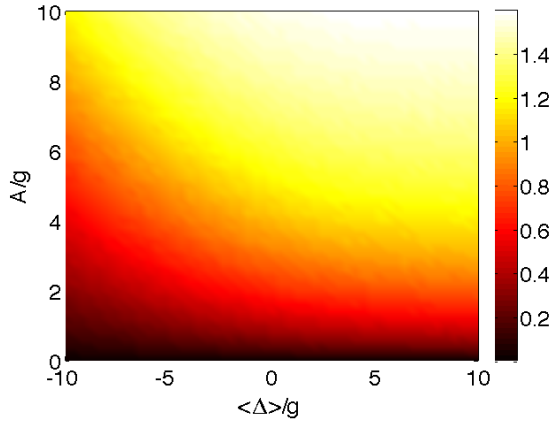
Fig. S. 4.4: The ensemble average entanglement $\overline{E}[\rho]$ between the two sites under disorder in the matter light detuning Δ (more specifically in the light frequency) on the phase diagram with $\delta(\Delta) = 10g$.

We can then characterize the average properties of the system given that it presents disorder. For instance we can look at the entanglement description of the phase diagram, only now we average the

entanglement over the pure state ensemble generated by the different values assumed by the system parameters. We remark that the pure state ensemble given in equation (4.5) is a physically realizable ensemble [24], since in principle the experimentalist can perform spectroscopic measurements and obtain the values assumed by the parameters in that particular sample system and then prepare the system ground state. We can define the reduced states $\rho_{AB}(\{\xi_i\}) = \mathrm{tr}_E\{|G(\{\xi_i\})\rangle\langle G(\{\xi_i\})|\}$, with the trace being performed over the environment of A and B. For instance, if we are looking at the atom-atom entanglement then we trace out the field, so the field would be the environment in this case. Therefore, we can define the average entanglement between any constituents A and B

$$\overline{E}[\rho_{AB}] = \int dp(\{\xi_i\}) E[\rho_{AB}(\{\xi_i\})], \tag{4.6}$$

which is physically realizable since the ensemble of ground states also is [25, 26]. Notice that the average entanglement of the ensemble is in general different than the entanglement of the average state with the usual hierarchy $\overline{E}[\rho_{AB}] \geq E[\rho_{AB}]$, with the average state $\rho_{AB} = \int dp(\{\xi_i\}) \rho_{AB}(\{\xi_i\})$.
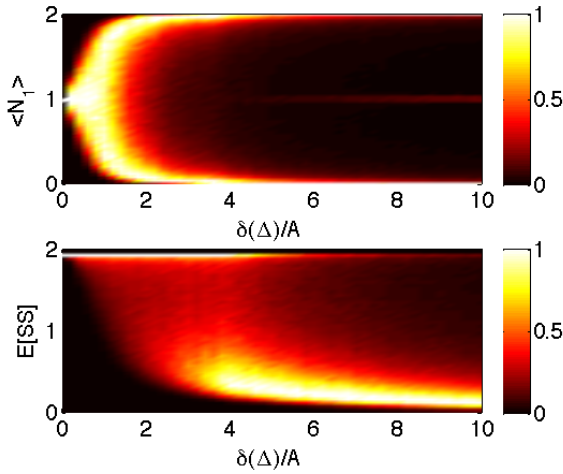
Fig. S.4.5: Probability distributions induced by disorder in the matter light detuning. (Top) Renormalized histogram $P(\langle N_1 \rangle)$ of the site occupation number as a function of disorder. (Bottom) Renormalized histogram $P(E)$ of the site-site entanglement as a function of disorder. The light hoping is $A = g$ and average detuning $\langle \Delta \rangle = 5g$.

In what follows in this section we consider only two sites of the jaynes-Cummings-Hubbard hamiltonian.

4.3.1 Disorder in the matter-light detuning

Now we can describe the effects induced by disorder in each of the parameters individually, detuning Δ, hoping A, and matter light coupling g. Let us begin by analyzing disorder only in the cavity-atom detuning, thus $\{\xi_i\} = \{\Delta_i\}$ (see figures (4.4) and (4.5)). As can be seen in fig. (4.4) the average entanglement between sites seems to decrease over the whole phase diagram in comparison with the clean case of fig. (4.2a).
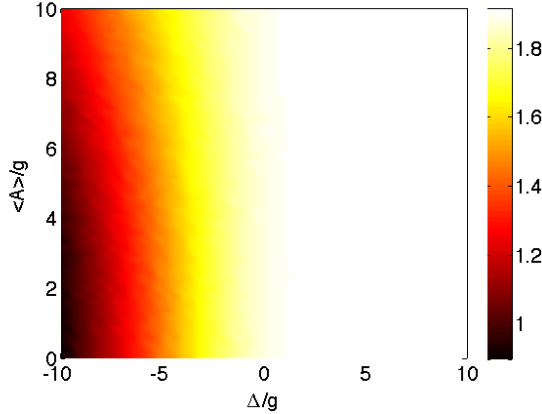
Fig. S.4.6: Effects of static disorder in the light hoping A on the phase diagram. The ensemble average entanglement $\overline{E}[\rho]$ between the two sites. Disorder of $\delta(A) = 10g$.

The decrease of site-site entanglement indicates that the excitations tend to localize through an Anderson-like mechanism. For instance, starting with the system in the superfluid phase as we increase the detuning disorder the distribution of the single site number occupation $P(\langle N_1 \rangle)$ is broadened and then it becomes a two peaked distribution (see top panel of figure (4.5)). In the regime in which the distribution $P(\langle N_1 \rangle)$ presents two peaks the system is fully localized, such that one of the peaks corresponds to all excitations in cavity one and the other corresponds to zero excitations in the cavity. This extreme regime of localization can be regarded as a bosonic bunching: the large disorder in the cavity line width allows for realizations in which the cavity has a very low frequency such that it is energetically favorable to fit more than one excitation in one cavity instead of distributing the excitations over the sites. For two sites and two excitations the state can be approximately given by $|2\rangle|g\rangle|0\rangle|g\rangle$ or $|0\rangle|g\rangle|2\rangle|g\rangle$ with the atoms in their ground states.

The parameters in fig. (5) are such that the system is in the superfluid phase in the clean limit. In this case, as expected, the distribution of the site-site entanglement $P(E[SS])$ shows a peak at the maximum value (bottom panel of the figure). However as disorder increases there emerges a second peak close to the minimum value corresponding to localized states. Thus the ensemble presents both superfluid and insulating *states* for intermediate values of disorder. The presence of the two sorts of states can be regarded as a precursor of a glassy phase [5], which we will show to be true with the large system analysis. Furthermore, as disorder increases even further the system becomes fully localized and the site-site entanglement distribution becomes single-peaked at very small values of entanglement.

4.3.2 Disorder in the photon hopping

Disorder in the photon hoping generates a different effect (see figures (4.6) and 4.7). Carrying out the same analysis as for disorder in the detuning, we see that the average site-site entanglement increases in the region where a Mott phase exists in the clean limit, while it remains practically unaltered in the superfluid phase. Fluctuations in the hoping may actually induce a glassy fluid
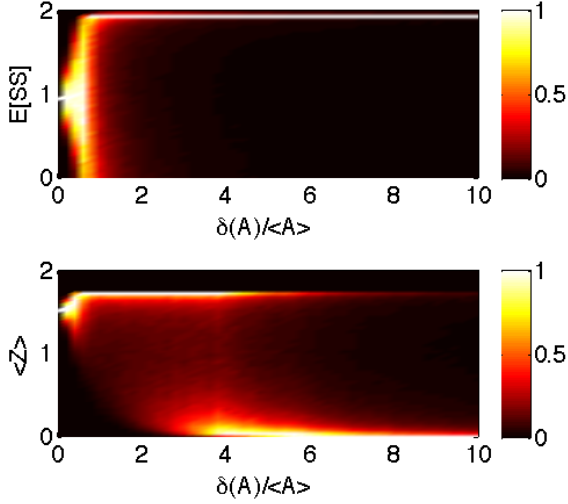
Fig. S.4.7: Probability distributions induced by disorder in the light hoping. (Top) Renormalized histogram $P(\langle Z \rangle)$ of the total atomic occupation number as a function of disorder. (Bottom) Renormalized histogram $P(E)$ of the site-site entanglement as a function of disorder. The average light hoping is $\langle A \rangle = 1g$ and detuning $\Delta = -2g$.

phase [6, 18, 19], that is, disorder allows realizations in which the hoping is stronger than the photon blockade and those realizations may prevail. The A-disorder may also suppress the polaritonic behaviour which can be seen as a decrease in the atomic population. We can also look at the distribution for the total atomic excitation $Z = \sum_i \sigma_i^\dagger \sigma_i$ as a function of disorder starting from the system at the Mott phase in the clean limit. The distribution $P(\langle Z \rangle)$ is very asymmetric and as disorder increases it concentrates at the extreme values assumed by $\langle Z \rangle$. One of the extremes corresponds to polaritonic superfluidity and the other to photonic superfluidity, with the latter prevailing in the limit of very large disorder. This can be corroborated by the entanglement distribution $P(E[\text{SS}])$.

4.3.3 Disorder in the matter-light coupling

Finally we analyse disorder in the matter light coupling g (see figure (4.8)). A first look at the g-disordered average entanglement (not shown here since it resembles very closely the Δ-disorder case) suggests that disorder in the Jaynes-Cummings coupling also induces localization, that is, disorder allows a great number of meaningful realizations in which the sites are almost unentangled and the excitations tend to bunch. However, the g-disorder induced distribution of the site occupation number $P(\langle N_1 \rangle)$ (top panel of fig. (4.8)) is very different than the one induced by Δ-disorder (which we showed that presents localization). In the current case the $P(\langle N_1 \rangle)$ distribution shows three peaks, the extreme ones corresponding to bunching similar to the Δ-disorder case, and a middle one that corresponds to states in which the excitations are still equally distributed among the sites. Disorder in the matter-light coupling induces states with Mott-like features in which the site-site entanglement vanishes (see middle panel of the figure). In fact, this is the meaning of the

middle peak in $P(\langle N_1 \rangle)$: some sites undergo a superfluid-insulating transition through a Mott-like mechanism. Since the distribution of the atomic occupation $P(\langle Z \rangle)$ (bottom panel of fig. (4.8)) is narrowly centered at an appreciable (although not extreme) value we may conclude that the system nature becomes mainly polaritonic, and thus presenting both Mott states (middle peak in $P(\langle N_1 \rangle)$ and polaritonic bunching (the extreme peaks in $P(\langle N_1 \rangle)$. This suggests that the system behaves very similarly to an Anderson-Mott insulator [27].
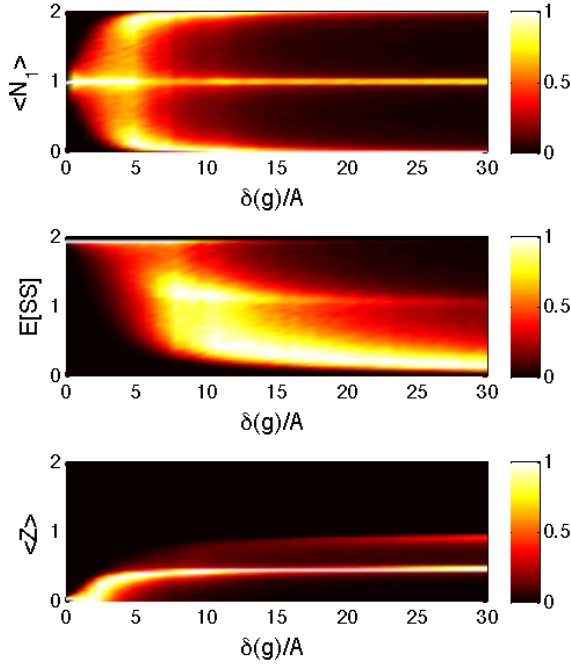
Fig. S.4.8: Probability distributions induced by disorder in the matter-light coupling g. (Top) Renormalized histogram $P(\langle N_1 \rangle)$ of the site occupation number as a function of disorder. (Middle) Renormalized histogram $P(E)$ of the site-site entanglement as a function of disorder. (Bottom) Renormalized histogram $P(\langle Z \rangle)$ of the total atomic occupation number as a function of disorder. The light hoping is $A = 1g$ and detuning $\Delta = 5g$.

The presence of superfluid, Mott and Anderson-like states for intermediate disorder in the coupling g suggests that glassy phases would be induced in larger systems of the Jaynes-Cumming-Hubbard type. In fact, a different situation was analysed in [28], in which there is disorder in the number of impurities per cavity. Since the number of atoms fluctuates then the intensity with which light couples to matter also fluctuates, and it was shown in [28] that such disorder induces glassy phases. Interestingly, even small versions of the quantum system present evidence of many diverse phases and behaviours expected only for larger quantum systems, which we discuss in the next section.

4.4 Disordered Large Quantum Systems

To address the physics of large disordered quantum systems we apply a recently developed technique, namely stochastic-mean-field-theory (SMFT) [20]. This method has been shown to provide appropriate descriptions for the effects of disorder without over estimating coherence and fluidity and has already been successfully applied to the disordered Bose-Hubbard model [20]. The main reason for the effectiveness of the method is self-consistently determining the probability distribution for the mean-filed parameter $P(\alpha)$ (instead of α itself) through an iterative process.

4.4.1 Stochastic-Mean-Field-Theory

Firstly we describe how to account for any on site disorder (with constant photon hopping A), afterwards we describe the special case of hopping disorder. In the mean-field description every site has a number z of nearest neighbors. The mean-filed hamiltonian for the kth site depends only on the scaled sum

$$\eta_k = \sum_j A_{\langle k,j \rangle} \alpha_j. \tag{4.7}$$

The probability distribution for η (we drop the site index for convenience) can be found from a simple and fundamental relation known as the convolution theorem

$$Q(\eta) = \int \ldots \int \prod_i^z d\alpha_i P(\alpha_i) \delta \left(\eta - A \sum_j^z \alpha_j \right), \tag{4.8}$$

which reduces to the Fourier transforms $\varphi(\beta) = \int d\alpha P(\alpha) e^{i\beta\alpha}$ and

$$Q(\eta) = \frac{1}{2\pi A} \int d\beta [\varphi(\beta)]^z e^{-i\eta\beta/A}. \tag{4.9}$$

The first step in the algorithm is to choose a trial distribution for α (different from a delta centered at $\alpha = 0$) and the desired distribution (in our case a Gaussian) for the disordered parameter ξ (the detuning or matter-light coupling). Then we assume all α_j to be independent form each other and we determine the self-consistent distribution

$$P(\alpha) = \int \int dq(\eta) dp(\xi) \delta(\alpha - \langle a \rangle), \tag{4.10}$$

such that $\langle a \rangle = \langle G[\xi, \eta] | a | G[\xi, \eta] \rangle$, with $dq(\eta) = d\eta Q(\eta)$. The procedure is iterated until we observe convergence, that is, until $P^{(i)}(\alpha)$ in the ith step is statistically close to $P^{(i+1)}(\alpha)$. Finally, the average state of the site is given by the disorder-induced ensemble

$$\rho = \int \int dq(\eta) dp(\xi) |G[\xi, \eta]\rangle \langle G[\xi, \eta]|. \tag{4.11}$$

To account for disorder in the photon hopping we must add another step to the procedure. It is convenient to work with the variable $\phi = A\alpha$ whose probability distribution is given by (we use a subindex to distinguish the various distributions)

$$P_\phi(\phi) = \int \int dA d\alpha P_A(A) P_\alpha(\alpha) \delta(A\alpha - \phi). \tag{4.12}$$

Then we can determine $Q(\eta)$ through the usual Fourier transforms $\varphi(\beta) = \int d\phi P_\phi(\phi) e^{i\beta\phi}$

$$Q(\eta) = \frac{1}{2\pi} \int d\beta [\varphi(\beta)]^z e^{-i\eta\beta} \tag{4.13}$$

and the procedure follows as for the case of on site disorder.

4.5 Disorder-induced transitions

The results presented in this section will allow us to conclude that the asymptotic effects of disorder (very large disorder) in the thermodynamical limit are very similar to the effects in small samples of the system. However, there are some significant quantitative differences, for instance, there are in fact phase transitions induced by disorder in the thermodynamical limit. It should also be pointed out that our approach is a bit different in this section. From now on we work with single-site mean-field-theory rather than cluster-mean-field-theory, and we follow this strategy to avoid higher computational demands. This limits the applicability of the method and quantities like the site-cluster entanglement are no longer addressable. Nonetheless, we are able to increase the local effective dimension of the oscillator to 20 states. Another difference between the approaches for small and large samples is that in the first case we fix the number of excitations in the system and it does not change as disorder increases. This is not the case in the present section, and in fact, the total number of excitations may change as a function of disorder.

Using the SMFT approach we are able to perform an analysis of the thermodynamical limit. The method allows us to recover the probability distributions (under the single-site-mean-field approximation) for the various quantities we analyse to characterize the system. The average mean field parameter, for instance, can be readily evaluated as $\langle \alpha \rangle = \int \alpha P(\alpha) d\alpha$. We follow the same ordering of presentation of the results: Firstly, we show the results for the detuning disorder, then for the hopping disorder and finally for the matter-light coupling. Given the unlimited nature of the disorder distribution we analyse (Gaussian) it follows that the insulating phases we present below are of glassy nature. Such phases have non vanishing number variance as opposed to the Mott-insulating phases [19]. Therefore glassy insulators can be characterized by vanishing superfluidity and non vanishing compressibility (which can be related to the number variance). However, we do not show the compressibility of the system, since the result can be readily anticipated. The compressibility increases in the insulating regions, thus glassy phases are established.

4.5.1 Disorder in the matter-light detuning

As show in figure (4.9) the net effect of disorder in the detuning is to induce insulating behaviour, indicated by the destruction of the fluid phase surrounding the Mott-lobes, in fact, the lobe structure disappears for significant amounts of disorder. The in-site entanglement shows that the system remains in superpositions of light and matter excitations for intermediate values of disorder. However, as we increase disorder the in-site components are either highly entangled or unentangled with higher probability. We can see the distributions as functions of disorder in figure (4.10). The transition from fluid to insulating is evident in the distribution of the mean field parameter. All this corroborates the small system predictions and once again the system is mainly photonic for strong disorder. Interestingly, in the present limit the distribution of cavity excitation ($P\langle N \rangle$ in figure (4.10)) is a series of delta functions (with different weights) centered at integer values of the mean occupation, which is in agreement with the insulating and bunched behaviour.
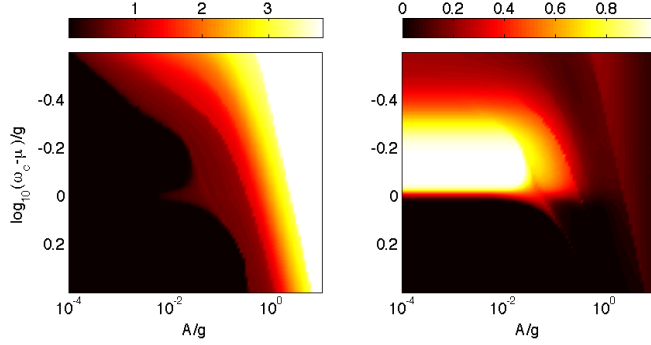
Fig. S.4.9: Stochastic mean field results for disorder in the matter-light detuning with $\delta(\Delta) = 0.1g$ and $\langle \Delta \rangle = 0$. (Left) The average mean field parameter. (Right) The entanglement of the average state.

4.5.2 Disorder in the photon hopping

The effects that hopping disorder produces in the system are opposite to those produced by detuning disorder, as it is the case for small systems. In the current case disorder induces induces a fluid phase, as we can see in figure (4.11), and decreases the in-site entanglement indicating that the system becomes more photonic in nature. As in other situations analysed, by looking at the distributions of the physical quantities as a function of disorder (not shown), we were able to observe the transition from insulating to fluid behaviour as disorder in the hopping parameter increased.

4.5.3 Disorder in the matter-light coupling

Finally, the effects of disorder in the light-matter coupling, once again, resemble the ones induced by the detuning disorder. Even though both the detuning and coupling disorders induce insulating behaviour, it should be pointed out they do it through very different physical mechanisms.

In the detuning case cavities may be in lower frequencies in many sites which allows for more photons to localize (even several photons per cavity). In the coupling case the strength of the polaritonic nature may be increased in cavities that are strongly coupled to their corresponding matter components inducing Mott behaviour. And as we can see in figure (4.12 bottom left) in comparison with fig. (4.10 bottom left) the distribution for the cavity population does not present the higher order peaks, only the ones corresponding to zero or one polariton per cavity. This behaviour is due to the fact that the sites with strong matter-light coupling prevent the accumulation of larger numbers of particles per site (Mott mechanism).

Adding the information provided by the entanglement and atomic population distributions, we have found that a fraction of the sites assumes the Mott behaviour and the rest are localized or even empty. Thus, we corroborate the small system analysis that suggests that the system behaves very similarly to the Anderson-Mott insulator [27]. It is, however, strikingly interesting that in one case (disorder in the detuning) it is the low frequency sites that dominate the resulting statistical behaviour and in the other case (disorder in the matter-light coupling) it is the strongly coupled sites that dominate, even though the distribution of the disorder parameter is gaussian and unbiased.
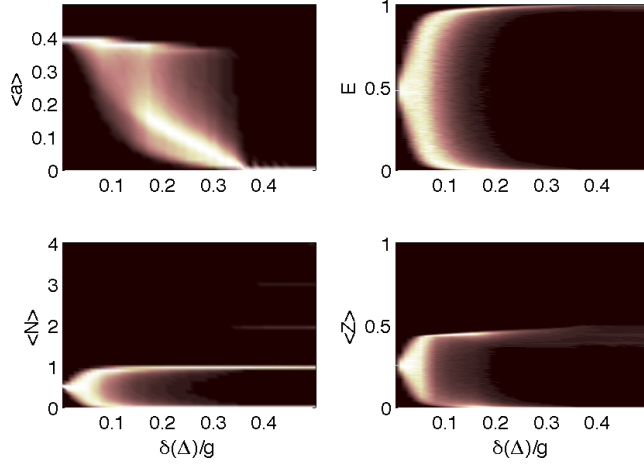
Fig. S.4.10: Probability distributions as a function of disorder in the matter-light detuning with $A = 10^{-1.9}g$, $(\mu - \omega_c)/g = -1$ and $\langle \Delta \rangle = 0$. Black corresponds to vanishing probability. (Top-Left) Distribution for the mean field parameter, (Top-Right) for the entanglement of the average state, (Bottom-Left) for the cavity excitation and (Bottom-Right) for the atomic excitation.

4.6 Conclusions

We were able to characterize the phase diagram and the Mott-Superfluid transition of small and large samples of the Jaynes-Cummings-Hubbard Hamiltonian using entanglement measures between the various possible partitions of the components of the system. In particular, we showed that these non-local measures identify more clearly where the transition happens. Furthermore, and more importantly, we also showed that entanglement measures distinguish which type of excitation dominates each phase which in turn allowed us to identify a crossover that is particular to this Hybrid system and does not have a purely bosonic analog. This behaviour splits the superfluid regime into two, the first one dominated by polaritons and the second is purely photonic.

For the disordered system we have shown that the simple statistical treatment of small systems can be quite instructive and allows us to draw conclusions that can be corroborated by the large system limit. We have shown that disorder both in the light-matter detuning and light-matter coupling induce insulating phases, however they do it through very different physical mechanisms. The former allows for photonic localization and bunching, the latter induces Mott behaviour in a fraction of the sites that prevents the bunching. Furthermore, the cavity-cavity coupling disorder induces a glassy fluid phase. The rich in-site structure of the system leads to these diverse disordered phases with very different statistics and physical meanings.

A great amount of work remains to be done on the characterisation of the JCH system. As a valuable point we suggest that an appropriate and efficient method should be applied to the study of the superfluid phase (with and without disorder) in which the mean field approach adopted here is limited. Once could use Density Matrix Renormalization Group (DMRG) for one-dimensional systems and Dynamical Mean Field Theory (DMFT) for high dimensional systems.

Finally, it is worth mentioning once again the mesoscopic aspect of the systems proposed to
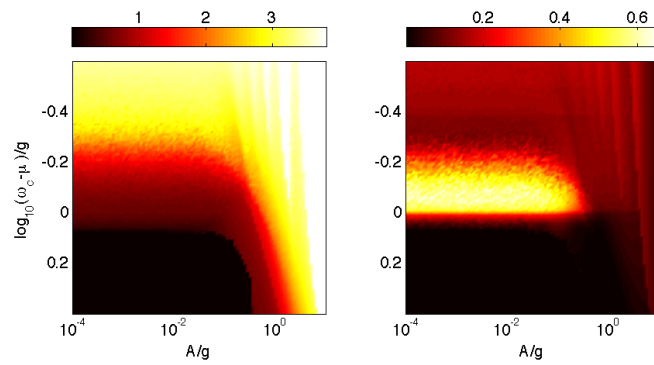
Fig. S.4.11: Stochastic mean field results for disorder in the hopping with $\delta(A) = 0.1g$ and $\Delta = 0$. (Left) The average mean field parameter. (Right) The entanglement of the average state.

implement the JCH Hamiltonian as well as the increasing ability to manipulate the different parameters of these systems, sometimes even at an individual level. These properties suggest that it will be possible to carry on a thorough experimental investigation of the effects of disorder and its relation to phase transitions and entanglement in many body physics in the near future.
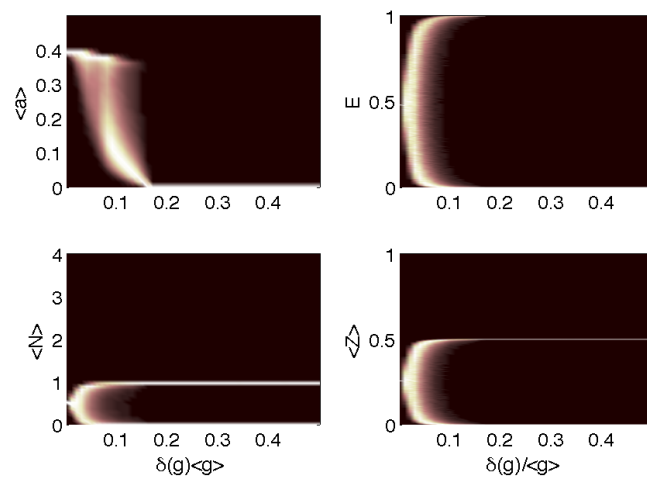
Fig. S.4.12: Probability distributions as a function of disorder in the matter-light coupling with $A = 10^{-1.9}g$, $(\mu - \omega_c)/g = -1$ and $\Delta = 0$. Black corresponds to vanishing probability. (Top-Left) Distribution for the mean field parameter, (Top-Right) for the entanglement of the average state, (Bottom-Left) for the cavity excitation and (Bottom-Right) for the atomic excitation.

Bibliography

[1] D. Jaksch, C. Bruder, J. I. Cirac, C. W. Gardiner, and P. Zoller Phys. Rev. Lett. **81**, 3108 (1998); Markus Greiner, Olaf Mandel, Tilman Esslinger, Theodor W. H., Immanuel Bloch, Nature **415**, 39-44 (2002).

[2] D.G. Angelakis, M. F. Santos, and S. Bose, Phys. Rev. A **76**, 031805(R) (2007).

[3] E. K. Irish, C. D. Ogden, M. S. Kim, Phys. Rev. A **77**, 033801 (2008).

[4] E. K. Irish, Phys. Rev. A **80**, 043825 (2009).

[5] Dirk-Soren Luhmann, Kai Bongs, Klaus Sengstock, and Daniela Pfannkuche, Phys. Rev. A **77**, 023620 (2008).

[6] Qi Zhou and S. Das Sarma, Phys. Rev. A **82**, 041601(R) (2010).

[7] Davide Rossini, Rosario Fazio and Giuseppe Santoro, EPL **83**, 47011 (2008).

[8] A. Osterloh, Luigi Amico, G. Falci, Rosario Fazio, Nature **416**, 608-610 (2002); G. Vidal, J. I. Latorre, E. Rico, and A. Kitaev, Phys. Rev. Lett. **90**, 227902 (2003).

[9] Fernando Guadalupe Santos Lins Brandao, New J. Phys. **7**, 254 (2005).

[10] A. D. Greentree, C. Tahan, J. H. Cole, and L.C.L. Hollenberg, Nat. Phys. **2**, 846 (2006); M. I. Makin, Jared H. Cole, Charles Tahan, Lloyd C. L. Hollenberg, and Andrew D. Greentree, Phys. Rev. A **77**, 053819 (2008); Davide Rossini, Rosario Fazio, Giuseppe Santoro, Europhys. Lett. **83**, 47011 (2008); Jens Koch and Karyn Le Hur, Phys. Rev. A **80**, 023811 (2009); S. Schmidt and G. Blatter Phys. Rev. Lett. **103**, 086403 (2009); Alexander Mering, Michael Fleischhauer, Peter A. Ivanov, and Kilian Singer, Phys. Rev. A **80**, 053821 (2009); James Quach, Melissa I. Makin, Chun-Hsu Su, Andrew D. Greentree, and Lloyd C. L. Hollenberg Phys. Rev. A **80**, 063838 (2009); S. Schmidt and G. Blatter Phys. Rev. Lett. **104**, 216402 (2010).

[11] A. Tomadin, V. Giovannetti, R. Fazio, D. Gerace, I. Carusotto, H.E. Tureci, A. Imamoglu, Phys. Rev. A **81**, 061801(R) (2010)

[12] S. Ferretti, L.C. Andreani, H.E. Tureci, D. Gerace, Phys. Rev. A **82**, 013841 (2010).

[13] Michal Grochol, Phys. Rev. B **79**, 205306 (2009).

[14] Neil Na, Shoko Utsumomiya, Lin Tian, and Yoshihisa Yamamoto, Phys. Rev. A **77**, 031803(R) (2008).

[15] S. Schmidt, D. Gerace, A. A. Houck, G. Blatter, H. E. Tureci, Phys. Rev. B **82**, 100507(R) (2010).

[16] P. A. Ivanov, S. S. Ivanov, N. V. Vitanov, A. Mering, M. Fleischhauer, K. Singer, Phys. Rev. A **80**, 060301(R) (2009).

[17] M. P. A. Fisher, *et.al.*, Phys. Rev. B **40**, 546 (1989); Pinaki Sengupta, Stephan Haas, Phys. Rev. Lett. **99**, 050403 (2007); Ehud Altman, Yariv Kafri, Anatoli Polkovnikov, and Gil Refael, Phys. Rev. Lett. **100**, 170402 (2008).

[18] Long Dang, Massimo Boninsegni, and Lode Pollet, Phys. Rev. B **79**, 214529 (2009).

[19] Ulf Bissbort, Ronny Thomale and Walter Hofstetter, Phys. Rev. A **81**, 063643 (2010).

[20] U. Bissbort and W. Hofstetter, EPL, **86** 50007 (2009).

[21] Michael Knap, Enrico Arrigoni, Wolfgang von der Linden, Phys. Rev. B **81**, 104303 (2010); Peter Pippan, Hans Gerd Evertz, Martin Hohenadler, Phys. Rev. A **80**, 033612 (2009).

[22] A. Peres, Phys. Rev. Lett. **77**, 1413 (1996); G. Vidal and R. F. Werner, Phys. Rev. A **65**, 032314 (2002).

[23] M.X. Huo, Ying Li, Z. Song, C.P. Sun, Phys. Rev. A **77**, 022103 (2008).

[24] H. M. Wiseman and John A. Vaccaro, Phys. Rev. Lett. **87**, 240402 (2001).

[25] Hyunchul Nha and H. J. Carmichael, Phys. Rev. Lett. **93**, 120408 (2004).

[26] Eduardo Mascarenhas, Daniel Cavalcanti, Vlatko Vedral and Marcelo França Santos, Phys. Rev. A 83, 022311 (2011); S. Vogelsberger and D. Spehner, Phys. Rev. A 82, 052327 (2010).

[27] M. C. O. Aguiar, V. Dobrosavljević, E. Abrahams e G. Kotliar, Phys. Rev. Lett. 102, 156402 (2009)

[28] D. Rossini and R. Fazio, Phys. Rev. Lett. **99**, 186401 (2007).

Part II

Equilibrium many-body systems

Chapter 5

The work of quantum phase transitions: Is there Quantum Latency?

5.1 Introduction

Classical phase transitions (CPTs) are driven by a multitude of mechanisms such as particle or heat exchange with a reservoir [1]. A characteristic trait of first order CPTs, e.g. water turning into ice, is an exchange of heat between the system and reservoir at constant temperature called the *latent heat*; this is the energy needed to go from one state of matter to another [2]. This can be made explicit if we consider the free energy $F = U - TS$ which has a discontinuous derivative at the first order critical point. This implies a discontinuity in entropy since $S = -\frac{\partial F}{\partial T}$. Therefore we also have a discontinuity in internal energy which is the latent heat $\Delta U = T\Delta S = Q_{\text{latent}}$.

Quantum phase transitions (QPTs), on the other hand, occur at zero temperature and are driven by changes in the system Hamiltonian, i.e., by extracting or performing work on the system [1]. Here, we recast QPTs in the framework of non-equilibrium thermodynamics [4, 5, 6, 7] and show that the average and irreversible work can be made vanishingly small in the vicinity of a first order QPT, therefore we show that there is no correspondence with classical latency. Thus there is no quantum latent work associated with equilibrium first order quantum phase transitions. However, an actual transition between two phases separated by a first oder transition is forbidden by the hamiltonian dynamics and thus requires the presence of an external bath which allows one phase to be converted into the other. The bath absorbs the excess work as a heat transfer from the system and hence latency is found as a nonequilibrium property.

In this chapter we consider the work done on a quantum system when it is taken across the critical point of a QPT by an infinitesimal-instantaneous change of its Hamiltonian. The sudden quench simplifies our analysis to give a transparent interpretation of the essential physics. Our method relies on quantifying the non-equilibrium work by analyzing the moments of the quantum work distribution. This approach has recently been used to provide insight into both the thermodynamic and universal features of quantum many-body systems [8, 9, 10, 11, 13, 12]. In particular, it was recently shown that for a zero-temperature quantum system undergoing a sudden quench, the

first and second derivatives of the ground state energy with respect to the quench parameter are closely related to the average work and irreversible work respectively [14]. (We also discovered this independently). Building on this result, we show how they capture the non-analyticity of the ground state energy in first order QPTs and to the order parameter and susceptibility of the model in second order QPTs. We support our findings with numerical simulations of the first, second, and infinite order QPTs in the XXZ spin chain, which maps to a model of interacting fermions [15].

5.2   Pure state thermodynamics

We consider a quantum system with the Hamiltonian $\hat{H}(\lambda) = \hat{H}_{\text{free}} + \lambda \hat{V}$, where λ is an external parameter controlling the strength of the perturbing potential $\hat{V}$. For $t < 0$ the control parameter is held at a fixed initial value $\lambda = \lambda_{\text{i}}$ and the system is coupled to a reservoir at zero-temperature. Upon equilibration, the system reaches its ground state, defined by $\hat{H}(\lambda_{\text{i}}) \ket{\psi_0} = E_0(\lambda_{\text{i}}) \ket{\psi_0}$ where $E_0(\lambda_{\text{i}})$ denotes the ground state energy. The control parameter is instantaneously quenched to a final value λ_{f} giving the Hamiltonian $\hat{H}(\lambda_{\text{f}}) = \sum_m E_m(\lambda_{\text{f}}) \ket{\phi_m} \bra{\phi_m}$ where $E_m(\lambda_{\text{f}})$ are the energy eigenvalues of the final Hamiltonian and $\{\ket{\phi_m}\}$ are the corresponding eigenstates.

The work done on the system is defined as the difference between the initial energy of the system and the outcome of an energy measurement performed in the eigenbasis of the final Hamiltonian, i.e., $W_m = E_m(\lambda_{\text{f}}) - E_0(\lambda_{\text{i}})$, where the outcome $E_m(\lambda_{\text{f}})$ is obtained with probability $p_m = |\langle \psi_0 | \phi_m \rangle|^2$. Accordingly, the *quantum work distribution*, which encodes the full statistics of work, is given by [4, 5, 6, 7] $P(W) = \sum_m p_m \, \delta\,(W - W_m)$. The first moment of the work distribution gives the average work done;

$$
\begin{aligned}
\langle W \rangle &= \int W P(W) \mathrm{d}W \\
&= \bra{\psi_0} H(\lambda_{\text{f}}) \ket{\psi_0} - \bra{\psi_0} H(\lambda_{\text{i}}) \ket{\psi_0} \\
&= (\lambda_{\text{f}} - \lambda_{\text{i}}) \bra{\psi_0} \hat{V} \ket{\psi_0} = \delta\lambda \frac{\partial E_0}{\partial \lambda}\bigg|_{\lambda_{\text{i}}},
\end{aligned}
\tag{5.1}
$$

where the last equality follows from $\hat{V} = \partial \hat{H} / \partial \lambda$ and $\delta\lambda = \lambda_{\text{f}} - \lambda_{\text{i}}$.

The average work is bounded from below by the Clausius statement of the second law [27]. At zero temperature, this requires that $\langle W \rangle \geq \Delta U$ with $\Delta U = E_0(\lambda_{\text{f}}) - E_0(\lambda_{\text{i}})$ denoting the change in internal energy. The Clausius inequality is saturated for completely adiabatic evolution. However, for general quenches the system can become excited, thereby dissipating work. This leads to the definition of the irreversible work $\langle W_{\text{irr}} \rangle = \langle W \rangle - \Delta U$ as a measure of the diabaticity of the quench [16]. For a weak quench, $\lambda_{\text{f}} - \lambda_{\text{i}} = \delta\lambda \ll 1$, the irreversible work can be expanded in powers of the small parameter $\delta\lambda$, thus,

$$
\begin{aligned}
\langle W_{\text{irr}} \rangle &= \delta\lambda \frac{\partial E_0}{\partial \lambda}\bigg|_{\lambda_{\text{i}}} - E_0(\lambda_{\text{i}} + \delta\lambda) + E_0(\lambda_{\text{i}}) \\
&\approx -\frac{\delta\lambda^2}{2} \frac{\partial^2 E_0}{\partial \lambda^2}\bigg|_{\lambda_{\text{i}}}.
\end{aligned}
\tag{5.2}
$$

5.3   Universal features of QPTs

Zero temperature quantum systems in the thermodynamic limit undergo a phase transition when a Hamiltonian parameter is tuned through a point of non-analyticity in the derivatives of the ground state energy [1]. For first order QPTs this non-analyticity takes the form of a level crossing, while for second order QPTs the critical point occurs at an avoided crossing (see Fig. 5.1 for a graphical illustration). Owing to this universal behaviour, we need only consider a minimal model incorporating a level crossing and an avoided crossing for our investigation of the thermodynamics of QPTs. We therefore choose the Landau-Zener model, describing a single two level system with energy splitting Δ and coupling ϵ within an externally tunable magnetic field of strength λ. The relevant Hamiltonian is

$$H_{\text{LZ}} = \left(-\frac{\Delta}{2} + a\lambda \right) \sigma^z + \epsilon \sigma^x, \tag{5.3}$$

where σ^α is a spin-1/2 Pauli matrix with $\alpha = \{x, y, z\}$ and a measures the strength of the coupling between the two-level system and the magnetic field. The ground state energy of the Hamiltonian in Eq. (5.3) is easily found to be $E_0 = -\frac{1}{2}\sqrt{4\epsilon^2 + (\Delta - 2a\lambda)^2}$. The first and second derivatives of the ground state energy with respect to the control parameter are then

$$\frac{\partial E_0}{\partial \lambda} = \frac{a(\Delta - 2a\lambda)}{\sqrt{4\epsilon^2 + (\Delta - 2a\lambda)^2}}, \tag{5.4}$$

$$\frac{\partial^2 E_0}{\partial \lambda^2} = -\frac{8a^2\epsilon^2}{(4\epsilon^2 + (\Delta - 2a\lambda)^2)^{3/2}}. \tag{5.5}$$

Hence, combining Eq. (5.4) with Eq. (5.1), we are able to evaluate the average work induced by a sudden quench of the external field in the Landau-Zener model. We approximate an adiabatic change in the external parameter by considering weak sudden quenches, i.e., taking λ_{i} to $\lambda_{\text{f}} = \lambda_{\text{i}} + \delta\lambda$. In the level crossing scenario ($\epsilon = 0$, see Fig. 5.1), analogous to a first order QPT, the average work done per quench is, thus, $\langle W \rangle / \delta\lambda = a$ for $\lambda_{\text{f}} < \lambda_{\text{c}}$ and $\langle W \rangle / \delta\lambda = -a$ for $\lambda_{\text{i}} > \lambda_{\text{c}}$, where $\lambda_{\text{c}} = \Delta/(2a)$ is the critical value of the external field. Evidently, the average work per quench exhibits a discontinuity at the critical point of magnitude

$$w = 2a. \tag{5.6}$$

This discontinuity is a general feature of the level crossing and, therefore, a general feature of first order QPTs. Similar discontinuous behaviour is also exhibited by the classical latent heat in CPTs. This sudden change is not quantum reminiscent of classical latency rather a novel form of nonequilibrium quantum latency.

Physically the average amount of work required to cross the critical point of a first order QPT vanishes with the "size" of the quench $W = \delta\lambda w$. However, as the system is driven across the level crossing it inevitably becomes excited, even for very slow evolution. Hence, to bring the system to its new ground state following the quench, it must be attached to a zero-temperature reservoir. During the equilibration process, an amount of heat is dissipated from the system to the reservoir. The amount of heat transfer is given by the "excess" energy in the system, which is exactly the irreversible contribution to the quantum work [16]. Thus, we have a quantum heat per quench

$$q = \langle w_{\text{irr}} \rangle \tag{5.7}$$

as a universal feature of first order QPTs. However, again $Q = \delta\lambda q$ goes to zero with the size of the quench, thus, there is no heat release intrinsically associated to equilibrium first order quantum phase transitions.

For $\epsilon \neq 0$, the Landau-Zener Hamiltonian in Eq. (5.3) exhibits an avoided crossing, analogous to a second order QPT (see Fig. 5.1). Combining Eq. (5.5) with Eq. (5.2), we are able to evaluate the irreversible work done following a weak sudden quench of the magnetic field strength. For a sudden quench beginning at the critical value of the external parameter $\lambda_{\mathrm{c}} = \Delta/(2a)$, the irreversible work reduces to

$$\langle W_{\mathrm{irr}} \rangle = -\frac{\delta\lambda^2}{2} \left.\frac{\partial^2 E_0(\epsilon \neq 0)}{\partial\lambda^2}\right|_{\lambda=\lambda_{\mathrm{c}}} = \frac{\delta\lambda^2 a^2}{2\epsilon}. \tag{5.8}$$

We see that as $\epsilon \to 0$ in Eq. (5.8), consistent with a second order QPT in the thermodynamic limit, the irreversible work for finite quenches at criticality diverges. This is consistent with the results of Refs. [8, 9, 10, 11, 12, 14] where the irreversible work is shown to indicate second order QPTs. We also point out the similarity between the irreversible work and the fidelity susceptibility, which is also a good indicator of second order QPTs [17, 18, 19, 20] analagous to the thermal susceptibility in a thermally driven second order CPT.

Recalling that low order transitions are associated with non analytical behaviour in derivative of the energy of corresponding order, we have explicitly shown how this thermodynamical approach detects low order transitions. Having elucidated the physical lack of latency in first order QPTs and reiterated the utility of the irreversible work as a susceptibility in second order QPTs, we now proceed to demonstrate these ideas in quantum spin chains.

5.4 Quantum many-body systems

We choose the one-dimensional anisotropic XYZ spin chain as the starting point for our investigation. This model is fully equivalent to a spin-polarized extended Hubbard model at half-filling, describing an effective system of spinless fermions [21, 22]. The Hamiltonian is given by

$$\hat{H} = \sum_{\langle i,j \rangle} \left[J_x \sigma_i^x \sigma_j^x + J_y \sigma_i^y \sigma_j^y + \frac{\lambda}{2} \sigma_i^z \sigma_j^z + h \sigma_i^z \right], \tag{5.9}$$

where $J_{x(y)}$ is the spin coupling along the $X(Y)$-axis, λ is the coupling along the Z-axis and h is the external magnetic field along the Z-axis. For a full discussion of the XYZ model and its mapping to the fermion chain, see Ref. [15].

5.4.1 DMRG: Density matrix renormalization group. Steven R. White Phys. Rev. Lett. 69, 2863 (1992)

Before proceeding with our results it is worthwhile describing, even though briefly, the method we employ for one-dimensional systems: Density Matrix Renormalization Group (DMRG). First of all the method really does not have any group-renormalization property in common with classical renormalization methods, however it does disregard or decimates irrelevant portions of state space based on their probability of occurring. More appropriately, it could be called Density Matrix Decimation but for historical reasons this is not the case. The method is applicable (mainly) for
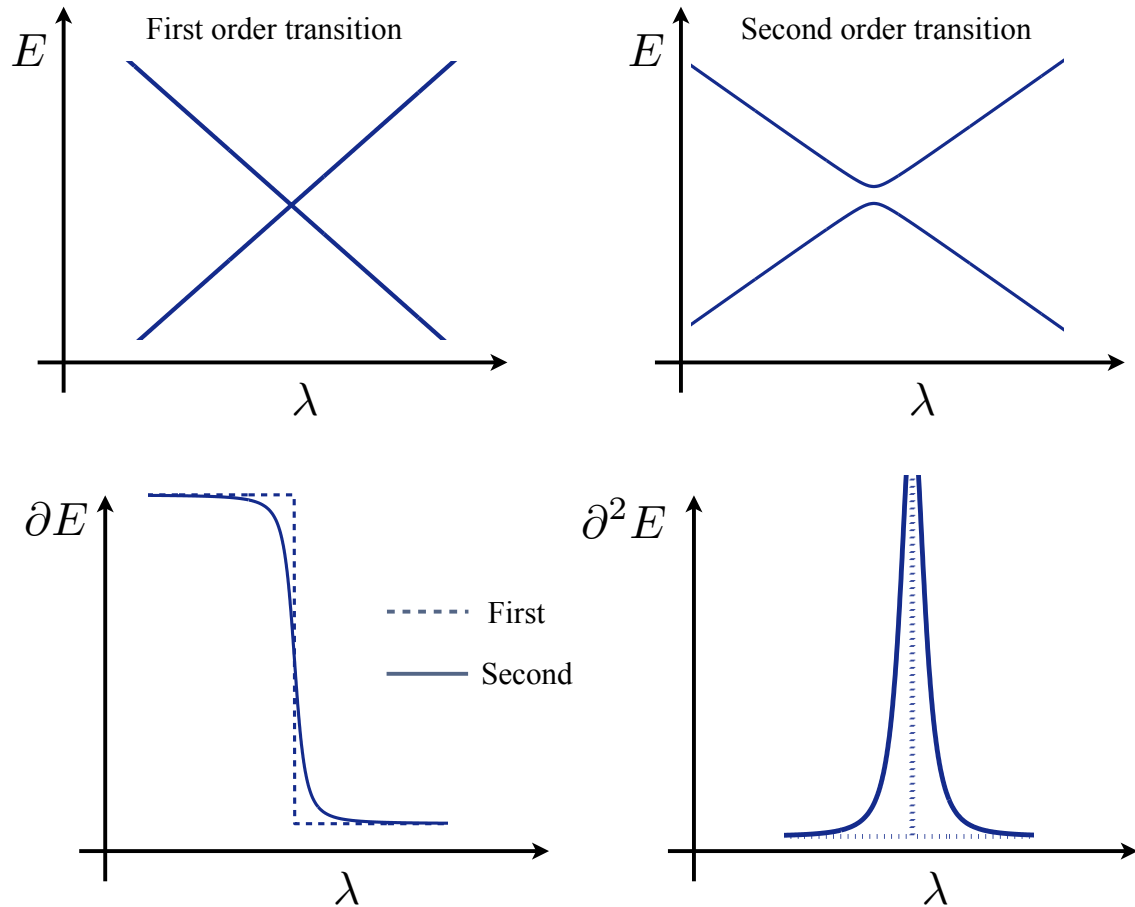
Fig. S.5.1: (Color online.) Schematic representation of a level crossing giving rise to a first order QPT and an avoided crossing leading to a second order QPT as discussed in the main text. The corresponding first and second order derivatives of the ground state energy are also presented. For $\epsilon = 0$, the ground and excited states of the Landau-Zener Hamiltonian (Eq. (5.3)) exhibit a level crossing as the external field is tuned through the critical value $\lambda_c = \Delta/(2a)$, while for $\epsilon \neq 0$, the energy levels exhibit an avoided crossing. In the case of the level crossing, both derivatives are discontinuous. For the avoided crossing, the first and second derivatives are continuous for finite ϵ and become discontinuous in the limit $\epsilon \to 0$ as the turning point in the ground state energy becomes a kink. As an aside, we note that the Landau-Zener Hamiltonian is isomorphous to the Ising mean-field Hamiltonian, which is accurate for the infinitely connected many-body lattice [1].

one-dimensional chains of (small state space) quantum systems of dimension d. In this chapter and the next we use it to describe ground state properties of the many-body Hamiltonian. There are a few reviews (U. Schollwock, Rev. Mod. Phys. 77, 259; G. De Chiara, M. Rizzi, D. Rossini, S. Montangero, J. Comput. Theor. Nanosci. 5, 1277-1288) on the method that should be consulted for a more thorough account and also for the connection to matrix product states (U. Schollwock, Annals of Physics 326, 96).

In order to best present the method we break it into two parts: the *build up* which used to be called infinite-DMRG and the *sweeps*. We start the build up by constructing a system that is small enough to be diagonalized by standard sparse matrix diagonalization, which we represent as a sequence o sites (• • • • • •). The ground state

$$|G\rangle = \sum_i \psi_i |L_i\rangle|R_i\rangle \tag{5.10}$$

, of the Hamiltonian is obtained and then the reduced density matrices corresponding to both halves of the chain are obtained by performing traces on the ground state

$$\rho_L = \mathrm{tr}_R\{|G\rangle\langle G|\} = \sum_i p_i |L_i\rangle\langle L_i|. \tag{5.11}$$

Next, the m most probable eigenstates of the density matrix on each side are stored in a matrix $L = [|L_1\rangle, |L_2\rangle, ..., |L_m\rangle]$ and R (for left and right respectively) with m being determined by the level of accuracy we desire to reach (typically of the order of 100 states). The precision is determined by the total probability of the discarded states and it is usually kept below 10^{-9} such that $1 - \sum_i^m p_i \ll 1$.

Now we perform a "renormalization" operation. We may disregard the least probable states by by projecting all operators of interest onto the subspace spanned by the m most probable states $O \approx R^\dagger O R$. By performing this operation we effectively have reduced the size of the matrices describing $N/2$ sites which would have dimension $d^{N/2}$ to dimension m. After this step we may add two new sites to the middle of the system, and repeat the process of renormalization and site addition until N reaches the desired total number of sites (typically several tens or lower hundreds). Pictorially, we change from the explicit representation (• • • • • •) to (Block$_L$ • •Block$_R$), where we have Blocks of dimension m that may describe systems of dozens of sites. This generates a collection of matrices R_i, L_i and finalises the build up part. At each step we have a renormalized representation of the total state

$$|\psi\rangle = \sum_{ijkl} |BL_i\rangle|s_j\rangle|s_k\rangle|BR_l\rangle. \tag{5.12}$$

Now, the matrices R, L have to be optimised in order to most efficiently project onto the most probable state space. This is done during the sweeps. By using the matrices R, L we may change our representation of the system shifting to the right (and left). For example, we end the build up part in the middle of the chain with (Block$_L$ •$_{N/2}$ •$_{N/2+1}$Block$_R$) and we may shift the representation (without adding any site) to (Block$_L$ •$_{N/2+1}$ •$_{N/2+2}$Block$_R$). This is done by using a small algorithm presented Steven R. White in Phys. Rev. Lett. 77, 3633. While shifting or sweeping to the right only the L matrices should be updated after another diagonalization, and while sweeping to the left only the R matrices should be updated. The sweeping should stop once convergence is reached. Many criteria can be used to determine convergence, throughout this thesis we analyse our criterium in the ground state energy convergence. It is important to note that DMRG effectiveness is directly dependent on the amount and range of the entanglement. It is most effective for slightly entangled states with short range entanglement.

5.4.2 Results

To proceed, we consider the XXZ Hamiltonian ($J_x = J_y = J$) with no external field ($h = 0$). In the parameter regime $\lambda/J < -2$ the ground state is ferromagnetically ordered (a fully-filled band insulator in the Fermi picture). A first order QPT to a Luttinger liquid phase is brought about by tuning λ/J to the regime $|\lambda/J| < 2$. At $\lambda/J = 2$ the system undergoes an infinite order Berezinskii-Kosterlitz-Thouless QPT to an anti-ferromagnetic phase (a charge density wave phase in the fermionic picture). In Fig. 5.2 we show numerical results for the average work and irreversible work done following a series of weak sudden quenches across the phase diagram, passing through both critical points. The work and irreversible work exhibit the discontinuous behaviour predicted in our analysis of the Landau-Zener model. The origin of the discontinuity in the irreversible work, can also be explained phenomenologically in this instance; As the magnetization of the two phases is different, the dynamics induced by quenching the Hamiltonian in Eq. (5.9), which preserves the total magnetization, are not able to convert one phase to the other. To drive the transition, a zero-temperature reservoir must be attached to the system at the end of the quench protocol, bringing the system to its new ground state. Physically, this corresponds to electromagnetic energy exchange between the system and the environment, which is consistent with heat exchange during a cooling process.

For completeness, we mention that neither the work nor the irreversible work indicate the Berezinskii-Kosterlitz-Thouless transition at $\lambda/J = 2$ (see Fig. 5.2). This is expected since the Berezinskii-Kosterlitz-Thouless transition is of infinite order and is, therefore, not captured by the finite order non-equilibrium thermodynamical approach we adopt here.

We now turn our attention to second order QPTs. In Fig. 5.3, we plot the numerically exact results for the average work and irreversible work done by quenching the external field in the XX model ($\lambda = 0$ and $J_x = J_y = J$ in Eq. (5.9)). We see that the average work has a discontinuous derivative at the QPT and, thus, the irreversible work shows singular behaviour at the critical point, consistent with its interpretation as a susceptibility. The thermodynamic properties of the second order QPT in the transverse Ising model ($\lambda = J_y = 0$ and $J_x = J$ in Eq. (5.9)) have been extensively studied [8, 9, 10, 11, 12, 14] and shown to exhibit the same global features in the phase diagram. We also note that, in these specific cases, the average work $\langle W \rangle = \delta h \sum_i \langle \sigma_i^z \rangle$ is given by the order parameter of the model.

5.5 Conclusion

In this chapter we have analysed the statistics of work done on general classes of quantum critical models by infinitesimal sudden quenches of a control parameter. We show that first order QPTs exhibit a discontinuity in the work distribution similar but not analogous to the classical latent heat, such that quantum latency is intrinsically a nonequilibrium phenomenon. As a final remark, we point out that recent proposals to measure the statistics of work by means of an ancillary system [23, 24] (see also [25] for an extension to open systems) can be extended to the many-body domain [26] and used to verify our findings, hence bringing pure state thermodynamics into the laboratory.
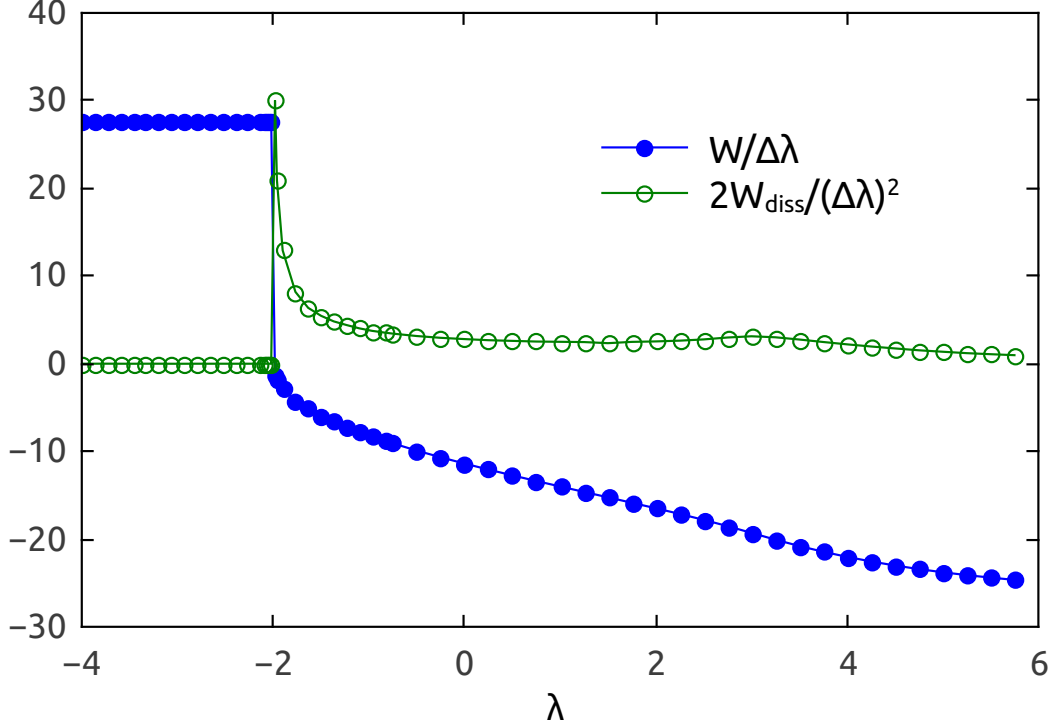
Fig. S.5.2: (Color online.) Density matrix renormalization group (DMRG) data (in units of $J = 1$) for the average work (filled blue circles) and irreversible work (empty green circles) done in a weak sudden quench of the XXZ hamiltonian with 112 sites and $\delta\lambda = 10^{-5}$. Here, we assume the presence of a small local energy shift at one lattice site which lifts the degeneracy in the ground state of the Hamiltonian. The data has a DMRG truncation error and energy convergence of $\approx 10^{-9}$. The quench protocol we consider is an instantaneous change of the Z-coupling $\delta\lambda = \lambda_{\mathrm{f}} - \lambda_{\mathrm{i}} \ll 1$ with the system initialized in the ground state of the initial Hamiltonian. Both the average and irreversible work display a discontinuity at the critical point of the first order transition at $\lambda = -2$. On the left hand side of the first order transition, the gapped spectrum of the ferromagnetic phase enforces adiabaticity as the system cannot be taken out of equilibrium by weak quenches within the same phase. This means that the system is not excited by the quench and the sole contribution to the average work is the change in internal energy. The discontinuities at the critical point indicate work required to drive the system from the ferromagnetic phase to the Luttinger liquid phase. The new phase is characterized by a continuous energy spectrum and so subsequent quenches can excite the system, leading to the dissipation of work. In contrast, neither the average work nor the irreversible work indicate the Berezinskii-Kosterlitz-Thouless transition at $\lambda = 2$.
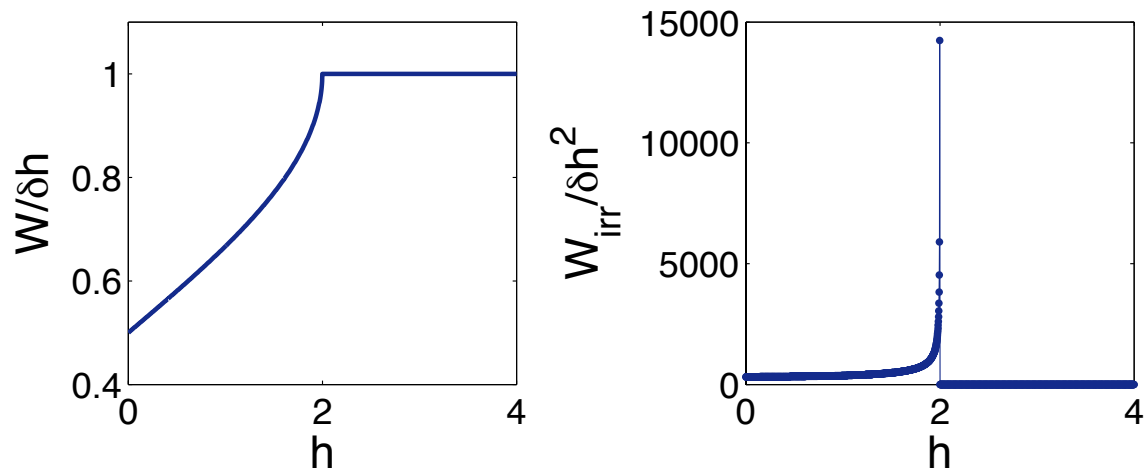
Fig. S.5.3: (Color online.) Exact numerical results for the average work and irreversible work induced by a sudden quench of the external magnetic field h in the XX model. This model incorporates a second order QPT from a ferromagnetic phase for $h/J \ll 1$ to a paramagnetic phase for $h/J \gg 1$, with the critical point occurring when the external field is two times the internal coupling $h = 2J$. The phase diagram exhibits a discontinuity in the average work and a divergent irreversible work at the critical point. This behaviour reflects the relationship between the irreversible work and fidelity susceptibility discussed in the main text.

Bibliography

[1] H.B. Callen, *Thermodynamics and an Introduction to Thermostatistics*, (Wiley, New Jersey, 1985).

[2] K. Binder, *Theory of first-order phase transitions*, *Rep. Prog. Phys.* **50**, 783-859 (1987).

[3] S. Sachdev, *Quantum Phase Transitions*, (Cambridge University Press, UK, 1999).

[4] H. Tasaki, *Jarzynski Relations for Quantum Systems and Some Applications*, arXiv.org:cond-mat/0009244 (2000).

[5] J. Kurchan, *A Quantum Fluctuation Theorem*, arXiv.org:cond-mat/0007360v2 (2000).

[6] S. Mukamel, *Quantum Extension of the Jarzynski Relation: Analogy with Stochastic Dephasing*, Phys. Rev. Lett. **90**, 170604 (2003).

[7] P. Talkner, E. Lutz and P. Hänggi, *Fluctuation theorems: Work is not an observable*, Phys. Rev. E **75**, 050102R (2007).

[8] A. Silva, *Statistics of the Work Done on a Quantum Critical System by Quenching a Control Parameter*, *Phys. Rev. Lett.* **101**, 120603 (2008).

[9] F.N.C. Paraan and A. Silva, *Quantum quenches in the Dicke model: Statistics of the work done and of other observables*, *Phys. Rev. E* **80**, 061130 (2009).

[10] A. Gambassi and A. Silva, *Large Deviations and Universality in Quantum Quenches*, Phys. Rev. Lett. **109**, 250602 (2012).

[11] R. Dorner, J. Goold, C. Cormick, M. Paternostro and V. Vedral, *Emergent Thermodynamics in a Quenched Quantum Many-Body System*, Phys. Rev. Lett., **109**, 160601 (2012).

[12] P. Smacchia and A. Silva, *Universal Energy Distribution of Quasiparticles Emitted in a Local Time-Dependent Quench*, Phys. Rev. Lett. **109**, 037202 (2012).

[13] B. Dora, A. Bacsi, and G. Zarand, *Generalized Gibbs ensemble and work statistics of a quenched Luttinger liquid*, Phys. Rev. B **86**, 161109(R) (2012).

[14] S. Sotiriadis, A. Gambassi and A. Silva, *Statistics of the work done by splitting a one-dimensional quasicondensate*, Phys. Rev. E **87**, 052129 (2013).

[15] T. Giamarchi, *Quantum Physics in one Dimension*, (Oxford University Press, UK, 2003).

[16] S. Deffner and E. Lutz, *Generalized Clausius Inequality for Nonequilibrium Quantum Processes*, *Phys. Rev. Lett.* **105**, 170402 (2010).

[17] P. Buonsante and A. Vezzani, *Ground-State Fidelity and Bipartite Entanglement in the Bose-Hubbard Model*, *Phys. Rev. Lett.* **98**, 110601 (2007).

[18] P. Zanardi, H.T. Quan, X. Wang, and C.P. Sun, *Mixed-state fidelity and quantum criticality at finite temperature*, *Phys. Rev. A* **75**, 032109 (2007).

[19] S. Chen, L. Wang, Y. Hao, and Y. Wang, *Intrinsic relation between ground-state fidelity and the characterisation of a quantum phase transition*, *Phys. Rev. A* **77**, 032111 (2008).

[20] S-J Gu, *Fidelity approach to quantum phase transitions*, *Int. J. Mod. Phys. B* **24**, 4371 (2010).

[21] T. Mishra, J. Carrasquilla and M. Rigol, *Phase diagram of the half-filled one-dimensional t-V-V' model*, *Phys. Rev. B* **84**, 115135 (2011).

[22] R.G. Pereira, S.R. White and I. Affleck, *Spectral function of spinless fermions on a one-dimensional lattice*, *Phys. Rev. B* **79**, 165113 (2009).

[23] R. Dorner, S. R. Clark, L. Heaney, R. Fazio, J. Goold, and V. Vedral, *Extracting Quantum Work Statistics and Fluctuation Theorems by Single-Qubit Interferometry*, Phys. Rev. Lett. **110**, 230601 (2013).

[24] L. Mazzola, G. De Chiara, and M. Paternostro, *Measuring the Characteristic Function of the Work Distribution*, Phys. Rev. Lett. **110**, 230602 (2013).

[25] M. Campisi, R. Blattmann, S. Kohler, D. Zueco, P. Hänggi, *Employing Circuit QED to Measure Nonequilibrium Work Fluctuations*, arXiv:1307.2371v1 (2013).

[26] J. Goold, T. Fogarty, N. LoGullo, M. Paternostro, and T. Busch, *Orthogonality catastrophe as a consequence of qubit embedding in an ultracold Fermi gas*, Phys. Rev. A **84**, 063632 (2011).

[27] M. Campisi, P. Hänggi and P. Talkner, *Colloquium: Quantum fluctuation relations: Foundations and applications*, *Rev. Mod. Phys.* **83**, 771 (2011).

Chapter 6

Non-universality of entanglement convertibility

Recently, it has been suggested that operational properties connected to quantum computation can be alternative indicators of quantum phase transitions. In this chapter we systematically study these operational properties in 1D systems that present phase transitions of different orders. For this purpose, we evaluate the local convertibility between bipartite ground states. Our results suggest that the operational properties, related to non-analyticities of the entanglement spectrum, are good detectors of explicit or hidden symmetries of the model, but not necessarily of phase transitions. We also show that thermodynamically equivalent phases, such as Luttinger liquids, may display different convertibility properties depending on the underlying microscopic model.

6.1   Introduction

Low order phase transitions are directly related to singularities in the derivatives of the free energy, with such singularities marking the boundary between two macroscopically distinguishable phases. These transitions are usually described by Landau's paradigm of symmetry breaking and as such are detectable by local order parameters [1]. The singular behaviour not only manifests itself in thermodynamical properties, but also has dynamical consequences, for instance the critical slowing down of adiabatic time evolution [2, 3]. On the other hand, the existence of phase transitions that do not correspond to symmetry breaking is well established [4]. A simple example is provided by the infinite-order Berezinskii-Kosterlitz-Thouless (BKT) transition [5] realized in several two-dimensional systems at finite temperature, a recent example being cold atomic gases [6]. The BKT universality class also turns up in quantum phase transitions in one-dimensional (1D) systems such as spin chains [7] and Bose-Hubbard chains realizable in optical lattices [8]. The existence of such transitions and the growing interest in topological phases in general [9, 10, 11, 12, 13, 14], which cannot be described by local order parameters, have motivated alternative approaches to address quantum phase transitions [15, 16, 17].

Quantum information theory has provided novel perspectives in this context based, for example, on the analysis of the intrinsic correlations (entanglement entropy, entanglement spectrum) of the quantum states of a given system [18, 20, 21, 22, 19, 23, 24, 25, 26, 27, 28, 29, 30, 31]. More recently,

a few studies have analysed the so-called local convertibility of quantum states [32, 33, 34, 10], which introduces an operational view related to quantum computation. This quantity is completely characterized by functions of the entanglement spectrum, either through majorization relations or the Rènyi entropies [35, 36, 37, 38]. Remarkably, it has been shown that several phase transitions coincide with changes in the local convertibility [32, 33, 34].

In this chapter we analyse operational aspects of quantum systems using the density matrix renormalization group (DMRG) technique. More concretely, we investigate the behaviour of the local convertibility across several quantum phase transitions in one-dimensional spin-1/2 and spin-1 XXZ Hamiltonians. Our results show that changes of the local convertibility typically correspond to points of symmetric Hamiltonians, which may not coincide with quantum phase transitions. We also give an example of an infinite-order (BKT) transition that is detached from *any* pre-existing symmetries, corresponding to *no* changes in the convertibility profile. Thus, according to our results the operational approach based on convertibility is a good detector of explicit symmetries rather than criticality. More specifically, we note that the notion of convertibility we adopt assumes a protocol of local operations and we show that this notion indicates explicit symmetries whose generators are local operators (i.e. operators that are sums but never products of single-site operators). However, hidden symmetries whose generators are non local operators are not directly detected by the convertibility, but through other properties of the entanglement spectrum.

6.2 Local Convertibility

Consider a quantum system described by a Hamiltonian H_λ, where λ is some tunable parameter. The system is partitioned into two subsystems, which are distributed to parties A and B. The two parties are given the task of converting the ground state $|\Psi_0^{(\lambda)}\rangle_{AB}$ of the initial Hamiltonian into $|\Psi_0^{(\lambda+\epsilon)}\rangle_{AB}$, the ground state of $H_{\lambda+\epsilon}$, by performing only local operations and classical communication (LOCC) on their respective subsystems. The general protocol allows for the use of an extra resource, namely a shared ancillary entangled state called catalyst $|C\rangle$, with which they can freely operate, provided that $|C\rangle$ is left undisturbed in the end of the process, i.e. $|\Psi_0^{(\lambda)}\rangle |C\rangle \rightarrow |\Psi_0^{(\lambda+\epsilon)}\rangle |C\rangle$. This protocol is called local catalytic conversion [36, 37, 38].

The necessary and sufficient condition for catalytic conversion relies on the set of Rènyi entropies,

$$S_\alpha(\lambda) = \frac{1}{1-\alpha} \log \, \mathrm{Tr}[\rho_A^\alpha(\lambda)] = \frac{\log \sum_i [\xi_i(\lambda)]^\alpha}{1-\alpha}, \tag{6.1}$$

where $\rho_A(\lambda)$ is the reduced density matrix of subsystem A and $\xi_i(\lambda)$ are its eigenvalues which constitute the entanglement spectrum (ES) of the bipartition [23]. Note that S_0 is the logarithm of the rank of the state, i.e., the number of nonzero eigenvalues of the reduced density matrix, and $S_{\alpha \rightarrow 1}$ is the von Neumann entropy or entanglement entropy (EE), while $S_{\alpha \rightarrow \infty}$ is the logarithm of the largest eigenvalue. The condition for conversion is $S_\alpha(\lambda) \geq S_\alpha(\lambda+\epsilon)$ for all α [37, 38], i.e., no entropies can increase after the conversion. In the $\epsilon \rightarrow 0$ limit, this relation can be replaced by the analysis of the signs of the catalytic susceptibility $\chi(\alpha,\lambda) = \frac{\partial S_\alpha(\lambda)}{\partial \lambda}$. If $\chi < 0$ for all α, then conversion is only possible from λ to $\lambda+\epsilon$; if $\chi > 0$, $\forall \alpha$, then conversion is possible only in the opposite direction. For $\chi = 0$ conversion is possible in both directions. This criterium was used in [32] to analyse the power of adiabatic quantum computation in different phases of a given λ-parametrized Hamiltonian.

However, some states allow for local convertibility even in the absence of a catalyst. In this case one can use the criterium of majorization of quantum states, defined as [35]

$$M(j) = \frac{\partial}{\partial \lambda} \sum_{i=1}^{j} \xi_i(\lambda), \tag{6.2}$$

where the entanglement spectrum is sorted in decreasing order. Convertibility from $|\Psi_0^{(\lambda)}\rangle$ to $|\Psi_0^{(\lambda+\epsilon)}\rangle$ in the absence of the catalyst is possible if $M(j) \geq 0$ for all j.

6.3 Anisotropic spin chain models

We consider the XXZ Hamiltonian

$$H = \sum_{l=1}^{N} [S_l^x S_{l+1}^x + S_l^y S_{l+1}^y + \Delta S_l^z S_{l+1}^z + D(S_l^z)^2], \tag{6.3}$$

where $\mathbf{S}_l^{(x,y,z)}$ are the spin operators at the lth site, Δ is the longitudinal nearest-neighbor exchange interaction, and D represents uniaxial single-ion anisotropy. In eq. 6.3 and through out this paper, we assume the transverse nearest-neighbor exchange interaction as the unit of energy. We study both spin-1/2 and spin-1 systems; for the former the single-ion anisotropy term is simply a constant, since $\sigma_z^2 = 1$ (where σ_z is a Pauli matrix). We shall identify the control parameter λ with either Δ or D, depending on the transition in question. For any values of Δ and D, the model has an explicit U(1) rotational symmetry in the xy plane and a Z_2 spin inversion symmetry along the z axis.

The spin-1/2 model is integrable and exactly solvable by Bethe ansatz [7]. The system has two gapped phases: a ferromagnetic phase for $\Delta < -1$ and an antiferromagnetic (AFM) Néel phase for $\Delta > 1$, separated by a gapless Luttinger liquid (LL) XY phase for $-1 < \Delta \leq 1$. The phase transition between the ferromagnetic and LL phases is of first order, while the one between LL and AFM phases is a BKT transition. In the latter the gap decreases exponentially as $\Delta \to 1^+$, which poses a challenge for numerical techniques attempting to detect the critical point [39, 27]. The model has an explicit SU(2) symmetry at $\Delta = 1$ (both in the spin-1/2 and spin-1 cases), that is, there exists a set of four operators $Z = \sum_l S_l^z$ (the total Z-spin), S^2 (the total spin), $Q = \sum_l S_l^- = \sum_l S_l^x - iS_l^y$ (a lowering operator) and $Q^\dagger$ which commute with the Hamiltonian at $\Delta = 1$ and are constructed as sums over local operators.

The spin-1 model is not integrable, but its ground state phase diagram is known [40, 41]. Let us first focus on the $D = 0$ line. In this case one finds a ferromagnetic phase for $\Delta \leq -1$, a LL XY phase for $-1 < \Delta \leq 0$, a Haldane phase for $0 < \Delta \lesssim 1.18$ and a Néel phase for $\Delta \gtrsim 1.18$ [42, 43]. The gapped Haldane phase is characterized by a nonlocal string order parameter that breaks a hidden $Z_2 \times Z_2$ symmetry [44] and is an example of a symmetry protected topological phase [12]. Most interestingly, the transition between the XY and the Haldane phase is of BKT type and is known to occur exactly at $\Delta = 0$ due to a hidden SU(2) symmetry generated by nonlocal operators [45]. To be more specific, in this case the Q operators that define the algebra satisfy $Q^+ \propto \sum_j (S_j^+)^2 e^{i\pi \sum_{l<j} S_l^z}$, $Q^- \propto \sum_j (S_j^-)^2 e^{i\pi \sum_{l<j} S_l^z}$ and $Q^z \propto [Q^+, Q^-]$, that is, they involve sums over nonlocal operators, in contrast to the case of the explicit SU(2) symmetry present at $\Delta = 1$.
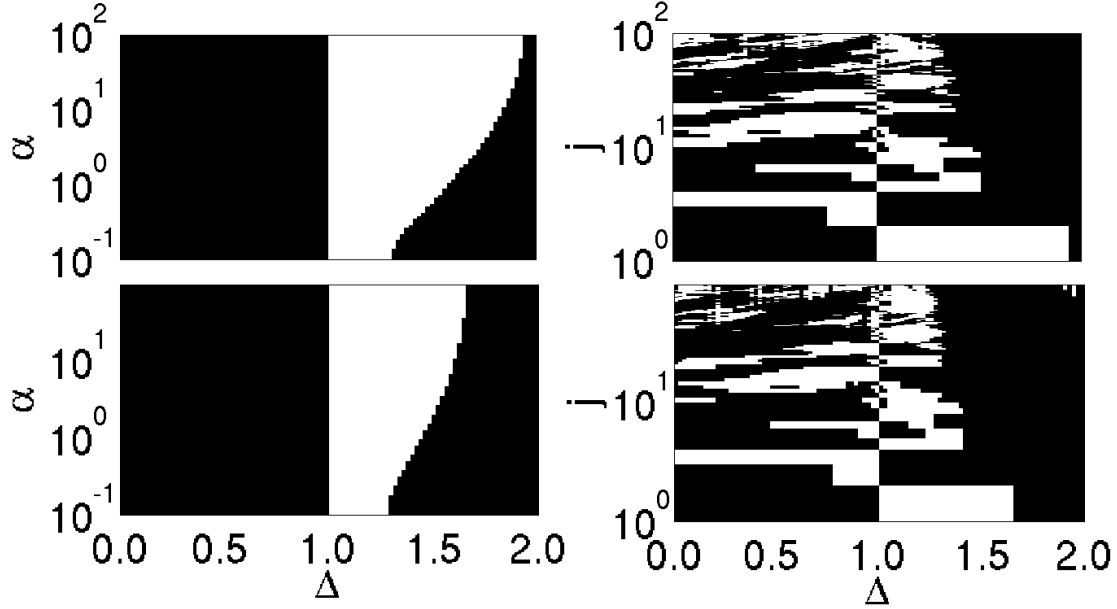
Fig. S.6.1: The sign of the catalytic susceptibility χ for different Rènyi entropies (left panels) and majorization M (right panels) as a function of Δ for a spin-1/2 chain with $N = 112$ (top) and $N = 212$ (bottom), where N is the size of the chain. The black region indicates $\chi < 0$ (or $M < 0$) and the white region corresponds to $\chi > 0$ (or $M > 0$). The data was generated for a symmetrical bipartite system $A = B = L/2$, with a DMRG truncation error below 10^{-9}.

Switching on the single-ion anisotropy in the spin-1 model gives rise to a BKT transition line in the phase diagram [42]. While the transition between XY and Haldane remains pinned at $\Delta = 0$ due to the hidden SU(2) symmetry, there appears a BKT transition between the XY phase and a so-called large-D phase, favoured by strong easy-plane anisotropy ($D > 0$). The gapped large-D phase is topologically trivial as the nondegenerate ground state is adiabatically connected to the product state with $S_l^z = 0$ for all spins. The transition from XY to large D is completely dissociated from high symmetry points in the lattice model. It is important to distinguish between the exact SU(2) symmetry at $\Delta = 0$ [45] and the SU(2) symmetry that arises in the renormalization group analysis of the sine-Gordon model, which is the effective field theory for the BKT transition [47, 46]. This emergent symmetry is a genuine signature of a quantum phase transition since it becomes asymptotically exact in the thermodynamic limit.

6.4 Operational properties

For both spin-1/2 and spin-1 models, the ground state is always one of the two degenerate fully polarized states for any $\Delta \leq -1$. Thus, in the ferromagnetic phase $\chi = 0$ and convertibility is possible between any two points (in both directions).

The other phases have nontrivial convertibility behaviour. First consider the spin-1/2 model.

In the left panels of Fig. 6.1 we present the sign of the catalytic susceptibility obtained using DMRG for open chains with $N = 112$ sites (top panel) and $N = 212$ (bottom panel). Differently from the ferromagnetic phase, for $-1 < \Delta < 1$ (which corresponds to the critical LL phase in the thermodynamic limit), $\chi < 0$ for all α, which indicates unidirectional convertibility. In addition, the convertibility changes direction at the isotropic point $\Delta = 1$. The convertibility is then lost (i.e., the sign of χ depends on α) as Δ increases and it is recovered (unidirectionally) for larger Δ as the ground state approaches the classical Néel state. The convertibility is sensitive to the chain length: the larger the system, the smaller the value of Δ for which it presents the convertibility characteristic of strong AFM behaviour.

Results for the majorization analysis are shown in the right panels of Fig. 6.1 for both $N = 112$ and $N = 212$, from which we can see that the use of a catalyst in the conversion is dispensable only in the strong AFM regime.

We stress that, independently of the chain length, the catalytic convertibility changes direction exactly at the Heisenberg point $\Delta = 1$ (see Fig. 6.1), which coincides with the SU(2) symmetry of the model. The absence of finite size effects at this point, even for small chains with $N \sim 10$ sites, suggests that the convertibility is detecting the SU(2) symmetry (expected to be present for chains of *any* size), rather than the phase transition, whose precursors should be apparent only for large systems. It is also interesting that the majorization relations (also in Fig. 6.1) display a local mirror-like symmetry around $\Delta = 1$, which reinforces that these quantities detect the SU(2) symmetry.

Let us now discuss the $D = 0$ spin-1 model. Our results for the convertibility properties in this case are presented in the top panel of Fig. 6.2. Interestingly, the LL phase $(-1 < \Delta < 0)$ is not locally convertible, since the sign of χ depends on α, unlike the LL phase in the spin-1/2 model, which is convertible. This is a remarkable fact: even though the LL phases of spin-1/2 and spin-1 models share the same low-energy physics, they exhibit different operational behaviour. Nevertheless, we note that the catalytic susceptibilities corresponding to large values of α, which are dominated by the largest eigenvalues of the density matrix, have the same sign $(\chi < 0)$ for both spin-1/2 and spin-1 LL phases. This seems consistent with the general expectation that universal information can be extracted from the low-lying levels in the ES [23, 25]. In contrast, the low-α (i.e., "high temperature" [23]) susceptibilities may depend on details of the microscopic model.

Now, the transition from the LL to the Haldane phase (known to occur at $\Delta = 0$ in the thermodynamic limit) does not coincide with a change in the convertibility (see Fig. 6.2). At this point the Hamiltonian presents the hidden SU(2) symmetry (related to *nonlocal* operators) discussed previously in this paper. This *hidden* symmetry is not detected by the *local* convertibility. Nonetheless, it is important to stress that the EE $(S_{\alpha \to 1})$ does present a derivative that changes sign exactly at the symmetry point, which also coincides with a level crossing in the ES (bottom of the figure). For $\alpha < 1$, the susceptibilities change sign for $\Delta < 0$, while for $\alpha > 1$ the sign changes happen for $\Delta > 0$. Thus, even though the convertibility is blind to this hidden symmetry, it is still encoded in the ES.

Figure 6.2 (top) also shows changes in the convertibility profile within the Haldane phase. The unidirectional convertibility is established approximately once the phase is reached $(0 \lesssim \Delta \lesssim 0.5)$, but it is then lost for $0.5 \lesssim \Delta \lesssim 0.7$. As Δ increases even further, still in the Haldane phase, the convertibility is recovered in the opposite direction. More interestingly, χ changes sign for all α exactly at the SU(2) symmetry point $\Delta = 1$. We emphasize that all these alterations happen inside the same phase, leading us to conclude that changes in the local convertibility do not necessarily correspond to phase transitions. Furthermore, there seems to be a direct relation between local
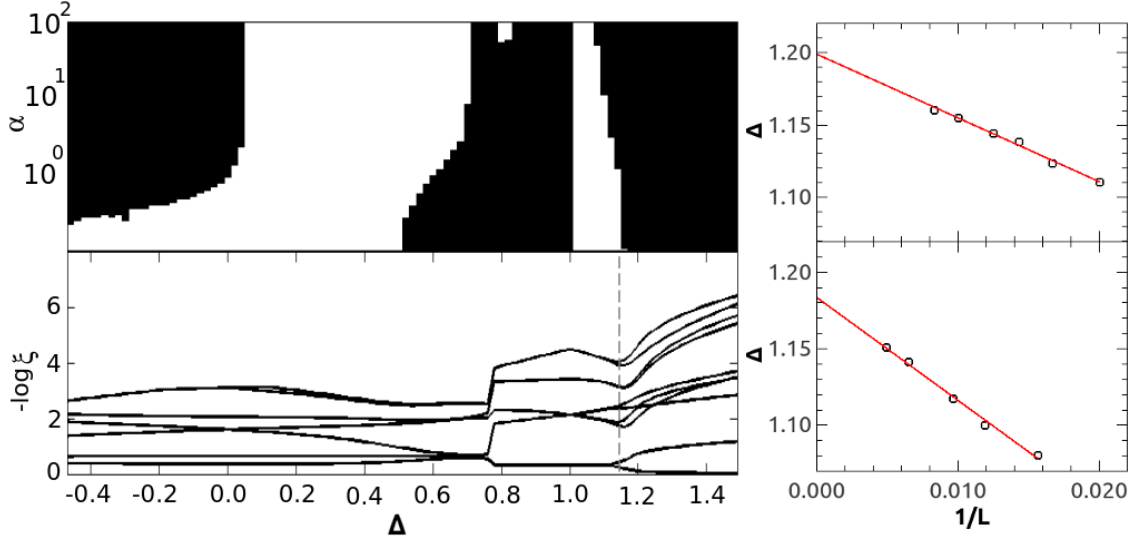
Fig. S.6.2: Sign of the catalytic susceptibility for different Rènyi entropies (left-top) and entanglement spectrum (left-bottom) of a symmetrical bipartite $A = B = L/2$ spin-1 system as a function of Δ, for $D = 0$ and $N = 106$. The right panels show finite size scaling procedures corresponding to the point where the unidirectional convertibility is recovered (top) and the level degeneracies are lifted (bottom) when going from the Haldane phase to the Néel phase.

convertibility and symmetries related to local operators.

The convertibility profile is a function of the ES. The 10 largest eigenvalues of the reduced density matrix are presented in the bottom panel of Fig. 6.2. As we can see, the most abrupt changes in the convertibility properties occur in the vicinity of points of either level crossing (e.g. near $\Delta = 1$) or degeneracy breaking of the ES (e.g. near $\Delta \approx 1.18$), that is, are related to non-analyticities of the ES.

It is interesting to understand why there are level crossings at $\Delta = 0$ and $\Delta = 1$, which correspond to the SU(2) symmetry points. The system ground state is an eigenvector of the symmetry operators and the partition we consider does not break the symmetry. This means that the left and right eigenvectors of the Schmidt decomposition can be identified by the symmetry quantum numbers. For the SU(2) symmetry, energy-eigenvectors corresponding to different eigenvalues of S_z can be degenerated if they are connected by the S^+ or S^- operators defined at each partition. This gives rise to the level crossings we observe in Fig. 6.2. As these crossings are associated with the symmetry, which is present for systems of any size, we do not expect these crossings to shift with the system size, as indeed observed in our numerical results (not shown). We add that the connection between symmetry and degeneracy in the EE has been analysed in detail in other cases [48].

A second order (Ising type) phase transition from the Haldane to the Néel phase happens for $\Delta \approx 1.18$ (in the thermodynamic limit) [42, 43]. As can be seen in the left-top panel of Fig. 6.2, around this value of Δ we observe a change in the convertibility sign. Contrary to the cases we analyse above, here the convertibility profile *is* sensitive to finite size effects. Note that this phase

transition falls under the standard symmetry breaking paradigm and, if the convertibility is able to detect the transition, it should depend on the system size, as it indeed does.

In previous literature [32, 34], changes in the convertibility profile are associated to this symmetry breaking type of transition, but only small systems are analysed (up to 18 sites). Here we consider larger systems and perform a finite-size scaling analysis, which can be seen at the right-top panel of Fig. 6.2. In the thermodynamic limit, the critical Δ obtained from our scaling procedure is $\Delta \approx 1.20$, which slightly deviates from the known value of $\Delta \approx 1.18$. Indeed, we do not expect a very good estimation of the critical Δ from the convertibility, since the changes in its profile correspond to Rènyi entropies of small-α that strongly depend on the smallest reduced density matrix eigenvalues, which intrinsically have less accuracy in the DMRG calculation.

The largest eigenvalues of the reduced density matrix are numerically more precise and indeed the 10 largest values of them can be used to better determine where this Ising type of transition happens. The change in the convertibility analysed above corresponds to a level splitting in the ES - see the dashed line in the left-bottom panel of the figure. This degeneracy breaking can be associated with the Haldane-Néel phase transition since for open chains the higher degeneracy of the Haldane phase is attributed to the spontaneous breaking of the hidden $Z_2 \times Z_2$ symmetry [24]. The value of Δ where this degeneracy is lift also *shifts* with the system size and a finite size scaling allows us to obtain the corresponding value in the thermodynamic limit. As can be seen in the right-bottom panel of Fig. 6.2, our analysis yields $\Delta \approx 1.18$, in good agreement with the known critical value for the Haldane-Néel phase transition [42, 43].

We are thus able to correctly identify the transition point by analyzing the ES, which is directly related to the convertibility profile. This result and the previous literature suggest that the convertibility is a detector of criticality only in the case of transitions associated with symmetry breaking. In most of the cases, however, it is a detector of explicit symmetries of the Hamiltonian.

Regarding the majorization relations, our results for the spin-1 system indicate that convertibility without a catalyst is possible only in the strong AFM (large Δ) regime, similarly to the Néel phase of the spin-1/2 model.

6.4.1 Single-ion anisotropy

To strengthen the conclusion drawn above that the convertibility is a detector of symmetries instead of phases transitions, we study the spin-1 XXZ chain with single-ion anisotropy. As mentioned above, the phase diagram for $\Delta < 0$ and $D > 0$ contains a BKT transition (without symmetry breaking) from a critical XY phase to a gapped large-D phase [41]. This transition does not coincide with any high symmetry points in the Hamiltonian for finite chains. In Fig. 6.3, we show results for some Rènyi entropies as a function of positive D, for $\Delta = -0.5$. The main point is that all entropies decrease monotonically with D, leading to a uniform convertibility profile ($\chi < 0$ for all α and all D). The BKT transition is expected to happen at $D \approx 0.8$ for $\Delta = -0.5$ [41], but there is no sign of it in the convertibility profile. We stress that this is the first example (to our knowledge) of a phase transition around which there is absolutely no change in the convertibility.

6.5   Critical Entanglement entropy

The phase transition analysed in the last section constitutes an important example in the context of our work, since it is not accompanied by a change in the convertibility. This infinite order phase transition which does not have a pre-existing SU(2) symmetry has, however, a small amount of
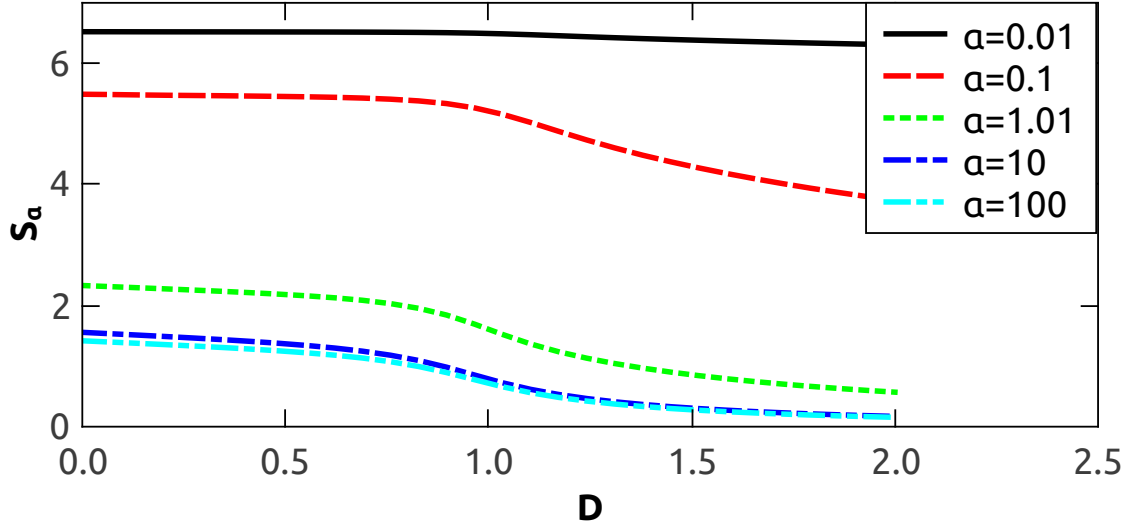
Fig. S.6.3: (color online). Rènyi entropies S_α ($\alpha = 0.01; 0.1; 1.01; 10$ and 100) for a $N = 206$, spin-1 chain with fixed $\Delta = -0.5$ and $A = B = L/2$, as a function of D. The entropies are always monotonic, which means that there is no change in the direction of the convertibility.

work dedicated to it. Here we show that the EE $S_{\alpha \to 1}$ can be used to detect it through a simple finite size analysis.

In Fig. 6.4 we show the EE, $S(x)$, as a function of the partition size x for $N = 106$, $\Delta = -0.5$ and different values of the single-ion anisotropy D. It is clear that the behaviour of $S(x)$ qualitatively changes with D: it increases logarithmically with x for small D, but saturates for large D values, indicating a phase transition.

In fact, the EE is specially useful since it has been shown to exhibit universal scaling in the LL phase, which is described by a conformal field theory (CFT) with central charge $c = 1$. Using CFT, Calabrese and Cardy [49] showed that the EE of a finite system with open boundary conditions in the regime $x, N \gg 1$ is given by

$$S(x, N) = \frac{c}{6} \log \left[\frac{2N}{\pi} \sin \left(\frac{\pi x}{N} \right) \right] + s', \tag{6.4}$$

where s' is a non universal constant.

We can find the BKT critical point by fitting the numerical data to Eq. 6.4, leaving c and s' as free parameters, as shown in Fig. 6.4. For small D, the numerical data are well fitted by Eq. (6.4), indicating that the system is in the critical phase. As D increases, however, the behaviour of $S(x)$ starts to deviate from the CFT prediction. The fitting accuracy (inset of the figure) clearly shows that Eq. (6.4) correctly describes the EE for $D \lesssim 0.8$, leading us to estimate that the BKT critical point is at $D = 0.82 \pm 0.07$, in accordance with previous results [41]. Inside the critical region, the values of the free parameters are as expected: s' is independent of the chain length and $c \approx 1$.
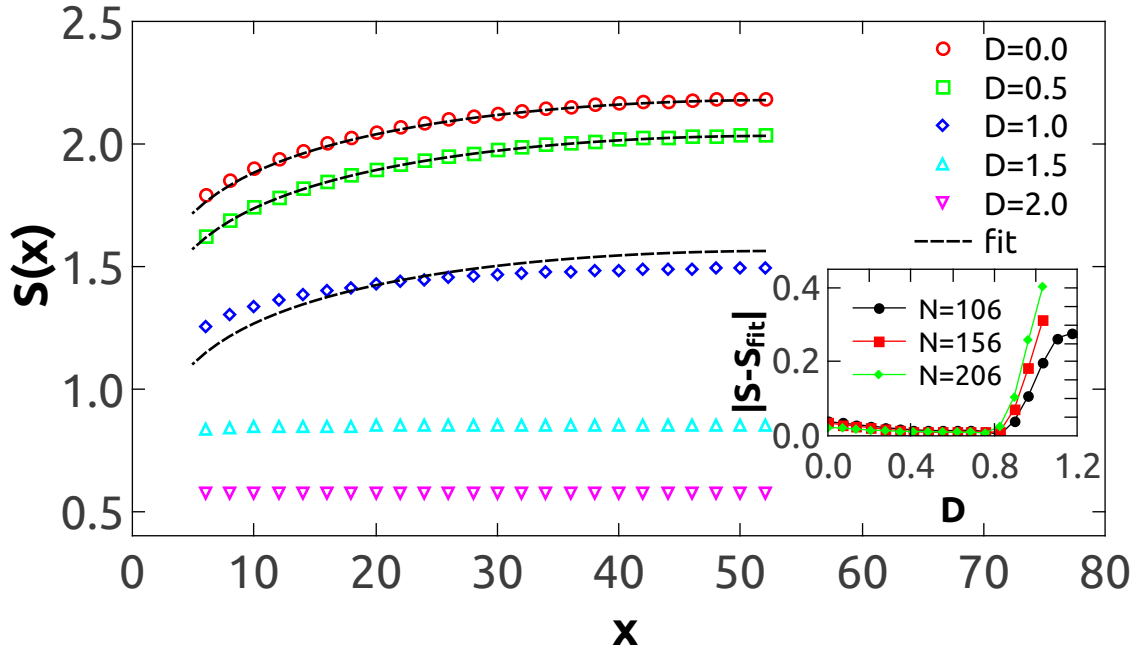
Fig. S.6.4: (color online). Entanglement entropy as a function of the partition size x for $N = 106$, $\Delta = -0.5$ and different values of the single-ion anisotropy D. The fittings of the numerical data to eq. 6.4 are also shown. The inset presents the fitting accuracy for systems of three sizes ($N = 106, 156, 206$), from which we find the BKT critical point at $D \approx 0.8$.

6.6   Conclusions

The local convertibility of many-body quantum states, an important concept in quantum information and computation theory, provides a comparison of the computational potential of adiabatic and LOCC procedures. The results presented in this chapter strongly suggest that this operational perspective on quantum states is not necessarily related to quantum phase transitions, but reflects properties of the entanglement spectrum which are intimately connected with symmetries of the microscopic model. In fact, we explicitly showed examples of local convertibility changes that do not correspond to phase transitions and phase transitions that do not correspond to alterations of the local convertibility. Furthermore, different models that fall into the same universality class, such as Luttinger liquids, may exhibit distinct convertibility properties. Hence, the non-universality of the convertibility.

Upon preparation of this manuscript we became aware of [50], where the entanglement spectrum for a couple of systems is shown to display pseudo transitions that do not correspond to physical phase transitions. The authors then conclude that it may be misleading to use entanglement measurements as detectors of quantum phase transitions, in agreement with our conclusions. Note that their conclusions are based on a different approach than ours, that is, one not related to high symmetry points or operational aspects.

Bibliography

[1] S. Sachdev, *Quantum Phase Transitions*, (Cambridge University Press, UK, 1999).

[2] A. Polkovnikov, Phys. Rev. B **72**, 161201(R) (2005).

[3] P. Doria, T. Calarco, S. Montangero, Phys. Rev. Lett. 106, 190501 (2011); T. Caneva, T. Calarco, R. Fazio, G. E. Santoro, S. Montangero, Phys. Rev. A 84, 012312 (2011).

[4] X.-G. Wen, *Quantum Field Theory of Many-Body Systems*, Oxford University Press, 2007.

[5] V. L. Berezinskii, Zh. Eksp. Teor. Fiz. **61**, 1144 (1971) (Sov. Phys. JETP **34**, 610 (1972)); J. M. Kosterlitz and D. J. Thouless, J. Phys. C **6**, 1181 (1973).

[6] C.-L. Hung, X. Zhang, N. Gemelke, and C. Chin, Nature **470**, 236 (2011).

[7] T. Giamarchi, *Quantum Physics in One Dimension* (Claredon Press, Oxford, 2004).

[8] Mciej Lewenstein, Anna Sanpera and Veronica Ahufinger, *Ultra Cold Atoms in Optical Lattices*, (Oxford, 2012).

[9] A. Hamma and D. A. Lidar, Phys. Rev. Lett. **100**, 030502 (2008).

[10] A. Hamma, L. Cincio, S. Santra, P. Zanardi and L. Amico, Phys. Rev. Lett. **110**, 210602 (2013).

[11] P. Bonderson and C. Nayak, Phys. Rev. B **87**, 195451 (2013).

[12] F. Pollmann and A. M. Turner, Phys. Rev. B **86**, 125441 (2012).

[13] Y. Zhao, W. Li, B. Xi, Z. Zhang, X. Yan, S.-J. Ran, T. Liu, and G. Su, Phys. Rev. E **87**, 032151 (2013).

[14] Z.-X. Liu, X. Chen, and X.-G. Wen, Phys. Rev. B **84**, 195145 (2011).

[15] X. Chen, Z.-C. Gu, and X.-G. Wen, Phys. Rev. B **84**, 235128 (2011).

[16] N. Schuch, D. Perez-Garcia, and I. Cirac, Phys. Rev. B **84**, 165139 (2011).

[17] Y. H. Su, B.-Q. Hu, S.-H. Li, and S. Y. Cho, Phys. Rev. E **88**, 032110 (2013).

[18] Y. Zhang, T. Grover, and A. Vishwanath, Phys. Rev. Lett. **107**, 067202 (2011).

[19] C. Mund, O. Legeza, and R. M. Noack, Phys. Rev. B **79**, 245130 (2009).

[20] L. Amico, R. Fazio, A. Osterloh and V. Vedral, Rev. Mod. Phys. **80** 517-576 (2008).

[21] A. Osterloh, L. Amico, G. Falci, R. Fazio, Nature **416**, 608 (2002); G. Vidal, J. I. Latorre, E. Rico, A. Kitaev, Phys. Rev. Lett. **90**, 227902 (2003).

[22] E. Mascarenhas, L. Heaney, M. C. O. Aguiar, M. F. Santos, New Journal of Physics, **14** 043033 (2012).

[23] H. Li and F. D. M. Haldane, Phys. Rev. Lett. **101**, 010504 (2008).

[24] F. Pollmann, A. M. Turner, E. Berg, and M. Oshikawa, Phys. Rev. B **81**, 064439 (2010).

[25] P. Calabrese and A. Lefevre Phys. Rev. A **78**, 032329 (2008).

[26] R. Thomale, A. Sterdyniak, N. Regnault, and B. A. Bernevig, Phys. Rev. Lett. **104**, 180502 (2010).

[27] M. Goldstein, Y. Gefen, and R. Berkovits, Phys. Rev. B **83**, 245112 (2011).

[28] V. Alba, M. Haque, and A. M. Läuchli, Phys. Rev. Lett. **108**, 227201 (2012).

[29] G. De Chiara, L. Lepori, M. Lewenstein, and A. Sanpera, Phys. Rev. Lett. **109**, 237208 (2012).

[30] L. Lepori, G. De Chiara, and A. Sanpera. Phys. Rev. B **87**, 235107 (2013).

[31] S. M. Giampaolo, S. Montangero, F. Dell Anno, S. De Siena, and F. Illuminati, Phys. Rev. B **88**, 125142 (2013).

[32] J. Cui, M. Gu, L.C. Kwek, M.F. Santos, Heng Fan, and V. Vedral, Nature Communications **3**, 812 (2012).

[33] J. Cui, L. Amico, H. Fan, M. Gu, A. Hamma, and V. Vedral, Phys. Rev. B **88**, 125117 (2013).

[34] J. Cui, J.P. Cao, and H. Fan, Phys. Rev. A **85**, 022338 (2012).

[35] M. A. Nielsen, Phys. Rev. Lett. **83**, 436 (1999).

[36] D. Jonathan and M. B. Plenio, Phys. Rev. Lett. **83**, 3566 (1999).

[37] S. Turgut, J. Phys. A: Math. Theor. **40**, 12185 (2007).

[38] Y. R. Sanders and G. Gour, Phys. Rev. A **79**, 054302 (2009).

[39] K. Okamoto and K. Nomura, J. Phys. A: Math. Gen. **29**, 2279 (1996).

[40] M. den Nijs and K. Rommelse, Phys. Rev. B **40**, 4709 (1989).

[41] W. Chen, K. Hida, and B. C. Sanctuary, Phys. Rev. B **67**, 104401 (2003).

[42] M. Tsukano, K. Nomura, J. Phys. Soc. Jpn. **67**, 302 (1998).

[43] Y. H. Su, S. Y. Cho, B. Li, H.-L. Wang, and H.-Q. Zhou, J. Phys. Soc. Jpn. **81**, 074003 (2012).

[44] T. Kennedy and H. Tasaki, Phys. Rev. B **45**, 304 (1992).

[45] A. Kitazawa, K. Hijii and K. Nomura, J. Phys. A: Math. Gen. **36**, L351 (2003).

[46] K. Nomura and A. Kitazawa, J. Phys. A: Math. Gen. **31**, 7341 (1998).

[47] T. Giamarchi and H. J. Schulz, Phys. Rev. B **39**, 4620 (1989).

[48] F. Pollmann, A. M. Turner, E. Berg, and M. Oshikawa, Phys. Rev. B **81**, 064439 (2010).

[49] P. Calabrese and J. Cardy, J. Stat. Mech. **P06002** (2004).

[50] A. Chandran, V. Khemani, S. L. Sondhi, arXiv:1311.2946.

Part III

Nonequilibrium many-body systems

Chapter 7

Dynamics and statistics of nonequilibrium spin chains

In this last chapter I will describe a project that emerged during my PhD studies and that will be pursued in the next few years. Because it is related to some of the main results and techniques developed during the PhD, I consider it relevant to present it in my thesis. I also thought that it would be a fine way to finalize this text by showing the direction intended for my future research on many-body systems. Note that, although I will include in this chapter preliminary results, most of what will be discussed are open questions that I would like to tackle from now on due both to their importance and beauty.

7.1   Introduction

The Classical Mechanics of isolated nonequilibrium systems is able to predict thermalization on local and global scales with the mechanism driving the process being chaos [7], which naturally manifests in nonlinear classical dynamics. On the other hand, in Quantum Mechanics it has been determined that entanglement in a nonequilibrium many-body state can be responsible for effective local equilibration of subsystems [2, 8]. Nonetheless, Quantum Mechanics is linear and thus not chaotic, therefore it is far from obvious what feature of complex quantum systems makes quantum thermalization possible on a global macroscopic scale [9]. Furthermore, the dynamics of isolated quantum systems is unitary and therefore they do not converge to equilibrium starting from a generic pure state. However, it may be the case for the overwhelming majority of the time instants, that the statistics of a few observables becomes indistinguishable from an effective equilibrated system.

Nonequilibrium physics is also important in the field of many-body systems where it is related, for example, to problems like transport and localisation, two issues with direct impact on our understanding of nature and on the design of new technologies. Even though transport physics, specially of electronic systems, is a cornerstone of all our technologies, the general problem of nonequilibrium transport seems far from being completely understood and answered. Significant steps towards this have been taken starting with Anderson localisation (or absence of diffusion) for zero temperature non-interacting particles [10]. Our understanding of localisation induced by disorder (spacial fluc-

tuations in the system structure) is heavily based on the single particle Anderson localisation. The energetic mismatch between neighbouring sites in a lattice may completely prevent transport by localising all single particle states. In a certain sense localised systems also prevent thermalization such that local perturbations are not diffused throughout the rest of the system. Such systems may then be called non-ergodic.

Only very recently, it has been shown that on top of the disordered landscape a combination of weak inter- particle interactions and thermal energy may induce delocalisation [11], thus extending Anderson work to the case of interacting particles. This equilibrium many-body localisation transition is a remarkable breakthrough which has sparked a new interest in the field. Importantly, it was noted that small interactions alone were not able to break localisation at low temperatures, and in fact thermal energy was necessary to induce delocalisation. Unexpectedly, different and novel behaviour is found for nonequilibrium systems. It was shown that initially localised states present an universal tendency to evolve into highly entangled states, even though such evolution is manifested in long time scales compared to the microscopic time scales [12]. These results suggest that arbitrarily small interactions are able to induce delocalisation. However, this has not been investigated. Therefore, *nonequilibrium localisation of interacting particles* is still a vast and untouched field.

In this last chapter we describe our latest project that aims at describing how and under which circumstances complex nonequilibrium systems behave effectively as equilibrated ones and also at describing novel nonequilibrium phenomena that cannot be effectively approximated by equilibrium models. This project, that started at the last few months of my PhD, investigates how complexity influences the long time statistics of dynamical systems and the time scales to eventually reach asymptotic statistics [1, 2].

I aim at characterising how each aspect of complexity (the range and type of many-body interactions; the structure of initial states as in quenched ground states, random product states, random entangled states; spacial disordered fluctuations of the system structure, deterministic time dependent alterations of the Hamiltonian) affects the physics of equilibration and I point out that this is far from accomplished in the current literature.

These aspects have been tackled mainly for noninteracting systems, that is, XY type spin chains that can be mapped to free fermions [1]. Such systems have well known phase diagrams at equilibrium, that is, from zero to infinite temperature [3]. Typically, these diagrams have a temperature axis and an axis representing changes of the Hamiltonian. The temperature axis can be thought of as an energy axis. The goal would be deriving analogous statistical phase diagrams (nonequilibrium phase diagrams) by adding energy to a zero temperature system taking it out of equilibrium by changing its hamiltonian (quantum quench) rather then adding thermal fluctuations. in this way the energy axis (temperature axis) is substituted by a nonequilibrium energy axis. We note that there are infinitely many ways of taking a system out of equilibrium and thus to a single equilibrium diagram there corresponds an infinite set of nonequilibrium diagrams.

We also review properties in systems of free fermions such as deriving the long time statistics of the entanglement in 1D systems and identifying if and how the quantum quench alters the localisation properties of given initial states. In this first step we identify new laws for the statistics and dynamics of nonequilibrium systems. The methods to accomplish these tasks are based on exact numerical solutions of the corresponding free fermion system to compute the time dependent fidelity to the ground state (Loschmidt echo) [4] and the time dependent block entanglement [5]. Nonetheless, it would also be of paramount importance to treat more complex cases such as interacting and disordered quantum systems. In the case of interacting systems, I will apply numerical

methods such as: sparse matrix diagonalization which is usually limited to a maximum of approximately 20 quantum systems and allows for long time dynamics; Density Matrix Renormalization Group which allows for hundreds of quantum systems but does not allow for extremely long time dynamics. For systems with long range interactions I will use exact matrix diagonalization, which is restricted in size, and also compare with random matrix theory [6] which is a model independent theory for complex quantum systems that is built upon the statistics of the Hamiltonian processes itself and has been successful in describing some complex systems. Despite of their limitations, all these methods are recognised to be accurate and efficient on a wide range of situations and we may interpolate from one method to the other to extract more general conclusions not limited by their respective traits.

I aim at characterising this process completely out of equilibrium for different classes of initial pure states. More specifically, investigate wider ranges of interactions and disorder analysing carefully the interplay between both. Two localisation perspectives should be compared, one in real space [13] and the other in the quantum state space [14]. These perspectives are independent and have very different meaning. However, there may be an interesting connection between them for it is known that non- entangled states are a very small portion of state space [15], and thus occasionally localisation in one sense might be connected to localisation in the other sense. I aim at showing how and when these notions are related in physically meaningful systems. It is also not clear wether or not there is a localisation transition or just a crossover. Even though the latter issue is of a more technical nature it is likely to have a great impact in the community and therefore I also aim at clarifying this debate. Finally I would study genuine out of equilibrium transport of energy and information in such many-body systems.

7.2   Loschmidt echo and Work distribution

Consider an isolated quantum many-body system in a pure equilibrium state, such as the ground state of the corresponding hamiltonian. Suppose the system is disturbed by an external agent that works on the system. The dynamics that follows after this process raises many questions. For example, a simple question would be: How sensitive is the many body state to a small perturbation? Or, can a small perturbation drastically take the system out of equilibrium? One answer to this question has been confirmed repeatedly: if the many body system is close to a low order quantum phase transition the system is extremely sensitive to the small perturbation [16]. The isolated system evolves unitarily which means reversible evolution, in principle. Therefore the dynamics does not present asymptotic states and in a strong sense they do not converge to an equilibrium state. However, we may still analyse the temporal statistics and address the effective equilibration and typicality. This issue has been tackled and it has been found that when the perturbation is small and the system is away from criticality it is effectively equilibrated. However, close to criticality the system presents an extensive oscillatory behaviour showing strong deviation from equilibrium [1].

In this chapter we are interested in characterising a few aspects of the effective equilibration of many-body systems. The short time behaviour is treated in more detail since it allows for an efficient characterisation of the dynamics. In fact we show that the short (at least $t < 1$) time behaviour allows us to analyse the time scales for the systems to relax to their average behaviour in time, the equilibration time. We also analyse how well the systems equilibrate using a few properties of the quench process, the entanglement dynamics, the Loschmidt echo and the distribution of the work corresponding to the quench.

One approach to this, commonly termed, quench problem has been the analysis of the Loschmidt

echo which was originally introduced in the quantum chaos literature [17]. Here we will focus on a special case of the Loschmidt echo. Suppose the initial state of the system is $|G_i\rangle$ the ground state of hamiltonian H_i. After the perturbation is applied the hamiltonian is transformed into $H_f = H_i + \epsilon V$, with V being the perturbation and ϵ its strength. Now, the Loschmidt echo is defined as

$$L(t) = |\langle G_i|e^{iH_it}e^{-iH_ft}|G_i\rangle|^2. \tag{7.1}$$

Since we have chosen the initial state to be an eigenstate of the initial hamiltonian the Loschmidt echo reduces to

$$L(t) = |\langle G_i|e^{-iH_ft}|G_i\rangle|^2 = |\langle G_i|\Psi(t)\rangle|^2, \tag{7.2}$$

which can be readily interpreted as the fidelity between the time evolving state and the initial state. In a general sense the issue of equilibration may be formulated in terms of the time fluctuations of the L-echo around its time average

$$L(t) = \overline{L} + \delta L(t), \tag{7.3}$$

with

$$
\begin{aligned}
\overline{L} &= \lim_{T\to\infty} \frac{1}{T}\int_0^T L(t)dt \\
&= \overline{\left|\sum_k |\langle k|G_i\rangle|^2 e^{-iE_kt}\right|^2} = \sum_{kl} |\langle k|G_i\rangle|^2 |\langle l|G_i\rangle|^2 \overline{e^{-i(E_k-E_l)t}} \\
&= \sum_k |\langle k|G_i\rangle|^4 .
\end{aligned}
\tag{7.4}
$$

In deed, there is a lot of information encoded into the echo, for instance if we define the time averaged state

$$\overline{\rho} = \overline{|\Psi(t)\rangle\langle\Psi(t)|} = \sum_k |\langle k|G_i\rangle|^2 |k\rangle\langle k|, \tag{7.5}$$

it follows that its purity is $\text{tr}\{\overline{\rho}^2\} = \overline{L}$. This average state is commonly called the diagonal ensemble for it has the same probability distribution as the initial state in the basis of the Hamiltonian eigenstates and has no coherences between them. This diagonal ensemble can be regarded as the nonequilibrium analog of the canonical ensemble. In fact, it can always be thought of as a sort of generalised Gibbs ensemble

$$\overline{\rho} = \frac{e^{-\sum_k \beta_k |k\rangle\langle k|}}{Z_G}, \tag{7.6}$$

with β_k being the Lagrange multipliers that can be determined by the set of self-consistent equations $e^{-\beta_k}/Z_G = |\langle k|G_i\rangle|^2$, with $Z_G = \sum_k e^{-\beta_k}$. In this case we have several constants of motion rather then just the energy, the average values of all the projectors onto energy eigenstates, and thus rather then having a single multiplier (the temperature) as in the canonical ensemble we have several multipliers. In any case we point out that this is a somewhat forced analogy since it compares an isolated dynamical system to a system in contact with a thermal bath or more precisely a system that is in a state that maximises the entropy given its internal energy. The forced analogies between equilibrium and nonequilibrium ensembles are well motivated while trying to derive equilibrium postulates from realistic nonequilibrium conditions, however rather then pursuing this venue here

we focus on dynamical quantities and highlight genuine nonequilibrium behaviour that has no equilibrium analog.

Regardless of the equilibrium analogies the purity of this nonequilibrium ensemble is still an interesting quantity as an inverse participation ration of "volume" in phase space. Thus the average value of the echo is directly connected to the spread of the dynamics is sate space. If the echo is unity it means that the system does not evolve and the dynamics are composed of a single pure state (completely localised in state space). If the echo drops to $1/d$ (with d being the dimension of the quantum system) then the dynamics is, in a sense, maximally delocalised. Note that this does not mean that all pure states are visited by the time evolution but rather that the system visits all energy-eigenstates with equal probability.

We can also define the relaxation or equilibration time t_{eq}, which is the time it takes for the echo to reach its average value for the first time. If we expand the echo in short time it assumes the form

$$L(t) \approx 1 - t^2 \alpha \approx e^{-\alpha t^2}, \tag{7.7}$$

which is a Gaussian decay with exponent

$$
\begin{aligned}
\alpha &= \langle G_i | H_f^2 | G_i \rangle - \langle G_i | H_f | G_i \rangle^2 \\
&= \epsilon^2 \left[\langle V^2 \rangle - \langle V \rangle^2 \right].
\end{aligned}
\tag{7.8}
$$

The equilibration time can be estimated as [18]

$$t_{\mathrm{eq}} = \sqrt{-\frac{\ln \overline{L}}{\alpha}}. \tag{7.9}$$

Thus, the relaxation should be typically dominated by the energy variance which is a measure of how the initial state is spread on the energy eigenstates of the final hamiltonian. It is known that close to criticality short time expansions may break down, however at least far from criticality the equilibration may be estimated with moderate efforts possibly even without resorting to long time evolution. We may in fact estimate the equilibration time from equilibrium properties. In case of a small perturbation the average echo reduces to the lower bound

$$\overline{L}_{\mathrm{bound}} = \lim_{||\epsilon V|| \to 0} \overline{L} = |\langle G_f | G_i \rangle|^4 \leq \overline{L}, \tag{7.10}$$

which is just the squared fidelity between the two equilibrium ground states. Therefore, for a general model the equilibration time after a small perturbation may be estimated from ground state properties.

Even though the above analysis works well it is interesting to remark that close to criticality the echo decay may deviate considerable from Gaussian [19]. We may then extend the time series expansion using the cumulant generating function [1]

$$L(t) = \exp\left\{ 2 \sum_n \alpha_{2n} \frac{(-t^2)^n}{(2n)!} \right\}, \quad \alpha_n = \epsilon^n \langle H_f^n \rangle_c, \tag{7.11}$$

such that for short times it is dominated by the Gaussian decay and higher order cumulants come into play after this initial decay [1].

After the relaxation time the echo starts oscillating around the average such that the amplitude and frequency of such oscillations characterize the effective equilibration. Therefore, the statistics of the echo $P(L) = \overline{\delta(L_t - L)}$ may be directly related to the effective equilibration [20]. Well equilibrated systems should have a narrow echo distribution ($\overline{\delta L^2} \approx 0$) while badly equilibrated systems should have a wide echo distribution.

The whole quench dynamics is the result of work being performed on or extracted from the system. To evaluate the work we need two measurements of the energy, a measurement before the quench and a measurement after the quench. The energy difference is the work. However, since the quantum measurement yields several possible results it turns out that we have a distribution of possible values of the work, and it is given by [21]

$$P(W) = \sum_k \delta(W - E_k)|\langle k|G_i\rangle|^2, \tag{7.12}$$

which is just the Fourier transform of the Loschmidt amplitude, the characteristic function. This distribution is also known as the local density of states in analogy to the density of states $P(E) = \text{tr}[\delta(E - H)]$ restricted to or weighed by the initial state $P(W) = \langle G_i|\delta(W - H)|G_i\rangle$ To compute the moments of the distribution it is rather convenient to work with the characteristic function

$$
\begin{aligned}
G(t) &= \int e^{-iWt}P(W)dW \\
&= \sum_k e^{-iE_k t}|\langle k|G_i\rangle|^2 \\
&= \left\langle e^{-iH_f t}\right\rangle
\end{aligned}
\tag{7.13}
$$

whose modulus square is the Loschmidt echo $L(t) = |G|^2$ [21]. The moments of the distribution are then given by

$$\overline{W^n} = \int W^n P(W)dW = (i)^n \left[\frac{d^n G(t)}{dt^n}\bigg|_{t=0}\right]. \tag{7.14}$$

The average work is given by

$$\overline{W} = \epsilon\langle V\rangle, \tag{7.15}$$

which is in direct agreement with the standard identification of quantum work [22], such that only the hamiltonian changes in the sudden quench without the system having time to evolve $dE = \text{tr}\{dH\rho\} + \text{tr}\{Hd\rho\} = \text{tr}\{dH\rho\} = \overline{W}$. The second moment is

$$\overline{W^2} = \epsilon^2\langle V^2\rangle, \tag{7.16}$$

which has a direct connection to the decay of the L-echo. From what we have just derived it follows that the echo decays as a Gaussian with the work variance as

$$L(t) \approx \exp\left\{-\overline{\delta W^2}t^2\right\}, \tag{7.17}$$

with $\alpha = \overline{\delta W^2}$, and in fact the α_n are the cumulants of the work distribution. Therefore, the Loschmidt echo depends only on the even cumulants of the work distribution. This is an interesting relation between the work distribution and the decay of the Loschmidt echo which has not been realised before, even though the α coefficient has been throughly determined previously [4].

7.3   Methods

In this section we highlight the main features of the methods employed in this chapter, namely the t-DMRG algorithm that extends DMRG to time evolution and free fermion techniques applicable for the Ising and XY models.

7.3.1   t-DMRG

The t-DMRG method is a direct extension of DMRG to dynamically evolving systems. First the system is initialised in a ground state using standard DMRG and then the system is evolved through a procedure very similar to the "sweeps" portion of the static DMRG method, however at each step a two site evolution operator is applied. Sweeping from site to site is done by the algorithm developed by S. White where we change the representation of the state from (for example) Block $\bullet_i \bullet_{i+1}$Block to Block $\bullet_{i+1} \bullet_{i+2}$Block. Now, this was already used in the DMRG method. The extra ingredient is the Trotter-Suzuki decomposition of the evolution operator e^{-iHt}. Say we have

$$H = H_{\text{odd}} + H_{\text{even}}, \tag{7.18}$$

with H_{odd} being the hamiltonian for the odd links in the chain, that is, the coupling from site 1 to site 2, site 3 to site 4 and so on. Analogously H_{even} couples site 2 to site 3, site 4 to site 5 and so on. The first order Trotter decomposition then reads

$$e^{-iHdt} \approx e^{-iH_{\text{odd}}dt}e^{-iH_{\text{even}}dt} + \mathcal{O}(dt^2). \tag{7.19}$$

Such decomposition would lead to erros of order dt^2 and it is thus desirable to perform higher order decompositions. Here we choose to stop at second order

$$e^{-iHdt} \approx e^{-iH_{\text{odd}}dt/2}e^{-iH_{\text{even}}dt}e^{-iH_{\text{odd}}dt/2} + \mathcal{O}(dt^3). \tag{7.20}$$

Thus in practice, implementing the evolution for a small time dt requires one sweep and a half and at each step a link evolution operator $e^{-iH_{<i,j>}dt}$ is applied with $H_{<i,j>}$ being the hamiltonian of two nearest neighbour sites. However this is still highly convenient since a discretisation of order $dt = 10^{-2}$ leads to errors of order 10^{-6}. In any case the biggest source of errors remains the DMRG or bond truncation, that is, the number of states kept m at each renormalization.

In figure (7.1) we show t-DMRG data for the Loschmidt echo of the Ising model with 100 sites after a weak quench in the external field far from and close to the critical point with $h_z = 0.5$ and $h_z = 0.9$ with $\Delta h_z = 0.1$. We can see that the echo converges to a well defined value by increasing m. Out side criticality the echo quickly converges to its average value, moreover the lower bound L_b is an accurate estimation of the average value. At criticality the behaviour is markedly different. The lower bound is not as tight as in the previous case and the echo show much stronger decay.

Now, by studying only the short time behaviour we obtain the variance of the work distribution α and the corresponding estimate of the equilibration time $t_{\text{eq}} \approx \sqrt{-\frac{\ln \overline{L}_{\text{bound}}}{\alpha}}$. As we can see in figure 7.2 the variance of the work distribution scales with the number of spins N and presents a discontinuous derivative at the critical point. We can see in figure (7.2) that away from criticality the equilibration time can be robustly estimated from the initial Gaussian behaviour and the lower bound for the average L-echo and the average echo is close to the lower bound. In this case the equilibration time has a well defined value in the thermodynamic limit as we can see by increasing the number of sites N in figure (7.2). At criticality the equilibration time keeps increasing with the system size. In fact, it diverges in the thermodynamic limit [18].
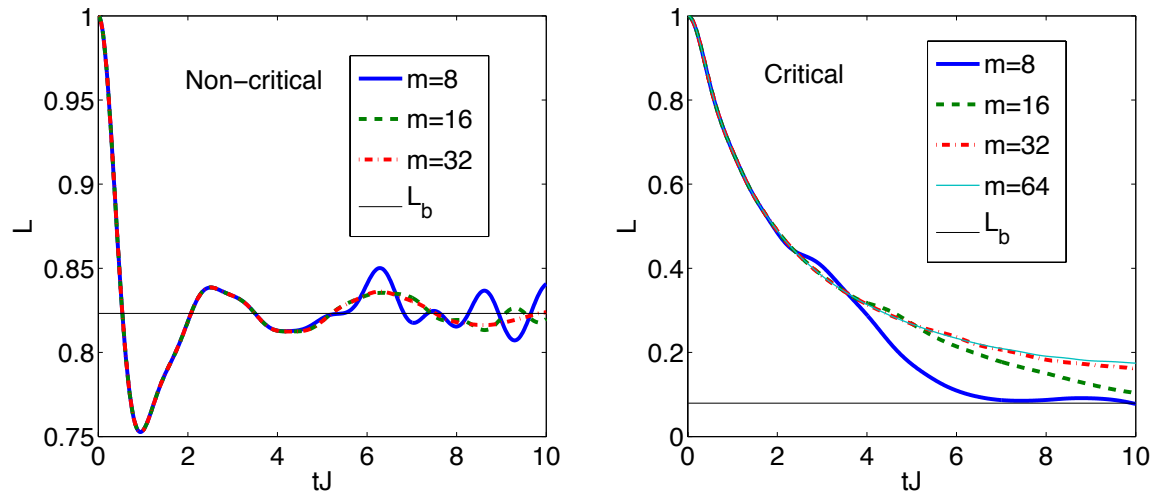
Fig. S.7.1: t-DMRG data for the Loschmidt echo of the Ising model with 108 sites after a weak quench in the external field far from the critical point with $h_z = 0.5$ and close to the critical point with $h_z = 0.9$ with $\delta h_z = 0.1$
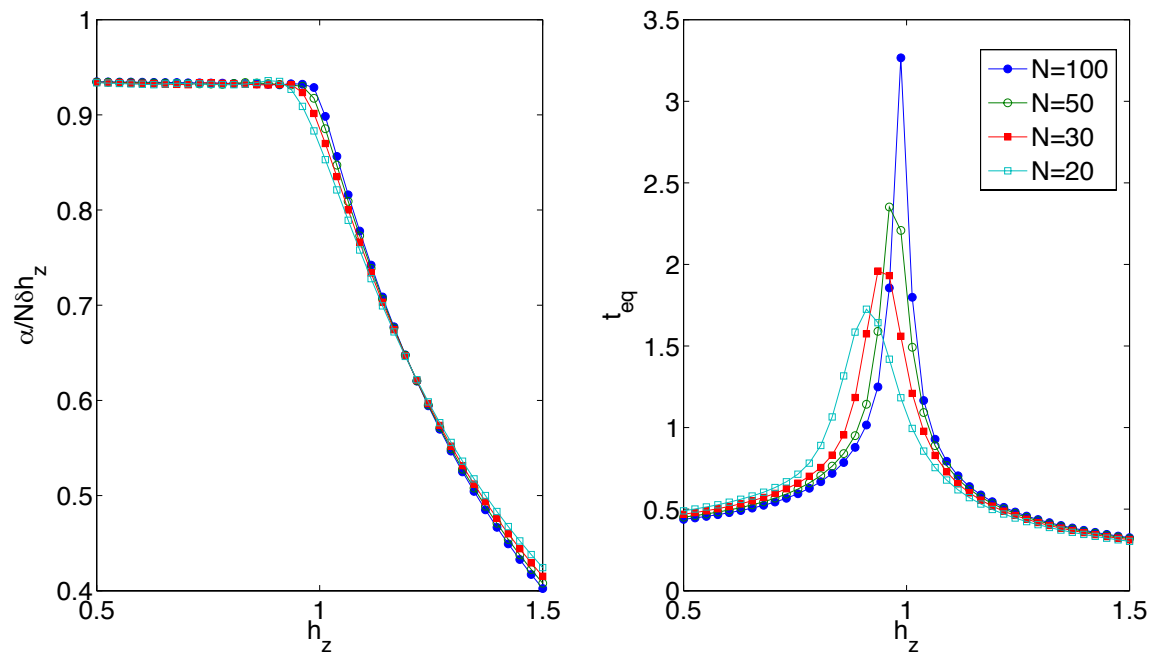
Fig. S.7.2: Gaussian exponent fit for the short time dynamics of the Loschmidt echo and the lower bound for the equilibration time of the Ising model after a weak quench in the external field with $\delta h_z = 0.01$

7.3.2 Spin-chains and Free fermions

Addressing the long time dynamics, and therefore, the time statistics and the work distribution is a tough numerical problem for general large system. In this case t-DMRG is not able to simulate the evolution, mainly because entanglement keeps increasing during the evolution and thus the number os states necessary to represent the time evolving state increases significantly. We are thus effectively restricted to very small sizes (up to 20 sites) using exact diagonalization. However, some spin hamiltonians a can be mapped to hamiltonians of noninteracting fermions and in this case we can exactly evaluate the long time evolution of large systems. Let us now briefly describe the mapping starting with the Ising hamiltonian

$$H = \sum_i \left[J X_i X_{i+1} + h Z_i \right], \tag{7.21}$$

with X and Z being the corresponding Pauli matrices, with J being the coupling in the X direction and h the external transverse field. The Pauli matrices can be expressed by the lowering (σ) and rising spin operators ($\sigma^\dagger$). The Jordan-Wigner transformation maps the spin chain into a fermionic chain as

$$c_k = \exp\left(i\pi \sum_{j=1} \sigma_j^\dagger \sigma_j \right) \sigma_k, \tag{7.22}$$

with the hamiltonian being rewritten as

$$H = \sum_{i,j} \left[c_i^\dagger A_{i,j} c_j + c_i^\dagger B_{i,j} c_j^\dagger + \text{H.c} \right], \tag{7.23}$$

with

$$A_{j,k} = J(\delta_{k,j+1} + \delta_{j,k+1}) + 2h\delta_{j,k}, \tag{7.24}$$

$$B_{j,k} = J(\delta_{k,j+1} - \delta_{j,k+1}). \tag{7.25}$$

This corresponding fermionic Hamiltonian is quadratic in the creation and annihilation operators. This allows for an exact numerical solution and quantities like the Loschmidt echo and the entanglement entropy can be calculated for arbitrarily long times. The algorithms to compute such quantities are described in [4] and [5] respectively.

7.4 Long time Statistics of Noninteracting fermions

Much of the analysis done by Zanardi and Campos Venuti focussed on the echo for small systems tractable by exact diagonalization. They also focussed on small quenches and their results suggested that the echo distribution $P(L)$ was the ultimate figure of merit for describing the dynamics. However, the small systems and the small perturbation they have chosen generate misleading circumstances in the sense that their conclusions are not universal.

Let us first take large systems (100 spins). In figure (7.3) we show the echo, the echo distribution and the work distribution for a small quench outside criticality. As expected the echo oscillates (with small amplitude) around a well defined average value. The finite size generated recurrences that are clear in the echo dynamics and also manifested as a high peak in the echo distribution.
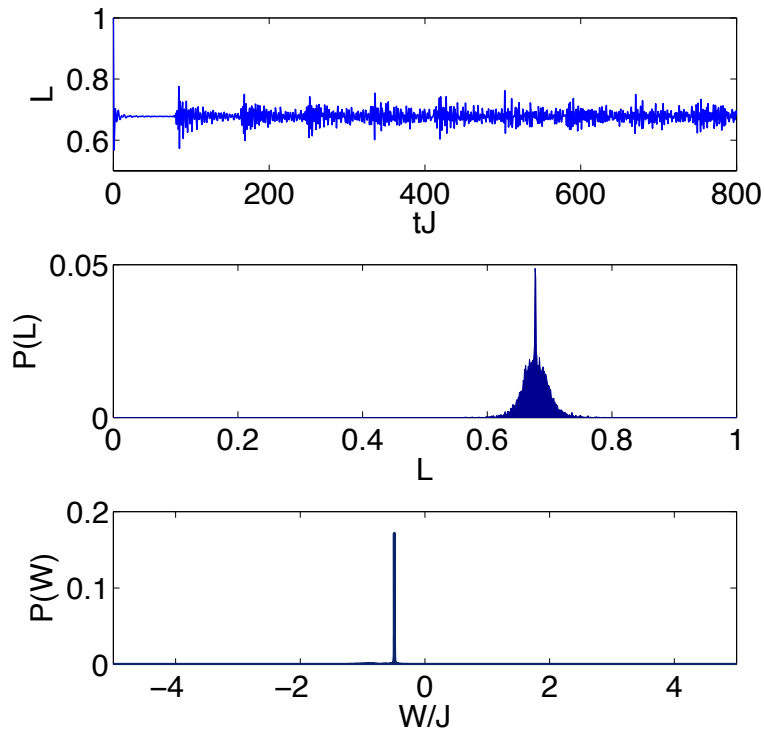
Fig. S.7.3: The Loschmidt echo L, the echo distribution $P(L)$ and the work distribution for the Ising model with 100 sites in a quench from $h = 0.5J$ to $h = 0.6J$.
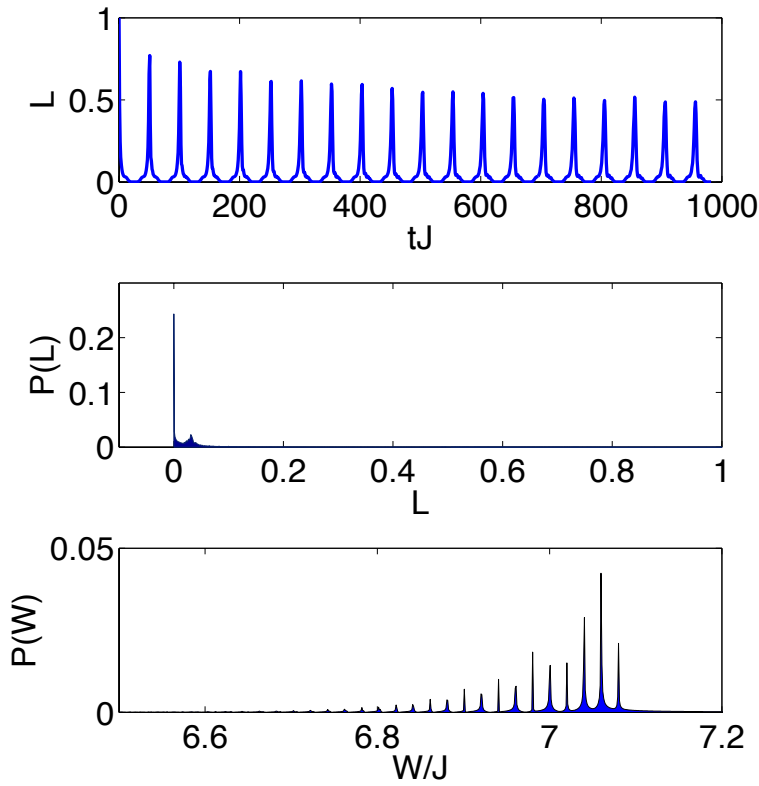
Fig. S.7.4: The Loschmidt echo L, the echo distribution $P(L)$ and the work distribution for the Ising model with 100 sites in a quench from $h = 0.9J$ to $h = 1J$.
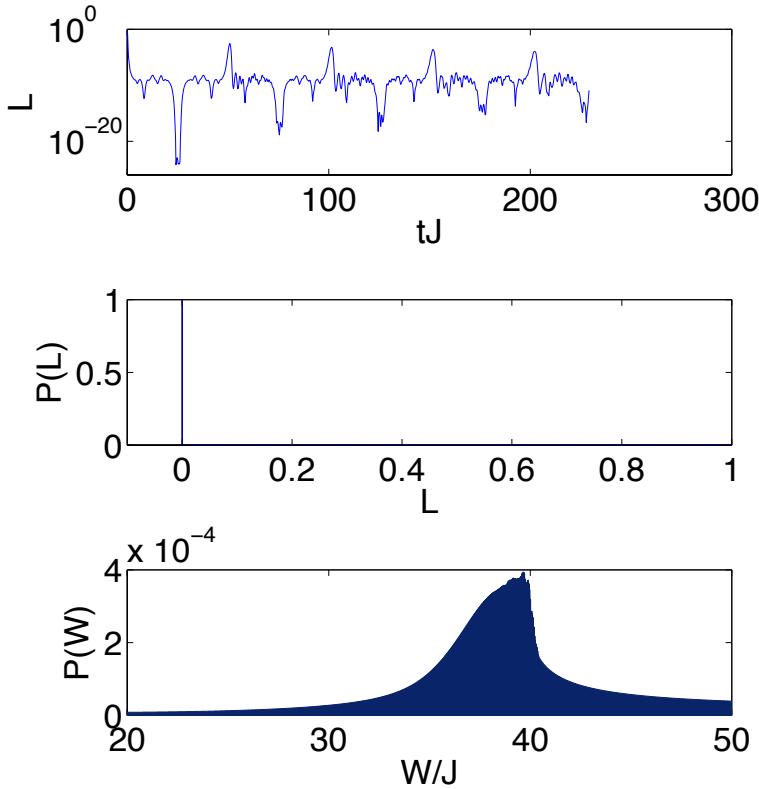
Fig. S.7.5: The Loschmidt echo L, the echo distribution $P(L)$ and the work distribution for the Ising model with 100 sites in a quench from $h = 0.5J$ to $h = 1J$.

The work distribution shows a single narrow peak indicating that, effectively, a single transition was triggered by the quench.

In figure (7.4) we show the echo, the echo distribution and the work distribution for a small quench close to criticality. As expected the echo strongly oscillates and spend most of the time at very small values. The finite size generated recurrences that are clear in the echo dynamics, however, they are not as clear in the echo distribution. Here the two-peaked behaviour highlighted by Zanardi is almost absent. The work distribution shows a series of well resolved peaks indicating that, effectively, several transitions were triggered by the quench.

In figure (7.5) we show the echo, the echo distribution and the work distribution for a big quench close to criticality. The echo drops quickly to very small values and displays small amplitude oscillations. The finite size generated recurrences that are clear in the echo dynamics, however, they are not as clear in the echo distribution as in the previous case. Here the two-peaked behaviour highlighted by Zanardi is absent. The work distribution shows a wide spreading with no peak-resolution indicating that the strong quench effectively excites a continuum of transitions such that the system is significantly decolonized in state space (also spread in energy).

We have thus seen that a small quench far from criticality has a small effect over the system
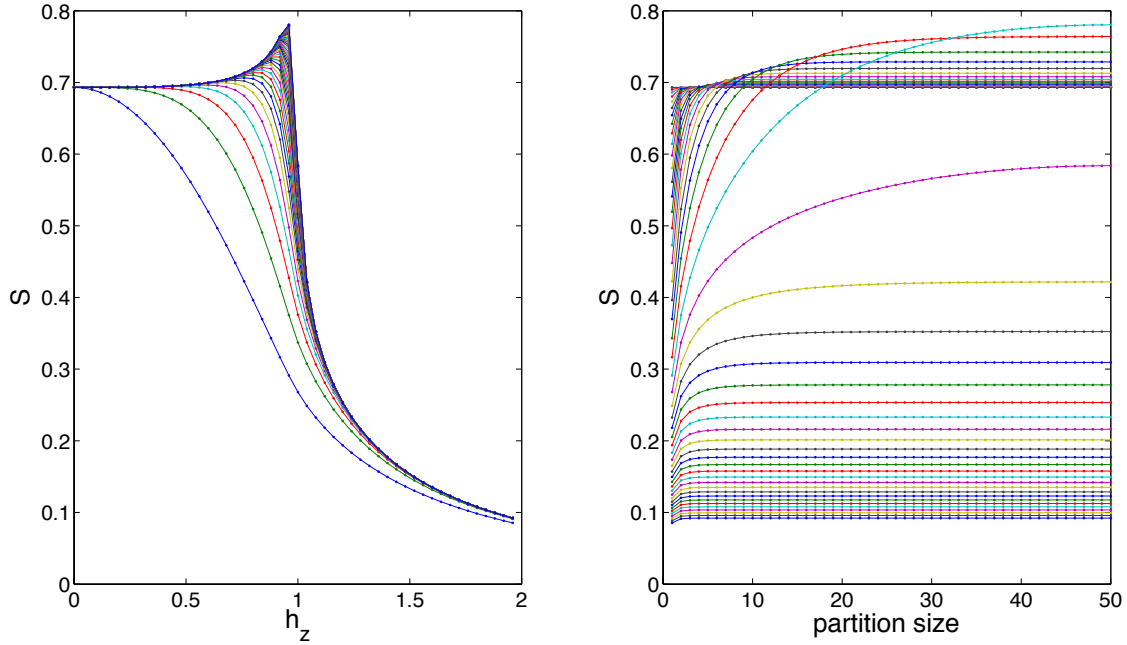
Fig. S. 7.6: The ground state entanglement of the Ising model for 100 sites. On the left the entropy for different partition sizes (the more pronounced the critical point the grater the size of the partition) as a function of the external field and on right the entropy for different field strengths (saturated or constant behaviour away from criticality and logarithmic behaviour close to criticality) as a function of the partition size.

state and it remains close to the original ground state, thus effectively in equilibrium. A small quench close to criticality strongly affects the system and it is strongly taken out of equilibrium. And finally, the strong quench could generate an effectively thermodynamically equilibrated system in a sense closely connected to the microcanonical formulation. In this case we have a continuum set of excited or populated states in a well defined energy shell.

   Before turning to the more general and realistic problem of interacting systems we start discussing the two notions of localisation in the noninteracting case. The two notions being localisation in state space which is already measured by the average echo and the work distribution and localisation in real space which can be captured by the entanglement in the quantum state.

   As we saw previously critical points and strong quenches can significantly delocalise the system in state space. Now we take one step further and analyse the system entanglement verifying how quantum correlations are spread throughout the system and how they evolve after a quench. Showing how delocalisation in real space is triggered by the quench.

   First let us recall the behaviour of the ground state entanglement entropy for the Ising model. In figure 7.6 we show the entropy both as a function of the external field and as a function of the partition size. We can see that at criticality the entropy obeys a length law, that is, the entanglement increases with the number of sites in the partition. On the other hand, outside criticality the entropy saturates to a constant value. The saturation of the entropy means that
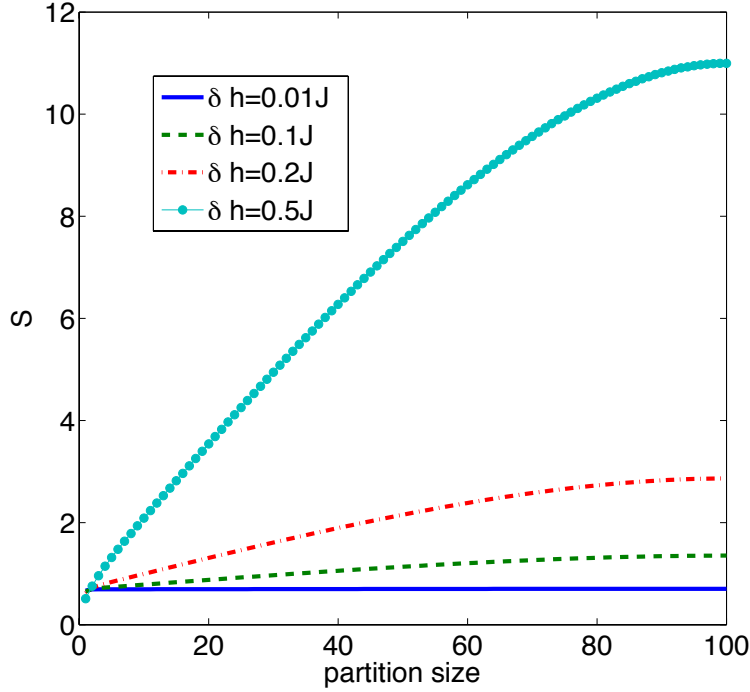
Fig. S.7.7: Time-snap shot of entanglement entropy of the Ising model after a sudden change of the external transverse field before finite size effects kick in.

correlations have a finite length scale and they do have a long range. The length law mean that correlations are long ranged and they keep increasing with the partition size.

In figure 7.7 we show the time average entanglement entropy and we can clearly observe that an approximate linear length law emerges and the entanglement increases with the size of the quench. Also the rate at which the entanglement increases with the partition size is greater the grater the size of the quench. After the quench the system visits highly entangled states that are delocalised in real space. There is an approximate linear behaviour for entropy before reaching partitions of the same order as the total size. It is interesting also to point out that the nonequilibrium behaviour of the entropy is not analogous to the equilibrium behaviour. It is neither saturated nor logarithmic. It is thus a genuine nonequilibrium behaviour.

Finally in figure 7.8 we compare the localisation in state space and real space and we can see that both notions of localisation seem to behave in a similar way.

7.5 Disordered quenched Spins And Many-body Localisation

In this section we will study the competing effects between disorder interactions. Previously we have focussed on the Ising model which maps to a system of noninteracting fermions. Now we study the XXZ model which maps to interacting fermions. Very recently we have seen the discovery of

(a)

(b)
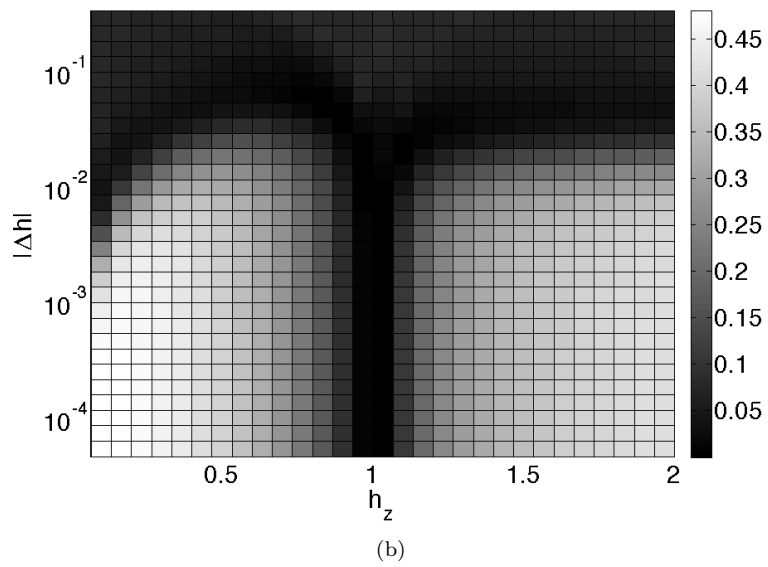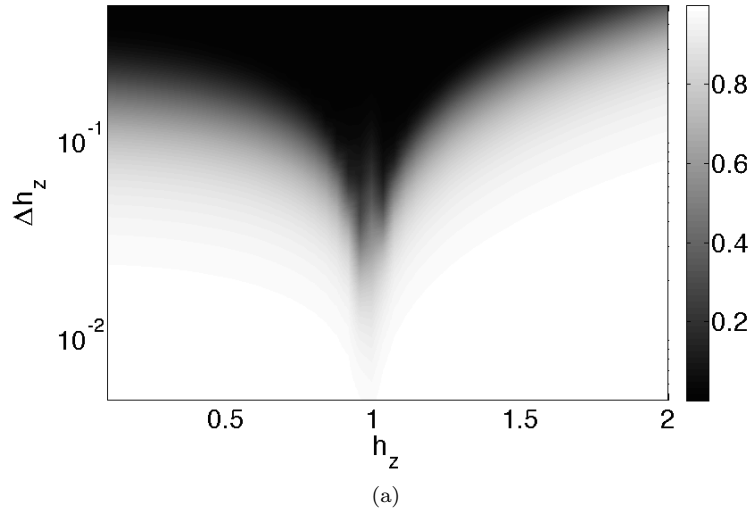
Fig. S.7.8: Here we plot the average echo and the distance between the average entropy and the closest conformal-field-theory fit. In this figure we compare the localisation in state space and the localisation in real space.
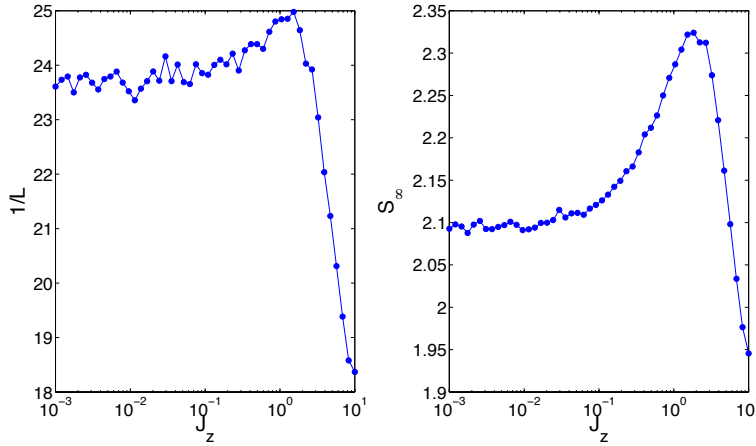
Fig. S.7.9: Time-snap shot of entanglement entropy of the Ising model after a sudden change of the external transverse field before finite size effects kick in.

novel nonequilibrium laws regarding the system entanglement [12]. However, the competing effects of disorder and interactions still remain to be addressed (only the perturbative limit was studied). Furthermore, the two notions of localisation have not been compared yet for interacting quantum systems.

In figure 7.9 we show a preliminary result for the average value of the echo and the asymptotic value of the entropy in the middle of the chain. We can see again that they seem to follow the same trend. But most importantly, there is a peak in both quantities indicating that even though the interactions and disorder tend to localise the system there is a regime in which their localising mechanisms are partially neutralised and the system seem more delocalised. We point out that further studies are still been carried out. But this seem a promising venue for uncovering emerging nonequilibrium phenomena related to the many-body localisation.

7.6 Conclusion

In this preliminary report of the project we have seen a few interesting novel phenomena. We have seen that there emerges a linear length law for the entanglement in noninteracting fermions after a sudden quench. Another step in this direction would be how interactions change the length law. We have also compared two notions of localisation: in state space and real space. And it seems that both follow similar behaviours also for interacting particles. Furthermore, we have also seen nonequilibrium competitions between interactions and disorder which is a breath of fresh air to the long line of research initialised by Anderson's nobel prise winning contribution.

Bibliography

[1] Lorenzo Campos Venuti and Paolo Zanardi, *Unitary equilibrations: Probability distribution of the Loschmidt echo*, Phys. Rev. A *81*, 022113 (2010); Lorenzo Campos Venuti, Sunil Yeshwanth, and Stephan Haas, Phys. Rev. A 87, 032108 (2013).

[2] F. Brandao, P. Cwiklinski, M. Horodecki, P. Horodecki, J. Korbicz, and M. Mozrzymas, Phys. Rev. E 86, 031101(2012).

[3] S. Sachdev, *Quantum Phase Transitions*, (Cambridge University Press, 1999).

[4] Davide Rossini, Tommaso Calarco, Vittorio Giovannetti, Simone Montangero, and Rosario Fazio, *Decoherence induced by interacting quantum spin baths*, Phys. Rev. A **75**, 032333 (2007).

[5] G. Torlai, L. Tagliacozzo, G. De Chiara, arXiv:1311.5509.

[6] Fritz Haake, *Quantum Signatures of Chaos*, (Springer, 2010); Hans-Jurgen Stockmann, *Quantum Chaos*, (Cambridge University Press, 2000).

[7] J. R. Dorfman, An Introduction to Chaos in Nonequilibrium Statistical Mechanics, Cambridge Lecture Notes in Physics (Cambridge University Press, Cambridge, 1999); Christian Beck, Thermodynamics of Chaotic Systems: An Introduction (Cambridge Nonlinear Science Series, 1997).

[8] S. Popescu, A. J. Short, and A. Winter, Nature Physics 2, 754 - 758 (2006).

[9] M. Rigol, V. Dunjko, and M. Olshanii, Nature (London) 452, 854 (2008).

[10] P. W. Anderson, Physical Review, Phys. Rev. 109, 1492 (1958).?

[11] D. M. Basko, I. L. Aleiner and B. L. Altshuler, Annals of Physics, 321, 1126 (2006); I. V. Gornyi, A. D. Mirlin, and D. G. Polyakov, Phys. Rev. Lett. 95, 206603 (2005).?

[12] Jens H. Bardarson, Frank Pollmann and Joel E. Moore, Phys. Rev. Lett. 109, 017202 (2012); Maksym Serbyn, Z. Papic, and Dmitry A. Abanin, Phys. Rev. Lett. 110, 260601 (2013).

[13] Richard Berkovits, Phys. Rev. Lett. 108, 176803 (2012).

[14] A. De Luca and A. Scardicchio, Europhys. Lett. 101, 37003 (2013).

[15] Oscar C. O. Dahlsten, Cosmo Lupo, Stefano Mancini, Alessio Serafini, arXiv:1404.1444.?

[16] H. T. Quan, Z. Song, X. F. Liu, P. Zanardi and C. P. Sun, *Decay of Loschmidt Echo Enhanced by Quantum Criticality*, Phys. Rev. Lett. **96**, 140604 (2006).

[17] Rodolfo A. Jalabert and Horacio M. Pastawski, *Environment-Independent Decoherence Rate in Classically Chaotic Systems*, Phys. Rev. Lett. **86**, 2490 (2001).

[18] Lorenzo Campos Venuti, Sunil Yeshwanth, and Stephan Haas, *Equilibration times in clean and noisy systems*, Phys. Rev. A **87**, 032108 (2013).

[19] Arseni Goussev, Rodolfo A. Jalabert, Horacio M. Pastawski, Diego Wisniacki, *Loschmidt Echo*, Scholarpedia 7(8), 11687 (2012).

[20] Lorenzo Campos Venuti, N. Tobias Jacobson, Siddhartha Santra, and Paolo Zanardi, *Exact Infinite-Time Statistics of the Loschmidt Echo for a Quantum Quench*, Phys. Rev. Lett. **107**, 010403 (2011).

[21] Alessandro Silva, *Statistics of the Work Done on a Quantum Critical System by Quenching a Control Parameter*, Phys. Rev. Lett. **101**, 120603 (2008).

[22] Massimiliano Esposito and Shaul Mukamel, Phys. Rev. E **73**, 046129 (2006).

Chapter 8

Conclusion

Throughout this thesis we have seen equilibrium and nonequilibrium emergent phenomena on interacting quantum systems. We have seen how a collection of quantum emitters behaves markedly differently from a set of independent emitters due to the emergent light filed; we have seen nonequilibrium light transport in non-linear electromagnetic cavities; emergent equilibrium phases in hybrid light-matter structures; operational properties of equilibrium emergent phases and nonequilibrium dynamics and statistics in spin chains including localisation properties.

In the last chapter we have laid out guiding lines for future research. The next step would be to use light matter interfaces to measure and expose novel many-body effects following similar lines as Igor. B. Mekhov, Christoph Maschler, Helmut Ritsch, Nature Phys. 3, 319 (2007); Kai Eckert, Oriol Romero-Isart, Mirta Rodriguez, Maciej Lewenstein, Eugene S. Polzik, Anna Sanpera, Nature Physics 4, 50-54 (2008). More specifically it will be very interesting to describe the light emission of strongly interacting systems addressing the statistics of the light in driven dissipative configurations that are found out of thermodynamical equilibrium (an example would be a lattice of driven dissipative non-linear cavities). Extending the work of the thesis I will be (i) analysing how interactions between quantum emitters influence light-amplification-through-stimulated-emission-of-radiation (LASER) and also the physics of subradiance and superradiance. This topic has not been appropriately tackled before as laser theory assumes noninteracting emitters. (ii) Using light matter interactions to translate the many-body properties into the light statistics, thus using the field as a probe and (iii) using the many-body interactions to taylor the quantum states of both the light and matter fields towards information processing applications.

Developing such project would (i) significantly advance our understanding of collective phenomena behind the postulates of macroscopic physics and also identify novel emergent laws for nonequilibrium systems, (ii) provide an important step in understanding the statistics and transport of interacting particles in random landscapes (ii) and also set the ground for upcoming technologies that envision harnessing quantum effects and complexity in condensed matter and optical systems.